Università degli Studi di Salerno

Dipartimento di Chimica e Biologia "A. Zambelli"

XXXIII ciclo di dottorato

Supported Gold Nanoparticles as Promising Catalysts in Sustainable Organic Synthesis

Tutor:

Prof. Alfonso Grassi

Ph. D. Course Coordinator:

Prof. Claudio Pellecchia

Ph. D. Student:

Antonella Dentoni Litta

8800100037

2020 - 2021

Università degli Studi di Salerno

Dipartimento di Chimica e Biologia "A. Zambelli"

XXXIII ciclo di dottorato

Supported Gold Nanoparticles as Promising Catalysts in Sustainable Organic Synthesis

Tutor:

Prof. Alfonso Grassi

Ph. D. Student:

Antonella Dentoni Litta

8800100037

Ph. D. Course Coordinator:

Prof. Claudio Pellecchia

2020 – 2021

With you

Everything seems so easy

With you

My heartbeat has found its rhythm

With you

I'm so close to finding my home

[Lasse Lindh - Run to You]

TABLE OF CONTENTS

2

ABSTRACT

Gold nanoparticles (AuNPs) emerged as very promising catalysts in a lot of organic reactions and industrial applications. These catalysts are in fact capable of catalysing chemical processes under mild conditions and according to the principles of Green Chemistry. Considering these peculiar features, during the years, scientific research has been addressed toward the design of more and more performing heterogeneous gold catalysts. To this aim, very relevant is the role of the support; as a matter of fact this allows preventing the sintering of the AuNPs but can also affect the catalyst performances by e.g. tuning the selectivity of the reaction.

Among the heterogeneous gold catalysts, AuNPs embedded in a porous crystalline polymer matrix consisting of polystyrene-*co*-cis-1,4-polybutadiene (sPSB) appeared of relevant research interest because of the peculiar reactivity patterns observed in a number of organic reactions, such as the selective aerobic oxidation of alcohols, nitroarenes reduction and aerobic oxidative esterification of cinnamyl alcohol.

This PhD thesis has been mainly addressed to the applications of the AuNPs-sPSB catalyst in Green Chemistry to assess the potential of this gold catalyst in organic reactions of interest in sustainable catalysis, such as the intermolecular and intramolecular hydroamination of arylacetylenes with anilines, and selective oxidation and oxidative esterification of HMF.

The intermolecular hydroamination of anilines with phenylacetylenes allowed the synthesis of aromatic ketimines in high yields and with excellent regio- and stereo-selectivity; the AuNPs-sPSB catalyst appeared thermally robust and recyclable. The kinetic investigation of hydroamination reaction, supported by DFT calculations, highlighted a new reaction pathway where the nucleophilic attack of the aniline occurs at the coordinated/activated phenylacetylene onto gold surface and is assisted by the formation of aniline aggregates stabilized via hydrogen bondings.

Cascade reactions are hot topic in Green Chemistry. In situ intramolecular hydroamination of 2-(2-propynyl)anilines followed by asymmetric transfer hydrogenation with the Hantzsch ester to produce chiral tetrahydroquinolines were successfully investigated using the AuNPs-TiO$_2$ catalyst; excellent regio- and enantioselectivity toward chiral tetrahydroquinolines were achieved under mild reaction conditions. The introduction of an electron-donating group (EDG = OMe) on the aromatic ring of the phenylacetylene moiety allowed an excellent control of the regioselectivity of the nucleophilic attack of the nitrogen atom to the π-system of the alkyne.

The selective oxidation and oxidative esterification of HMF were tuned by means of a fine control of the reaction parameters (crystalline phase of the support, temperature, solvent, oxygen

pressure); the HMF conversion into the desired products, namely 2,5-diformylfuran (DFF), 5-formyl-2-furancarboxylic acid (FFCA), 5-hydroxymethyl methylfuroate (HMMF), furan-2,5-dimethylcarboxylate (FDMC) and 2,5-furandicarboxylic acid (FDCA) was obtained in good yields with high selectivity under moderate experimental conditions.

ABBREVIATIONS

2-MeTHF: 2-Methyltetrahydrofuran

2,5 DMF: 2,5-dimethylfuran

AAS: Atomic Absorption Spectroscopy

AN: Aniline

AN-d_2: *N,N*-Aniline-d_2

Au-BM: Gold-Base Metals

Au-PGM: Gold-Platinum Group Metals

AuNPs: Gold Nanoparticles

AuNPs-(β)sPSB: AuNPs-sPSB in β crystalline phase of the polymeric support

AuNPs-(δ)sPSB: AuNPs-sPSB in δ crystalline phase of the polymeric support

AuNPs-(ε)sPSB: AuNPs-sPSB in ε crystalline phase of the polymeric support

AuNPs-Al$_2$O$_3$: Gold Nanoparticles supported on Aluminum Oxide

AuNPs-Carbon: Gold Nanoparticles supported on Carbon

AuNPs-CB: Gold Nanoparticles supported on Carbon Black

AuNPs-Fe₂O₃: Gold Nanoparticles supported on Iron(III) Oxide

AuNPs-NPCeO₂: Gold Nanoparticles supported on Ceria Nanoparticles

AuNPs-sPSB: Gold Nanoparticles supported on sPSB

AuNPs-TiO₂: Gold Nanoparticles supported on Titanium Oxide

AuNPs-ZnO: Gold Nanoparticles supported on Zinc Oxide

AuNPs-Zr(OH)₄: Gold Nanoparticles supported on Zirconium Hydroxide

BE: Binding Energy

CDA: Chiral Derivatizing Agent

CP: Co-Precipitation Method

CTEM: Conventional Transmission Electron Microscopy

DFF: 2,5-diformylfuran

DFT: Density Functional Theory

DHMF: 2,5-dihydroxymethylfuran

DLC: Dynamic Light Scattering

DMA: *N,N*-dimethylacetamide

DMF: *N,N*-dimethylformamide

DMSO: Dimethyl Sulfoxide

DP: Deposition-Precipitation Method

ED: Electrondonating

EWG: Electronwithdrawing

FA: Phenylacetylene

fcc: face centered cubic

FDCA: 2,5-furandicarboxylic acid

FDMC: Furan-2,5-dimethylcarboxylate

FFCA: 5-formyl-2-furancarboxylic acid

FWHM: Full Width af Half Maximun

HMF: 5-hydroxymethyl-2-furfural

HMFCA: 5-hydroxymethyl-2-furancarboxylic acid

HMMF: 5-hydroxymethyl methylfuroate

HRTEM: High Resolution Transmission Electron Microscopy

ICP-OES: Inductively Coupled Plasma-Optical Emission Spectrometry

IMP: Impregnation Method

KIE: Kinetic Isotope Effect

MAO: Methylaluminoxane

MC: Microencapsulated

MEP: Molecular Electrostatic Potential

MFCA: 5-(methoxycarbonyl) furan-2-carboxylic acid

MFF: Methyl 5-formyl-2-furoate

MNPs: Metal Nanoparticles

mol%: Molar Percentage

MTPs: Multi-Twinned Nanoparticles

MW: Microwave

PEI: Polyethyleneimine

PMMA: Poly(methylmethacrylate)

PSNPs: Polymer Supported Nanoparticles

PVP: Poly(*N*-vinylpyrrolidone)

QSEs: Quantum Size Effects

RD: Reduction-Deposition Method

SEM: Scanning Electron Microscopy

SPR: Surface Plasmon Resonance

sPS: Syndiotactic polystyrene

sPSB: Syndiotactic polystyrene-*co*-cis-1,4-polybutadiene

TEM: Transmission Electron Microscopy

T_g: Glass Transition Temperature

THF: Tetrahydrofuran

THQ: Tetrahydroquinoline

TOAB: Tetraoctylammonium bromide

TOF: Turnover Frequency

TON: Turnover Number

UV-VIS: Ultraviolet-Visible

XPS: X-Ray Photoelectron Spectroscopy

XRD: X-Ray Diffraction

WAXD: Wide Angle X-Rays Diffraction

wt%: weight percentage

CHAPTER 1

....

GENERAL PROPERTIES OF GOLD NANOPARTICLES

CHAPTER 1: GENERAL PROPERTIES OF GOLD NANOPARTICLES

1.1: INTRODUCTION TO METAL NANOPARTICLES

Metal particles, typically with dimensions smaller than 100 nm at least in one dimension, are defined metal nanoparticles (MNPs). Under these conditions, properties completely different from those of massive metal or molecular compounds are typically observed; these strongly depend on size, shape, interparticle distance and the nature of the material in which they are included (the support).[1] The peculiarity of these properties can be explained considering the quantum size effects (QSEs) and the surface plasmon resonance (SPR). Typically, massive metals are known to be electric conductors. Moving from bulk to nano-sized materials, the energy gap between the valence and conduction bands increases; for this reason the electrons are localized as in a molecular state and the MNPs behave as semi-conductors (**Figure 1**).
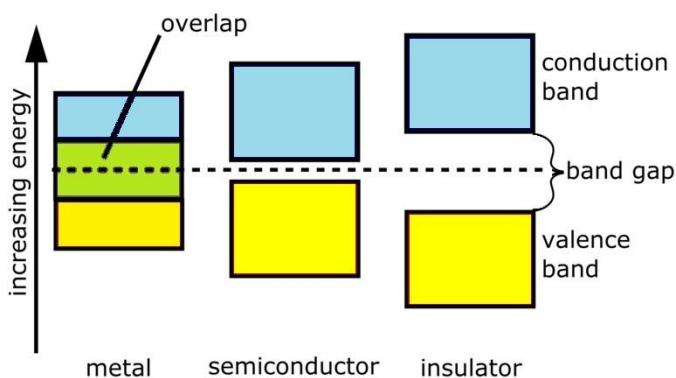
Figure 1: Different size of band gaps for conductors, semiconductors and insulators.

All the phenomena related to this energy gap are called QSEs and are generally observed when the de Broglie wavelength of the valence electrons is of the same order of the particle size.[2] The SPR is defined as the collective oscillations of the free electron gas located at the surface of the nanoparticle (plasmon) interacting with an oscillating electromagnetic field of the radiation having a wavelength comparable to the nanoparticles size (**Figure 2**).[3,4]
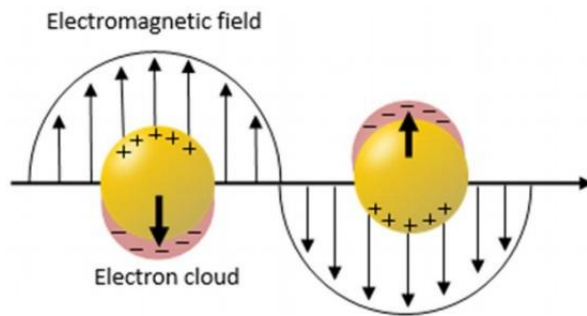
Figure 2: Example of Surface Plasmon Resonance effect in MNPs.

This resonant oscillation produces large wavelength-selective increase of absorption, scattering and electromagnetic field at the nanoparticle surface. Consequently, when something modifies the environment of the nanoparticle, this also affects the local SPR. For example, the colour of the MNPs depends on its size. Interestingly the peculiar plasmon

absorbance of MNPs has been exploited for a wide variety of applications[4] as e.g. chemical sensors, biosensors[5] and opto-electronic hybrids.[6]

1.2: PROPERTIES OF GOLD NANOPARTICLES

Gold nanoparticles (AuNPs,) also known as colloidal gold, are nanometre-sized particles of gold. The technological use of AuNPs can be traced back to the ancient Romans when they applied noble metals to stain glasses for decorative purposes: the first example is the Lycurgus Cup (**Figure 3**).[7] The SPR effects of the AuNPs included in the glass matrix turns the colour of the cup from greenish in reflected light to ruby red in transmitted light.
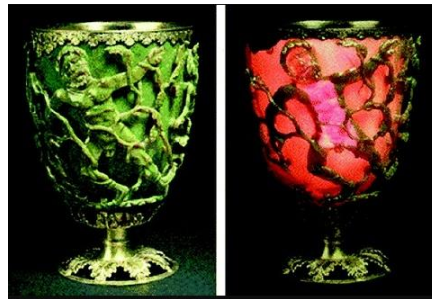
Figure 3: Effects of the light on Lycurgus Cup.

However, the real scientific potential of the AuNPs was not highlighted until the 1850s when the Michael Faraday's work showed the different optical properties of the AuNPs compared to bulk gold.[8] The physical-chemical properties, the catalytic activity and the applications of AuNPs depend on various factors such as size, shape, surface area, oxidation state and type of support; these features will be described in detail in the following paragraphs.

1.2.1: SIZE AND SHAPE

The effect of size on the catalytic activity and selectivity of MNPs based heterogeneous catalysts was extensively investigated by Toshima *et al.*[9] The catalytic activity generally increases (**Figure 4**) as the size of the MNPs is decreased because of the increase of the specific surface area.[10]
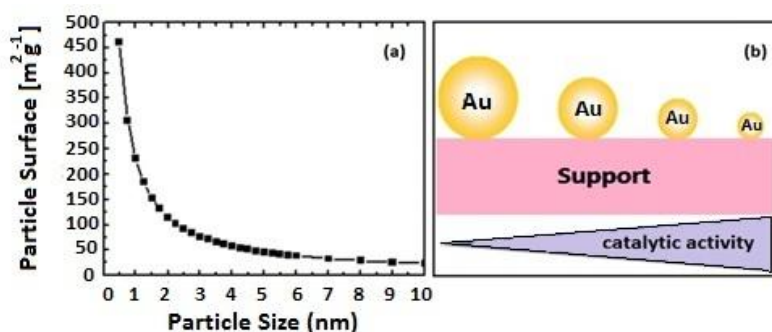
Figure 4: Relation between the sizes of AuNPs with (a) surface area (b) catalytic activity.[10]

In the pioneering study by Haruta on the low temperature oxidation of CO to CO_2 it was clearly demonstrated that the catalytic activity of the AuNPs dramatically depends on the size of the nanoparticles.[11]

Noble metals as gold tend to form spherical particles in face centered cubic (*fcc*) crystalline structure because of the high symmetry of this arrangement of the metal atoms and to minimize the surface area energy. Consequently, morphologies ranging from quasi-spherical to highly faceted particles, typically cubic or octahedral, are the most common for isotropic particles. However, small nanoparticles with size lower than 20 nm are not always found in the equilibrium shape and multi-twinned nanoparticles (MTPs), in five-fold symmetry, are also observed (**Figure 5**).[12]
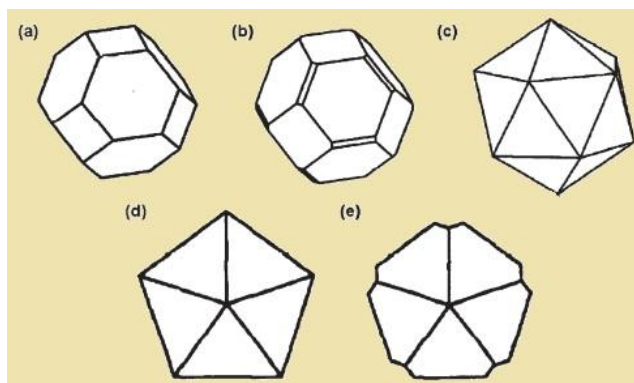
Figure 5: Common morphologies for metal nanoparticles having *fcc* crystalline structure: (a) truncated octahedron, (b) truncated octahedron with extra (110) truncations, (c) icosahedron, (d) regular decahedron (e) Mark's decahedron.[12]

In general the morphological control of AuNPs is not a simple matter since it depends on various factors such as the gold concentration in the feed, the type of support and presence of defects and impurities.[13]

1.2.2: OXIDATION STATE

The question about the oxidation state of catalytically active gold atoms in catalysis is largely unresolved. Small metallic cluster of Au(0), cationic gold species (Au(I) and/or Au(III)) or anionic gold species interacting with electron-rich metal defects on the support have been proposed.[14–17] For example, Kowalski *et al.*[18] have shown that for AuNPs supported on titanium oxide (110 surface) (AuNPs-TiO_2), the gold atoms adsorbed at a bridge site between the surface oxygen and first-layer of titanium ions do not change the oxidation state of titanium (Ti^{4+}). On the other hand, when gold is adsorbed on the top of oxygen atoms, there is a charge transfer from metal to surface, which implies the reduction of a second-layer titanium ions (formally Ti^{3+}) and the formation of a positive charge on gold ($Au^{\delta+}$) (**Figure 6**). Therefore, the site at which the Au atoms are adsorbed as well as the nature of the supports are important for the oxidation state of AuNPs.
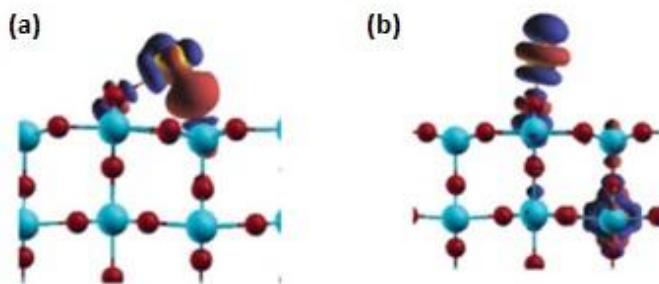
1.2.3: EFFECT OF THE SUPPORT

As previously described, the nature of the supports is very important. One of the roles of the support is to prevent the sintering of AuNPs occurring during the catalyst preparation or a catalytic process. The use of porous support such as e.g. porous metal oxides and polymers, or mesoporous silica allows regulating the dispersion of the nanoparticle and to prevent their agglomeration or coalescence.[19] Furthermore the support enhances the thermal stability of the catalyst reducing the costs, and provides improved surface area characteristics. In addition, the support is believed to play an active role in catalysis. The oxygen vacancies on the surface of metal oxides supports have a role in activating gold.[20] Rodriguez *at al* [21,22] pointed out that oxygen vacancies in cerium oxide (CeO$_2$) catalyze decomposition of sulfur dioxide (SO$_2$) and dissociation of water in AuNPs-CeO$_2$ (111). Metal oxides such as MnO$_2$, CeO$_2$ and Fe$_2$O$_3$, where the metal

exhibits two accessible and stable oxidation states, are active in redox cycling of the metal ions, allowing a stabilization of positive gold species.[23,24] Corma *et al.*[25] showed that the catalytic activity of AuNPs in the aerobic cinnamyl alcohol oxidation reaction is strongly dependent on the nature of the support. A series of supported gold catalysts with the same gold content (1.5–2 wt%) and particle size (3–4 nm) were compared using different supports (NP-CeO$_2$, CeO$_2$, TiO$_2$, Carbon) under the same reaction conditions (**Figure 7**); the AuNPs-NPCeO$_2$ showed the best catalytic activity. According to the mechanisms shown in **Figure 8**, the oxidation run proceeds through three reaction steps: i) the formation of alcoholato species bound to positive charged gold atoms that act as Lewis-acid sites; ii) the β-hydride shift from the carbinolic carbon atom to the gold surface; iii) oxidation of the metal-hydride to form water and restore the metal site.
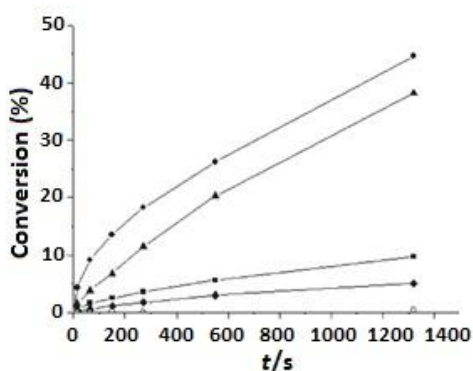
Figure 7: Time-conversion plot for cinnamyl alcohol oxidation with ●AuNPs-NPCeO$_2$, ▲AuNPs-CeO$_2$, ■AuNPs-TiO$_2$, ◆ AuNPs-Carbon, ○without catalyst.[25]

The NP-CeO$_2$ support allows the stabilization of the positively charged gold species through a strong ionic bond interaction and the oxygen vacancies on the surface of the support contribute to the absorption-activation of the oxygen, promoting the oxidation of the Au-H intermediate species; the synergic effect of these properties explains the higher activity of AuNPs-NPCeO$_2$ catalyst compared to the other metal oxides.
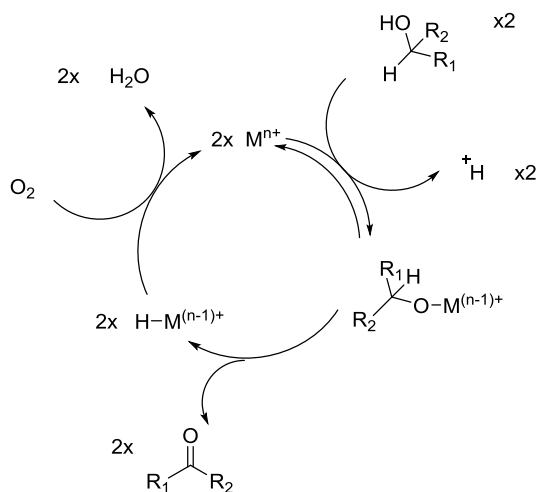
Figure 8: proposed mechanism for the AuNP-NPCeO$_2$ catalyzed aerobic oxidations of alcohols.[25]

Polymeric supports can also play different roles in AuNPs synthesis:[26] they can simply stabilize the AuNPs or act as template or reducing agent. When poly(N-vinylpyrrolidone) (PVP), polyethylene glycol (PEG), polyvinyl

chloride (PVC), starch or chitosan are applied, the size, shape and morphology of the resulting nanoparticles are dramatically affected by the nature of the polymeric stabilizer because of the different surface energy of the NPs and thus, the growth direction of the different faces of the NP surface. The polymeric stabilizer prevents agglomeration of the NPs via steric or electrostatic effect, as shown in **Figure 9**.
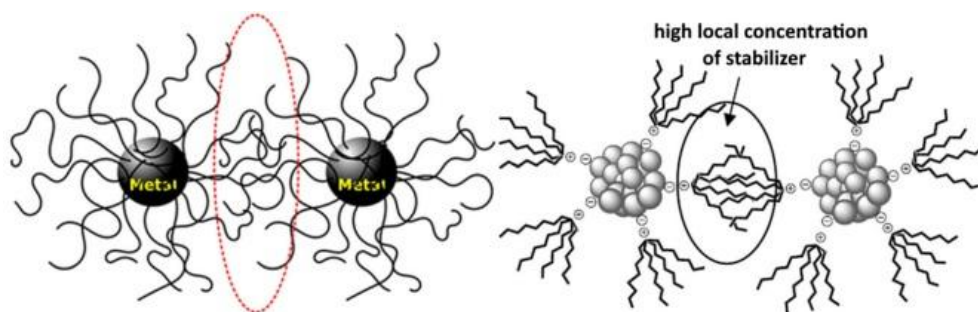
Figure 9: steric (left) and electrostatic (right) stabilization of MNPs by polymers.[26]

Poly(N,N-diethylacrylamide) microgels can work as template determining both size and shape control in AuNPs synthesis.[27] In this case, the formation of the AuNPs depends on solvent and swelling state of the microgels; the environment of the internal space of the gel, the concentration of the Au^{n+} cation and the crosslinking density of the microgel, all control the size of the resulting AuNPs.

The polymeric support can also affect the catalytic activity. The polymer swelling can influence the diffusion rate of the substrates and their accessibility to the catalytic sites. In other cases, the microscopic morphologies can affect the reactivity and selectivity of the reaction pathways. E.g. Kobayashi reported the selective aerobic oxidation of alcohols and aldehydes to the corresponding methyl esters catalyzed by AuNPs supported on polystyrene-based polymers[28] under mild conditions (room temperature; atmospheric pressure of oxygen).

1.3: CATALYSIS PROMOTED BY AuNPs

Bulk gold was for long time considered poorly reactive since it is resistant to oxygen corrosion and is not reactive with sulphides at any temperature; for this reason, it is found in nature as nuggets. Moreover, gold has a low tendency to chemisorb reagents onto the surface, an essential feature in heterogeneous catalysis by metals. Recently the AuNPs have been recognized as surprisingly active and extraordinary effective green catalyst. The first example was reported in 1972 by Bond *at al* [29] where Au(0) supported on silica or γ-alumina was found active in the hydrogenation of alkenes and alkynes under mild conditions. Shortly later, Hutchings[30] and Haruta[31] reported that AuNPs are catalytically active in hydrochlorination of acetylene and oxidation of carbon monoxide to carbon dioxide at low temperature, respectively.
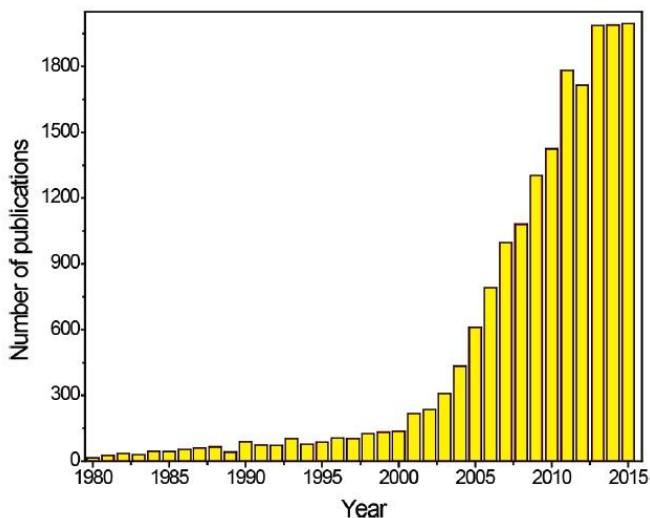
Since then, the gold rush in catalysis get started and the number of publications about the use of heterogeneous gold catalysts is constantly increasing (**Figure 10**). Nowadays, AuNPs act as incredible catalysts in many organic reactions[14,24,32] and catalytic processes, some of which of industrial application.[33,34] The use of the AuNPs catalysts offers many advantages compared to the homogeneous counterpart. One of the most important is the easy recovery from the reaction medium and the possibility of reuse. Moreover heterogeneous gold catalysts are biocompatible, non-toxic, not air-sensitive and usually active under mild conditions in agreement with the principles of Green Chemistry[35] (**Figure 11**); AuNPs catalysts are thus of particular interest in pharmaceutical industry and biomedical applications.[36]

Figure 11: Principles of Green Chemistry.

A general scheme of the reactivity patterns catalyzed by AuNPs is shown in **Figure 12**; these processes generally consist of oxidation and hydrogenation reactions, nucleophilic additions to carbon-carbon multiple bonds and activation of carbonyl groups and alcohols.[37] AuNPs are particularly active in the epoxidation of alkenes, oxidation of alcohols and low temperature CO oxidation. Special interest is deserved to the oxidation of propene to propene oxide, a commodity chemical used in the manufacture of polyurethane and polyols. Haruta *et al.* showed for the first time the potential of the AuNPs in such reaction, achieving a selectivity of 99% at a conversion of only 1% using oxygen as oxidant and hydrogen as reductant at relatively low temperature.[38] The epoxidation of ethylene can be selectively accomplished using AgNPs but the epoxidation of propene resulted more challenging; these disappointingly results arise many unresolved questions about the AuNPs performances in this process.[39]
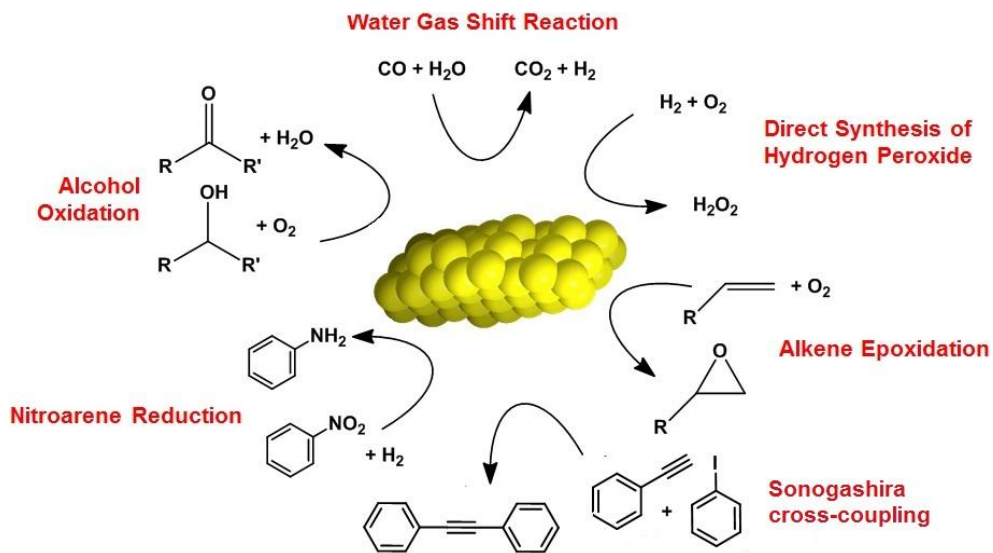
Figure 12: reactions catalyzed by AuNPs.

Hydrogenation of alkenes and alkynes was one of the first processes to be catalyzed by AuNPs; since then, AuNPs have been employed in the selective hydrogenation of α,β-unsaturated carbonylic compounds to α,β-unsaturated alcohols and in the reduction of nitro groups in the presence of other reducible functionalities. AuNPs are also a promising catalyst in the direct synthesis of hydrogen peroxide (H_2O_2), currently produced at industrial scale with the anthrahydroquinone route. The direct synthesis of H_2O_2 from H_2 and O_2 at low temperatures is, in principle, a valid and sustainable alternative to this process;[40] another reaction pathway involves the reaction of O_2 with water catalyzed by the photoactive AuNPs-TiO_2 catalyst,[41] or with hydroxylammonium salt (or

hydroxylamine) using AuNPs supported on rare earth oxides (La_2O_3 or Gd_2O_3).[42]

[Au] is a soft Lewis acid showing high affinity for the carbon-carbon multiple bond of alkynes, allenes or olefins; coordination of the π-system to the metal leads to the formation of adducts that make the substrate active toward the nucleophiles attack (**Figure 13**).
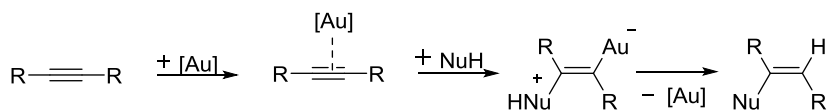
Figure 13: mechanism for the gold catalyzed nucleophilic addition to carbon-carbon multiple bonds.

This result paved the way to a large variety of possible reactions, comprising hydroamination, hydrosililation, hydrochlorination, hydroalkoxylation, hydrothiolation and coupling reactions.[24,32,37]

1.3.1: BIMETALLIC Au&M CATALYSTS

Sometimes the application of monometallic AuNPs catalysts in the industrial field is limited by several factors. Very small AuNPs (typically < 5 nm) and a strict control of the particle growth during synthesis and

catalytic runs limit their application in high-temperature processes where aggregation phenomena can occur. Metal oxide supports are often required for increasing the thermal stability of the catalysts and, in some cases, lead to oxygen activation in oxidation catalysis.

To overcome some of these limitations, the researchers aimed to introduce new tricks to improve the catalyst performances. Alloying gold with other metals can tune the electronic properties of the metal and produce interesting reactivity patterns not observable with the monometallic catalyst. The Au&M bimetallic catalysts show in most cases better performances in terms of activity, selectivity and durability, due to a synergistic effect of the two metals similarly to as the ligand can modify the electronic properties and the steric hindrance at the metal center in homogenous catalysis. The superior performances of the Au&M catalysts compared to the Au counterpart have been reported for different chemical reactions; examples include CO oxidation, selective oxidation of alcohols to aldehydes, synthesis of hydrogen peroxide and biomass conversion into fuels and chemicals.[43,44] The bimetallic catalysts can be classified, on the basis of their morphology, in: *i)* core-shell segregated nanoparticles (**a**, **Figure 14**), consisting of a core of metal A (red) surrounded by a shell of metal B (yellow); *ii)* subcluster segregated nanoparticles (**b**, **Figure 14**) consisting of nanoparticles A and B subclusters, that share a common interface; *iii)* mixed (ordered or random) A-B nanoparticles (**c**, **Figure 14**); *iiii)* multishell nanoparticles (**d**, **Figure 14**) that have layered or onion-like alternating -A-B-A- shells.[45]
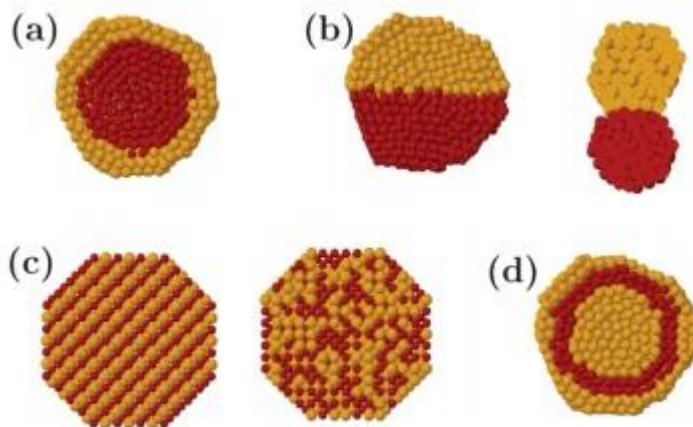
Figure 14: Representation of mixing patterns: a) core-shell, b) subcluster segregated (b), c) mixed, d) multishell.[45]

Different bimetallic Au&M catalysts have been synthetized and classified on the basis of the metal characteristics: 1) Gold-base metals (Au-BM) where BM refers mainly to Cu, Ag, Co and Ni; 2) Gold-platinum group metals (Au-PGM) where PGM refers to Pt, Pd, Rh and Ir.[46] A clear example of the synergistic effect of Au-BM catalysts is the low temperature CO oxidation. The catalytic activity of AuNPs catalysts is strongly influenced by the size of the NPs where diameters ranging from 2 to 5 nm are the most active.[47] For the Au-BM catalysts, Mou and co-workers[48] reported a remarkable catalytic activity with Au&Ag of 20-50 nm supported on mesoporous aluminosilicate (Au&Ag-MCM) where the high catalytic activity is independent of the NPs size and results from the ability of Ag to activate O_2.

The use of Au-PGM catalysts is profitable in hydrogenation reactions. AuNPs are less reactive than PGMs in hydrogen activation but exhibit higher chemoselectivity in the reduction of functional groups. The addition of small amount of PGM to Au catalysts allows to improve the hydrogenation activity retaining high chemoselectivity. Corma *et al.* reported a selective hydrogenation of 3-nitrostyrene into 3-vinylaniline catalyzed by Au&Pt-TiO$_2$:[49] the high chemoselectivity is attributed to the preferential adsorption and activation of the nitro group at the Au–Ti interface.
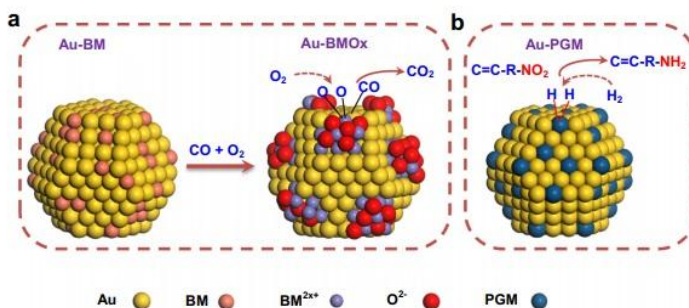
Figure 15: synergistic effects of bimetallic Au-M catalysts: a) Au-BM in CO oxidation; b) Au-PGM in selective hydrogenation of nitroaromatics.[46]

CHAPTER 2

....

SYNTHESIS AND CHARACTERIZATION OF GOLD NANOPARTICLES CATALYSTS

CHAPTER 2: SYNTHESIS AND CHARACTERIZATION OF GOLD NANOPARTICLES CATALYSTS

2.1: GENERAL APPROACHES TO THE AuNPs SYNTHESIS

The most common protocols are generally categorized into top-down protocols, involving the grinding of bulk material into smaller pieces down to the nanometric scale, or bottom-up protocols where the nanoparticles are synthesized from metal salts or molecular seeds that nucleate to form nanostructures.[50] In both methods, chemical, physical and biological techniques can be used; each method offers some specific advantages and disadvantages.[51]

2.1.1: CHEMICAL METHODS

Chemical methods are the most common procedures where generally the preparation of AuNPs includes two main processes. One is the reduction of the gold precursor, typically $HAuCl_4$, $NaAuCl_4$ or LAuX (L= PR_3; X=Cl) by sodium borohydride ($NaBH_4$), hydrazine, hydroxylamine, polyols, citric or oxalic acids to promote nanoparticle nucleation. A problematic issue is that the most efficient reducing agents such as $NaBH_4$ and hydrazine are biologically and environmentally toxic. The reduction reaction is followed by the addition of a stabilizer containing sulfur, phosphorus, nitrogen or oxygen donor atoms, or polymers and surfactants to avoid aggregation of the metal particles. More explored is the use of inert porous supports

because of their stability, high efficiency and excellent control of the AuNPs size.[52]

The Turkevich method[53] was the first chemical method to be proposed in the literature. It consists of the reduction of $HAuCl_4$ with citrate in water (**Figure 16**) where citrate acts as both reducing and stabilizing agent and the resulting diameter of the AuNPs is of about 20 nm. Later on, in 1973, Frens modified this method to obtain AuNPs with size in the range from 15 to 150 nm.[54] Considerable efforts have been produced in the last decades to clarify the effect of pH, temperature, citrate or gold concentration on the dimensional and morphological characteristics of the resulting AuNPs.[55]
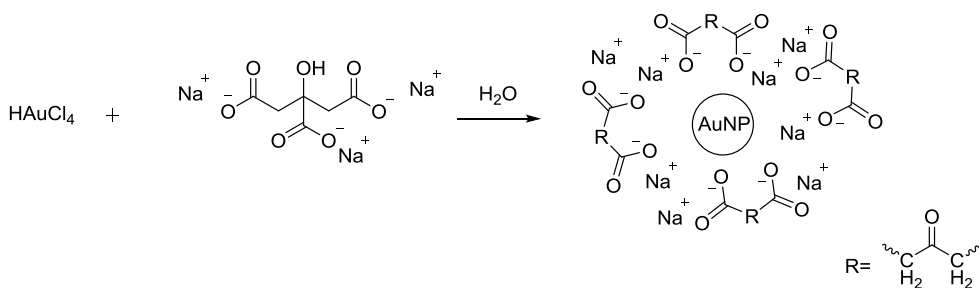
Figure 16: Synthesis of AuNPs using the Turkevich method.

 The Brust-Schiffrin method[56] discovered in 1994 allows the synthesis of thermally stable and air-stable AuNPs of controlled size (1.5 - 5.2 nm) with low dispersity. The procedure involves the reduction of $HAuCl_4$ with

NaBH$_4$ in a mixture of water and toluene, in the presence of a phase transfer agent such as tetraoctylammonium bromide (TOAB) and thiols as capping agents (**Figure 17**).
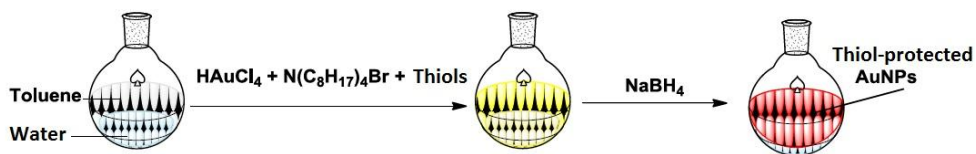
Figure 17: Synthesis of AuNPs using Brust-Schiffrin the method.

Thiol-protected AuNPs can be purified, dried and redissolved, without changing the size of the nanoparticles. This method was also developed with other gold precursors, capping agents and reducing agents in a single liquid phase, avoiding the use of phase transfer agents. Furthermore, gold complexes with thiolate or phosphine ligands do not need capping agents since they play also this role.[2,57]

2.1.2: PHYSICAL METHODS

Physical methods are based on the energy transfer by ionizing or non-ionizing radiation, photochemical processes and microwave radiation;

this can lead to the nucleation of metallic particles through reduction pathways.

The photochemical synthesis simultaneously activates the nucleation and growth processes. Irradiation with ultraviolet (UV) light leads to the reduction of the gold complexes to the metallic state in presence of acetone or ascorbic acid as source of electrons. These processes are carried out in organic solvents or aqueous solution, using polymers, dendrimers or surfactants to form micelles as soft templates to prevent the coalescence of smaller gold particles (**Figure 18**). However, this method is very sensitive to pH, temperature, irradiation time and surfactants or $HAuCl_4$ concentration.[58,59]
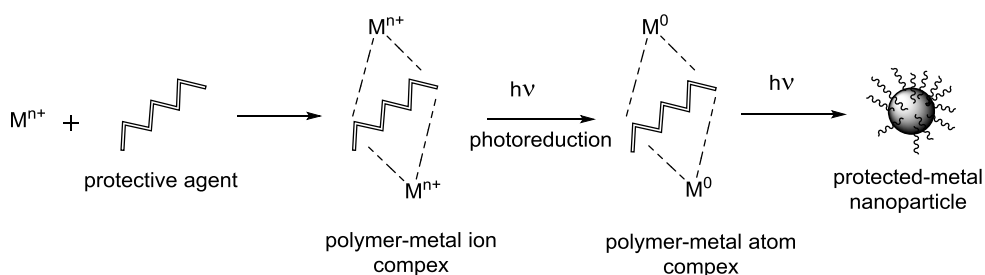
Figure 18: Photochemical reduction of metal salts in the presence of a polymer.

Irradiation of aqueous solution with high-energy ionizing radiation, generally γ-ray, allows generating transient radicals, through water radiolysis containing both reducing and oxidizing species. The addition of

42

e.g. 2-propyl alcohol decomposes the oxidizing species while the reducing radicals reduce the metal ions to metal atoms. The coalescence of metal atoms to form MPs in the presence of a capping agent (**Figure 19**)[60] is carried out at very mild conditions (ambient pressure, room temperature) and yields uniformly disperse AuNPs. Also in this case, the solvent, pH, metal precursor concentration and the absorbed dose do influence the characteristic of the final products.[61]
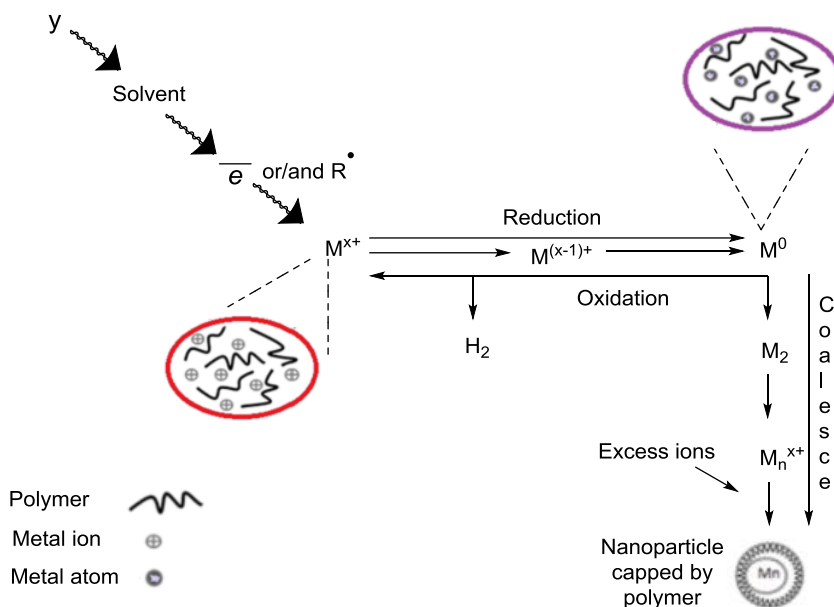
Figure 19: Metal ion reduction by ionizing radiation in the presence of stabilizer.

In microwaves radiation the reducing species are formed in situ as a result of the interaction with the reagents. This allows the reduction of gold ions to metallic gold to produce first nucleation and finally the AuNPs; the stabilization is controlled through the presence of passivating agents. Considering that there is no need of additional reducing agents, this method can be considered "*green*" because it avoids the formation of contaminants. This process requires relatively short time, allowing a good control of size distribution of the AuNPs. The solution is directly heated by the radiation instead of conventional heating by thermal sources, determining higher temperature homogeneity in the reaction mixture.[62,63]

2.1.3: BIOLOGICAL METHODS

Enzymes, microorganisms, plants or plants extracts have been exploited for the synthesis of MNPs. Among them, the use of plants, or plants extracts, is preferred because of their availability, low cost, eco-friendliness and non-toxic nature.[64] Generally, the procedure involves an extraction in a green solvents of different part of the plants, namely leaf, root, shoot, petal, fruit and peel; the extract contains both the reducing and capping agents necessary for the reduction of the metal ions. Example of reactive compounds are: flavonoids, phenols, carboxylic acids, amino acids, ketones and proteins. The reaction begins by contacting the mixture of the metal precursor with the plant extracts at

room temperature. The reaction rates are relatively high, from several minutes to hours, depending on the amount and the type of plants.[65] Fresh as well as dried plants can be used; of course, the effects of seasonal variations can lead to variations in plant constituents. The size and morphology of AuNPs are controlled by various factors such as temperature, pH concentration of the extract and concentration of the metallic ions.
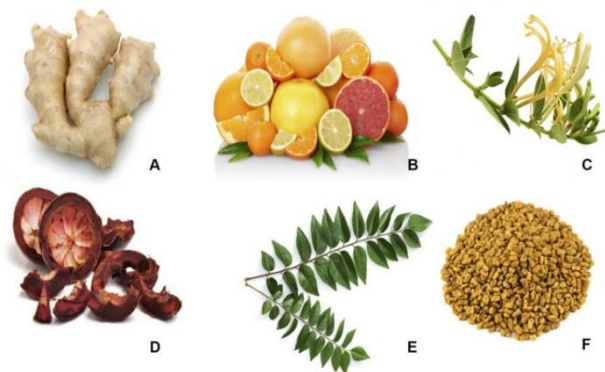
Figure 20: examples of plants used to synthesize AuNPs (A) Zingiber officinale, (B) Citrus, (C) Lonicera Japonica, (D) Garcinia mangostana, Murraya koenigii Spreng, (F) Abelmoschus esculentus.[64]

2.2: SYNTESIS OF AuNPs SUPPORTED ON INORGANIC COMPOUNDS

Different inorganic compounds have been used as effective supports in the AuNPs preparation and stabilization; the strong interactions between the AuNPs and support produces high thermal stability. The most used are: titanium oxide (TiO_2), alumina (Al_2O_3), cerium oxide (CeO_2), magnesium oxide (MgO), silica (SiO2), ferric oxide (Fe_2O_3) and zeolites. Different method of preparation can be used for the synthesis of AuNPs on these supports and the most important are briefly discussed below.

2.2.1: IMPREGNATION METHOD

The impregnation method (IMP)[10,19,66] is one of the most used to support AuNPs because of its versatility (different types of metal oxides), simplicity and low cost. Generally, the support is suspended in a large volume of the gold precursor solution ($HAuCl_4$, $AuCl_3$, Au_2Cl_6); then the solvent is slowly evaporated, and the support is calcinated under suitable thermal conditions (**Figure 21**). This IMP is called *wet impregnation*. Another possibility is the *incipient wetness technique* where only the pores of the support are filled with the solution of the gold precursor. The AuNPs obtained from this approach has a wide size distribution, ranging from 2 to 30 nm. Since gold salts interact only weakly with the support, there is not a good dispersion during calcination and the particles suffer

of severe agglomeration side reactions. The characteristics of the final catalyst depend on time of heating, calcination temperature and type of support. Supports such as MgO and Al_2O_3 are not appropriate since they are soluble in strongly acidic solution like gold salts solution.
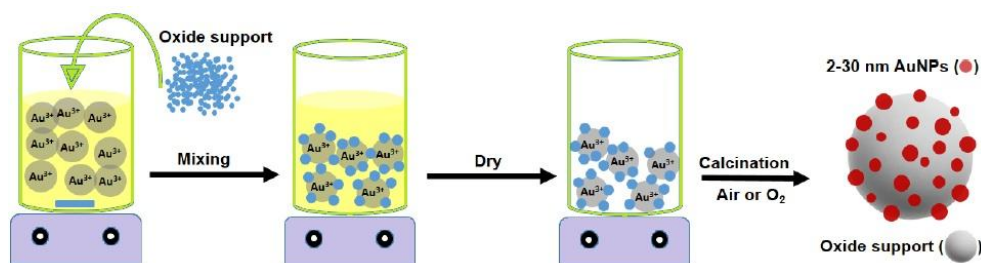
Figure 21: preparation of AuNPs via Impregnation method.

2.2.2: CO-PRECIPITATION METHOD

The co-precipitation method (CP)[10,19,66] was for the first time discovered in 1987 by Haruta[31] and consists in the simultaneous precipitation of both the inorganic support and gold. The aqueous solution of the gold precursor (generally $HAuCl_4$) is treated with a water-soluble metal salt (e.g. nitrate), in aqueous alkaline solution (Na_2CO_3 or NH_4OH or NaOH). The hydroxide and/or carbonate species are precipitated simultaneously, and the resulting slurry is filtered, washed and dried prior calcination (**Figure 22**). The resulting AuNPs have an average size of 2-3 nm and are uniformly dispersed. The relative precipitation rate is the main parameter

to be controlled. Limitation are; i) few metal hydroxides or carbonates can be co-precipitated with $Au(OH)_3$; ii) different salts are obtained as by-products and they can act as catalyst poisons if not removed correctly in the washing step.

Figure 22: preparation of AuNPs via Co-Precipitation method.

2.2.3: DEPOSITION-PRECIPITATION METHOD

In 1991 Haruta group[67] discovered the Deposition-Precipitation method (DP).[10,19,66] In this approach the insoluble oxide support is added to a solution of the gold precursor ($HAuCl_4$). Alkali (Na_2CO_3 or NaOH) are added to this slurry to rapidly change the pH value (in the range of 6 to 10) and allow the precipitation of the hydroxide species. The surface of the support acts as nucleating agent and most of the active precursors end up being attached. The resulting mixture is then subject to repeated sequences of filtration and washing and a flow of H_2 is applied to reduce the Au(III) ions into AuNPs (**Figure 23**). The key point of this technique is

the control of the pH value. The AuNPs are highly dispersed with particle sizes of 2-3 nm and unlike the CP methods are mostly located at the surface of the support. This method is appropriate for metal oxides but it is not very suitable for activated carbon or zeolites due to their high isoelectric point, even if after an acidic treatment some better results are showed.[68,69]
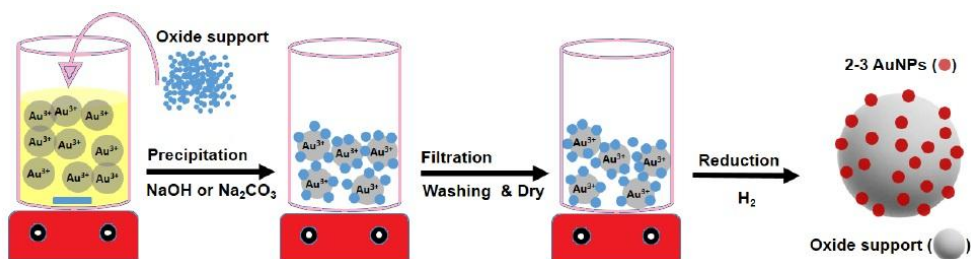
Figure 23: preparation of AuNPs via Deposition-Precipitation method.

2.2.4: REDUCTION-DEPOSITION METHOD

In this procedure,[19] the gold ions are first reduced to colloidal gold with the chemical method discussed above (Turkevich-Frens or Brust-Schiffrin methods). Then the support is impregnated with the AuNPs adsorbing them and the resulting material is filtered, washed and dried (**Figure 24**). The most important feature is the adsorption of AuNPs to the support, which requires strong adsorption capacity and large surface area of the support.
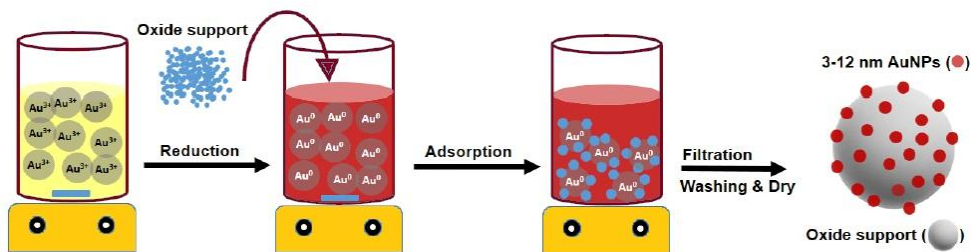
Figure 24: preparation of AuNPs via Reduction-Deposition method.

2.3: SYNTESIS OF AuNPs SUPPORTED ON ORGANIC POLYMERS

The use of organic polymers and biopolymers can offer considerable advantages compared to inorganic supports.[70,71] They are commercially available or readily synthesized and functionalized with conventional polymerization techniques; variations of the chemical environment of the AuNPs allow to change selectivity and solubility of the catalyst. When the polymeric support is undergone to covalent crosslinking, higher thermal stability is obtained and the MNPs sintering is hampered. Moreover, the swelling or softening of the polymeric support in appropriate solvents can modulate the access of reagents to catalytic sites. All of the previously described methods have been applied to the preparation of AuNPs embedded in organic polymers, the main difference consisting in the thermal treatment that is typically carried out at lower temperature. The reducing agents typically employed are $NaBH_4$ or alcohols, carboxylic acids or the polymer itself.[72] The synthetic routes can be divided into two categories: ex-situ and in-situ.
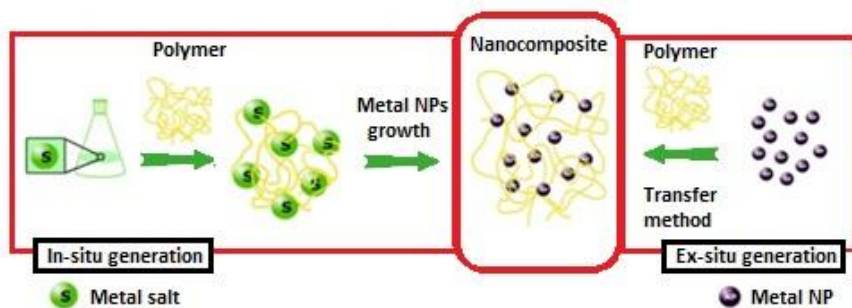
2.3.1: EX-SITU SYNTESIS

In this process, MNPs are physically entrapped in the polymer or biopolymer network (**Figure 25**). At first, the preformed MNPs are dispersed in a polymer solution and then the physical entrapment can be performed by casting and solvent evaporation or chemical polymerization. Different types of polymer supported nanoparticles (PSNPs) were prepared by ex-situ synthesis.[73] dos Santos *et al.* showed that AuNPs can be embedded in chitosan films.[74] The synthesis is done in very mild condition. $HAuCl_4$, dilute acetic acid as reducing agent and chitosan are first pre-mixed at 85°C; then the suspension is cooled at room temperature, casted onto glass substrates and left dry to obtain thin films. Similarly, Chatterjee *et al.* reported the synthesis of films using pre-synthetized Au&Ag NPs.[75] In this case, the pre-formed MNPs were dispersed in THF in presence of polymethyl methacrylate (PMMA) and the suspension was concentered by slow solvent evaporation. The resulting

solution was deposited onto glass slide and dried at room temperature to obtain transparent films. The ex-situ method is very common because it allows the use of various types of nanoparticles and host polymers; in addition, the physical entrapment allows to stabilize the MNPs. However, the formation of a homogeneous dispersion of an inorganic material in the polymer solution is still a challenging process.

2.3.2: IN-SITU SYNTESIS

Unlike the previous method, with in-situ approach the MNPs are synthesized from precursors and trapped inside the polymer phase though appropriate reactions (**Figure 25**).[56] In this case, the polymer acts as a nano-reactor providing a limited environment for the synthesis and stabilization of MNPs. The advantages of such method compared to the ex-situ are that the size and shape of nanoparticles are better controlled. Different factors influence the nature of the PSNPs: the nature of the polymer, the type of metal precursor and the reaction conditions. In particular, the in-situ processes can be divided in two categories: (i) sorption followed by redox and/or precipitation reaction; (ii) impregnation followed by redox and/or precipitation reaction.

In the first case the metal precursor is first adsorbed on the polymer and then the MNPs are performed by a reduction (or oxidation) of the metal ions or an in-situ precipitation. Generally, chemical interactions between

the metal and the functional groups of the polymers are involved. In Schauer group the synthesis of AuNPs in chitosan matrix or carboxy methyl chitosan matrices is reported.[76] In this case, amines and amides of chitosan and alcoholic groups in carboxy methyl chitosan yield metal ions chelation and nanoparticles immobilization. The synthesis is performed by dissolving $AuCl_3$ in the polymer solution and then chitosan leads to the reduction to yield the AuNPs formation.[77]

A

R = H or acetyl

B

R = H or acetyl or
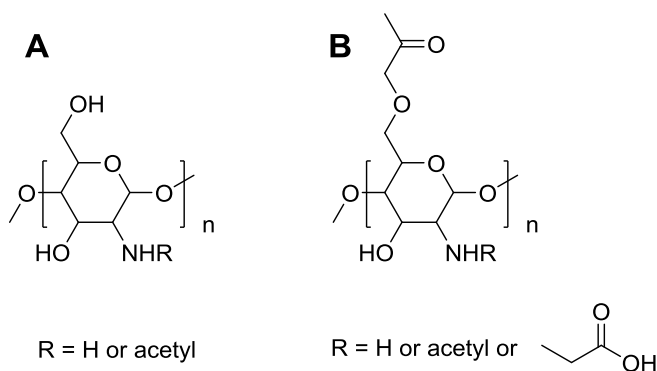
Figure 26: (A) chemical structure of chitosan, (B) chemical structure of carboxy methyl chitosan.

In the second case, the incorporation of metal precursor does not involve chemical interactions between the metal and the polymer. The impregnation can be performed by dissolving the polymer and the metal precursor in a solvent or by soaking the polymer with the metal precursor.

2.3.3: AuNPs CATALYSTS SUPPORTED ON ORGANIC POLYMERS

The first example of a polymer-supported gold catalyst was provided by Deng *et al* [78] who used a cation-exchange resin as a polymer support. The resin was pretreated with NaOH and then impregnated with a $HAuCl_4$ solution followed by drying: this catalyst was applied in the synthesis of carbamates from amines, carbon monoxide and molecular oxygen.
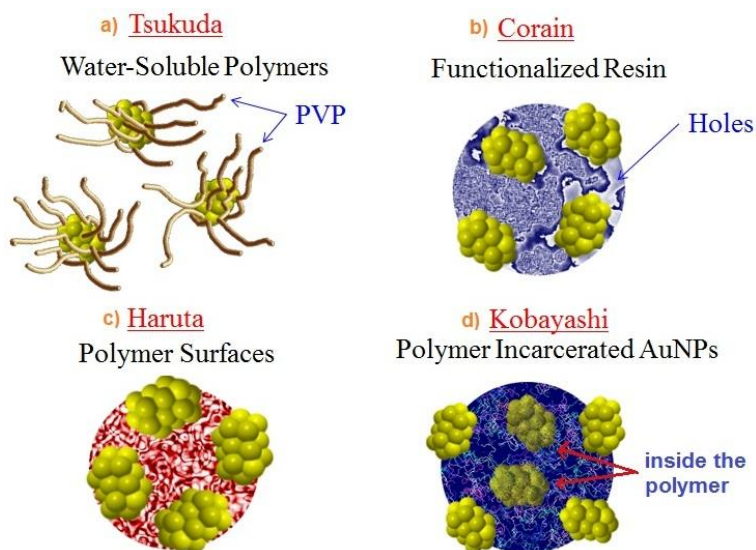
Figure 27: example of polymer stabilized AuNPs a) colloidal solutions of AuNPs with soluble polymer; b) AuNPs stabilized with porous resin; c) AuNPs located at the surface of the polymer; d) AuNPs embedded into a polymeric matrix.

In 2005 Tsukuda *et al.*[79] reported poly(*N*-vinylpyrrolidone) (PVP) as support of AuNPs (**a**, **Figure 27**). In this case, the gold catalyst was prepared by contacting an aqueous solution of NaBH$_4$ with an aqueous solution of HAuCl$_4$ and PVP at 0°C, to form a colloidal solution of AuNPs with an average diameter of 1.3 nm. This catalyst was found active in the aerobic oxidation of benzylic alcohols in water. The size effect was also investigated by testing, in the same reaction condition, the catalytic activity of this catalyst compared to an analogue where the average diameter of the AuNPs was of 9.5 nm. In this case, the smaller AuNPs exhibit higher catalytic activity.

Corain *et al.*[80] reported the synthesis of AuNPs supported on porous resin (**b**, **Figure 27**), with a moderate cross-linking degree, consisting of poly-2-(methylthio)ethylmethacrylate-*N*,*N*-dimethylacrylamide-*N*,*N'*-methylenebisacrylamide (4, 8, 88 mol%) (MTEMA–DMAA-4–8) (**Figure 28**).
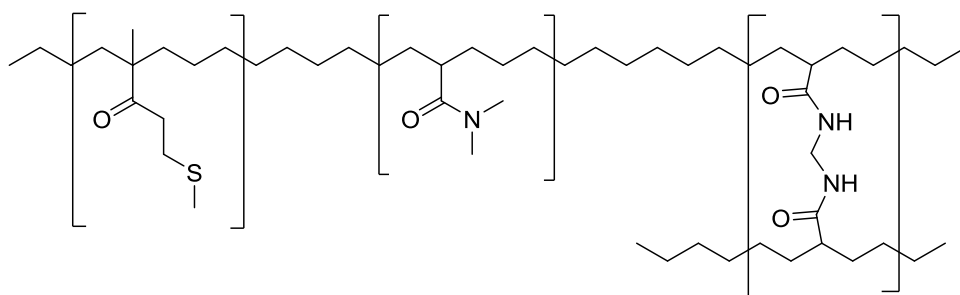
Figure 28: structure of MTEMA-DMAA-4-8 resin.[80]

The resin was suspended in MeCN containing AuCl$_3$ and left under stirring for 4 days. The thioethere units coordinates Au(III), thus homogeneously dispersing the metal. The metalated resin was recovered and suspended in water and then reduced with NaBH$_4$. This catalyst was found active in the oxidation of pentanal to pentanoic acid by dioxygen. An important feature is that the crosslinking degree influences the porosity of the polymer structure; consequently it is possible to control the size of AuNPs.[81]

Haruta *at. al.*[82] reported a method to support AuNPs on the surface of an anion-exchange resin (**c**, **Figure 27**) containing reducing functional groups (generally amino group, ammonium group or hydroxyl group) suitable for gold reduction and stabilization of the AuNPs. The resin is dissolved in aqueous alkali hydroxide solution, then added to an aqueous solution of the gold precursor and the mixture is left under stirring without further addition of reducing agents or heating. This catalyst is active in the oxidation of glucose to gluconic acid.

(x / y / z   28:34:38)
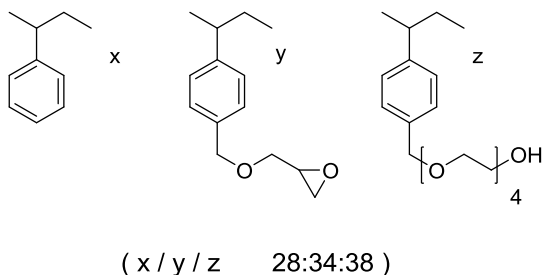
Figure 29: AuNPs stabilized with crosslinked polystyrene matrix.[83]

Another example is provided by Kobayashi (**d**, **Figure 27**).[83] In this case, polystyrene functionalized with alcohol and epoxide moieties in the side chain (**Figure 29**) is treated with the gold precursor [AuClPPh$_3$] and then reduced with NaBH$_4$ in THF at room temperature. Hexane is added to coagulate the polymer hybrid and the compound separated by filtration and heated at 150°C to cross-link the side chains and give the final polymer-incarcerated gold catalyst. The polystyrene matrix stabilizes the naked gold clusters via the aromatic rings of the polymeric chain. The catalyst was employed in the aerobic oxidation of several alcohols, under air or oxygen atmosphere at room temperature.

2.4: GOLD NANOPARTICLES EMBEDDED IN POUROUS SUPPORTS

A porous material is definite as a solid that has an interconnected network of pores. Many substances such as clays, rocks, ceramics, metal oxides, carbonaceous materials, polymers can be considered as porous media. According to their size, the pores are classified in: micropores (diameters smaller than 2 nm), mesopores (diameters between 2 and 50 nm) and macropores (diameters larger than 50 nm).[84] Furthermore based on their accessibility, the pores can be distinguished in *closed pores* (totally isolated and inaccessible) and *open pores* (which are accessible from the external surface of the material). The first ones influence the macroscopic properties of the material, such as bulk density, mechanical strength and thermal conductivity. The second ones are also active in

processes such as fluid flow and adsorption of gases.[84] Porous materials provide some benefits when used as supports for AuNPs. First of all the presence of pores can prevent the agglomeration and leaching of gold by incorporation of AuNPs; furthermore the pores can act as template and control the size of AuNPs during their synthesis.[85] The pores can affect also the selectivity of the catalytic process, controlling the type of molecules that can access the pores and migrate through them. A huge variety of porous materials has been utilized as support for the preparation of gold nanoparticles but carbonaceous materials, metal oxides and polymers are the most common examples.[85]

2.4.1: SYNDIOTACTIC POLYSTYRENE-*CO*-CIS-1,4-POLYBUTADIENE

Syndiotactic polystyrene-*co*-cis-1,4-butadiene (sPSB, **Figure 30**) has been employed as crystalline porous support for AuNPs (AuNPs-sPSB). This catalyst was successfully used in various catalytic reaction.[86–89]
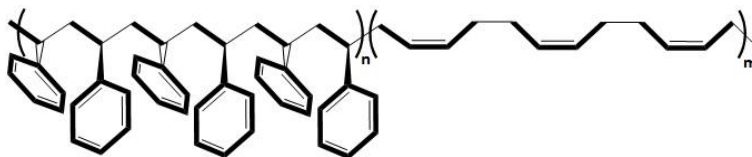
Figure 30: structure of sPSB polymer.

The sPSB is a linear *multiblock co*-polymer obtained by copolymerization of styrene and 1,3-butadiene, catalyzed by CpTiCl$_3$ and methylaluminoxane (MAO).[90] The sPSB samples with composition rich in styrene (> 60mol%) are crystalline for the presence of stereoregular syndiotactic polystyrene domain whereas butadiene is located as isolated units or forming polybutadiene rubber domains. The crystalline phase gives to the overall polymer characteristics typical of a semicrystalline polymer such as high chemical resistance; excellent physical properties; reversible physical crosslinking. The presence of the amorphous part is also very important since improve the *swelling* of the polymer, an important point for the diffusion of the reagents through the porous matrix. When the amount of styrene in the *co*-polymers is about 90% *w/w*, the average styrene block lengths are longer than nine units and sPSB exhibits polymorphism of the crystalline phases similar to that of the syndiotactic polystyrene (sPS)[86] comprising at least five different forms: α, β, γ, δ and ε.[91–93] The α and β forms are compact and the polymer chains assume a *trans*-planar conformation (**Figure 31**) whereas in the γ, δ and ε forms the chains assume a helix conformation (**Figure 31**).
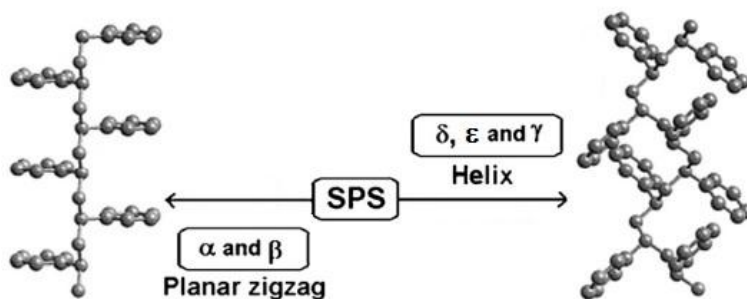
Figure 31: Chain conformations of the crystalline phases of sPS.

Noteworthy the δ and ε forms present nanometric cavities and channels, respectively, in the crystalline phase (**Figure 32**),[94,95] where guest small molecules (toluene, chloroform) are hosted producing co-crystalline and intercalate or clathrate structures. A clathrate structure is obtained when the small molecules are located and isolated inside the cavities, while an intercalate structure is obtained when layers of organic molecules occur alternatively to polymeric chain states.
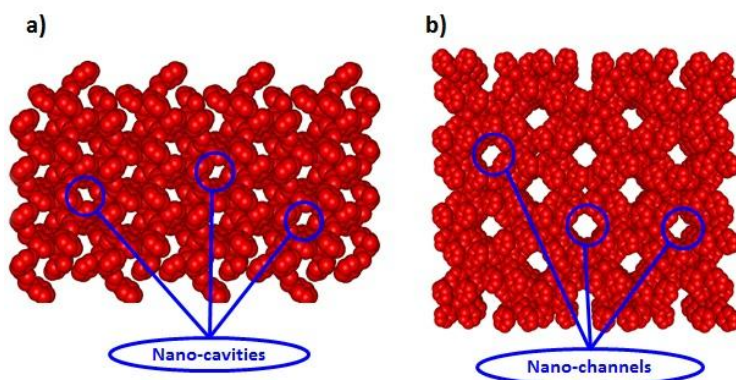
Figure 32: crystalline structure of a) δ form and b) ε form of sPS.

Generally, the *"as synthesized"* sPS is observed in the δ crystalline form containing molecules of the solvent (used in the synthetic process) as host molecule; these molecules are removed by heating, treatment with acetone or acetonitrile, or supercritical CO_2 extraction leaving empty cavities. The α and β forms are obtained from melt, by rapid or slow cooling respectively. In some conditions, the transition from one crystalline form to another can be achieved. For example, β and γ forms result from thermal treatment. The δ form is obtained at 110-130°C whereas the β form is obtained at 150°C. The α forms is obtained after annealing at 190°C of the γ form. Finally, the ε form can be obtained by swelling in $CHCl_3$ of the γ forms. In **Figure 33** a schematic representation of interconversion between the various polymorphic forms of sPS is reported.
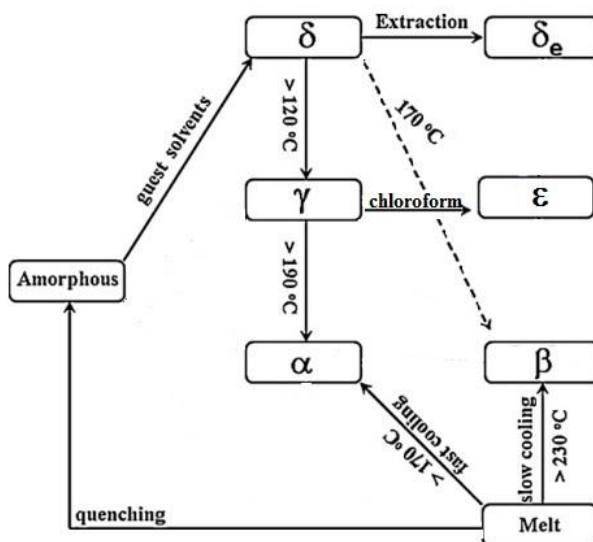
Figure 33: Scheme of interconversion between various polymorphic forms of sPS.

When sPSB is used as support for gold nanoparticles this complex polymorphous behavior can play an important role in the catalytic activity.

2.4.2: SYNTHESIS OF GOLD NANOPARTICLES EMBEDDED IN sPSB POLYMER

The synthesis of AuNPs-sPBS was reported for the first time in 2012.[86] The sPSB is dissolved in THF and the mixture is stirred for 24h at room temperature and then heated at reflux to improve the swelling of the polymer. After slow cooling to room temperature $HAuCl_4$ is added; the color of the slurry changes from transparent-white to yellow. The resulting slurry is stirred at room temperatures for 10 minutes and a sodium triethylborohydride solution in THF is rapidly added determining a color change from yellow to purple; the slurry is rapidly precipitated in methanol. The purple solid is filtrated, washed with fresh methanol to remove any by-product resulting from the reduction step and dried in vacuum at room temperature (**Figure 34**). The entrapment of gold as AuNPs in the polymer matrix is quantitative as assessed by atomic absorption spectroscopy (AAS) analysis of the filtrate and ICP analysis of the catalyst after digestion with aqua regia. Therefore, the amount of gold can be pre-fixed.
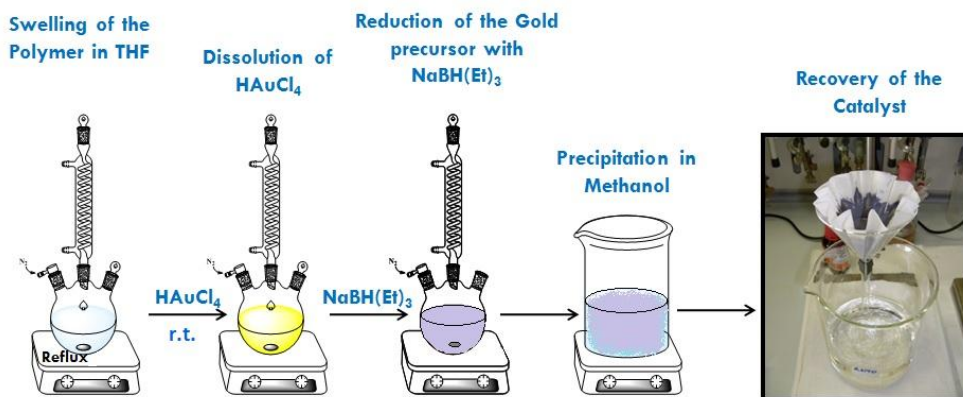
Figure 34: preparation of AuNPs-sPBS catalyst.

The stabilization of naked AuNPs in the polymeric support is due to the strong interaction with the aromatic moieties of polystyrene domains, in analogy with the results by Kobayashy.[83] In AuNPs-sPSB the crystallinity of the polymer matrix acts as physical and reversible crosslinks, hampering gold leaching. The as synthetized AuNPs-sPSB catalyst crystallizes in the clathrate δ form phase; it is thus possible to obtain the other crystalline forms through appropriate procedures.[87] The thermal treatment at 170°C for 5h produces AuNPs-sPSB in β crystalline phase, while thermal treatment at 135°C for 2h afford the formation of AuNPs-sPSB with γ crystalline phase. Finally, treating the AuNPs-sPSB in γ crystalline phase with a mixture of water and chloroform allows the formation of the ε crystalline phase.

2.5: CHARACTERIZATION OF GOLD NANOPARTICLES

The characterization of the size, shape, morphology and surface change of the AuNPs is carried out using different techniques such as UV-Vis, TEM, FT-IR, XRD, DLS, AFM and so on; the most common are discussed as follow.[96,97]

2.5.1: UV-VIS SPECTROSCOPY

UV-VIS spectroscopy is one of the most simple technique applied for the characterization of the size and concentration of the AuNPs in solution.[97] As discussed in paragraph 1.1, MNPs exhibit localized surface plasmon resonance (LSPR) that is the collective oscillation of the free electron gas located at the surface of nanoparticles (plasmon), in resonance with a specific wavelength of incident light.[3,4] The SPR of AuNPs results in a strong absorbance band in the visible region, typically at 520 nm, which can be measured by UV-Vis spectroscopy. Using the Lambert–Beer law (**Eq. 1**), (where A is the absorbance, b is the optical path length and C is the concentration of the solution), knowing the extinction coefficient ε, it is possible to calculate, through optical measurements, the concentration of spherical AuNPs in solution.

$$A = \varepsilon b C \qquad \text{Eq. 1}$$

Generally, the intensity of the SPR band depends on the size of the AuNPs and increases as their size increase (**a, Figure 35**).[98] Instead, the exact position of the SPR band depends on the shape and aggregation state of the AuNPs.[96] Usually for uneven shaped particles, compared to spherical particles of the same diameter, the absorbance peak shifts into the far-red region of the spectrum (**b**, **Figure 35**). Similarly, when formation of AuNPs aggregates occurs, shifts into the far-red region and broadening of the adsorption peaks occurs (**c, Figure 35**).[99]
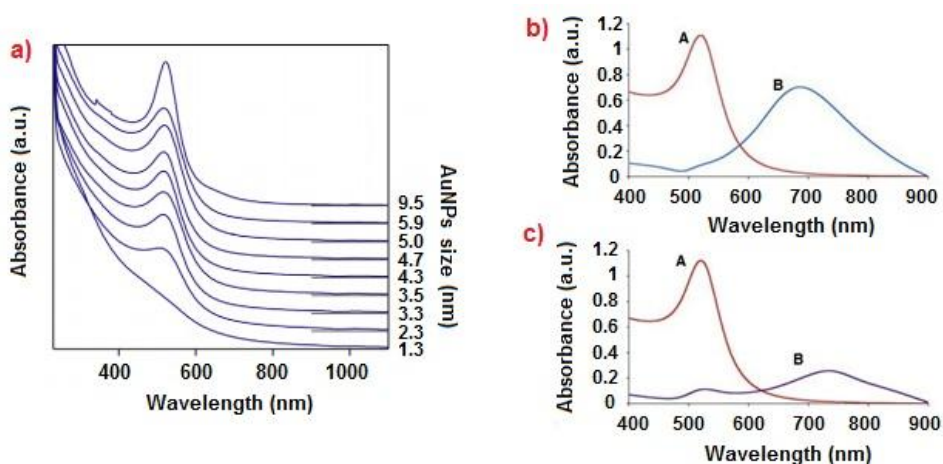
Figure 35: UV-Vis spectra showing a) AuNPs size dependent surface plasmon resonance; b) AuNPs shape dependent surface plasmon resonance as of spherical (A) and uneven-shaped (B) gold nanoparticles; c) AuNPs aggregation dependent surface plasmon resonance as of monodisperse (A) and agglomerated (B) gold nanoparticles.[99]

The average diameter of nanoparticles can be determined through UV-Vis spectroscopy. The extinction coefficient ε, from the Lambert–Beer law (**Eq. 1**), is used to build a calibration curve to estimate the average diameter of nanoparticles, according to **Eq. 2**,[100] where D is the core diameter of the nanoparticles and k and a are constants of the linear fitting.

$$ln\,\varepsilon = k\,lnD + a \qquad \text{Eq. 2}$$

Moreover for nanoparticles sizes below 35 nm the average diameter d of AuNPs can be also determined from the absorbance according to **Eq. 3**,[101] where A_{spr} is the absorbance at the surface plasma resonance peak, A_{450} is the absorbance at 450nm, while $B_1 = 3.55$ and $B_2 = 3.11$ are constants derived from theoretical model.[101]

$$d = e^{\left(B_1\frac{A_{spr}}{A_{450}} - B_2\right)} \qquad \text{Eq. 3}$$

2.5.2: X-RAY DIFFRACTION (XRD)

XRD technique is a non-destructive technique that provides information regarding the AuNPs crystalline structure,[96,97] the lattice parameters, crystalline grain size and nature of the phase, moreover can give information about the support. This technique exploits the wave nature of X-rays and their interaction with a crystalline sample and is based on Bragg's law (**Eq. 4**), where λ is the wavelength of the X-rays, n is the order

of diffraction, d is the spacing between sequential parallel planes of a crystal, and ϑ is complementary angle of the X-ray incidence.

$$n\lambda = 2dsin\emptyset$$

Eq. 4

In **Figure 36** a typical XRD pattern of AuNPs is showed.[102] Four Bragg's reflection can be observed at around 38.2°, 44.5°, 64.9° and 74.9° in the diffraction pattern, corresponding respectively to (111), (200), (220) and (311) planes of *fcc* lattice (according to Joint Committee on Powder Diffraction Standards-JCPDS no. 04-0784). The peak corresponding to (111) plane is more intense than the others suggesting that (111) is the predominant orientation.
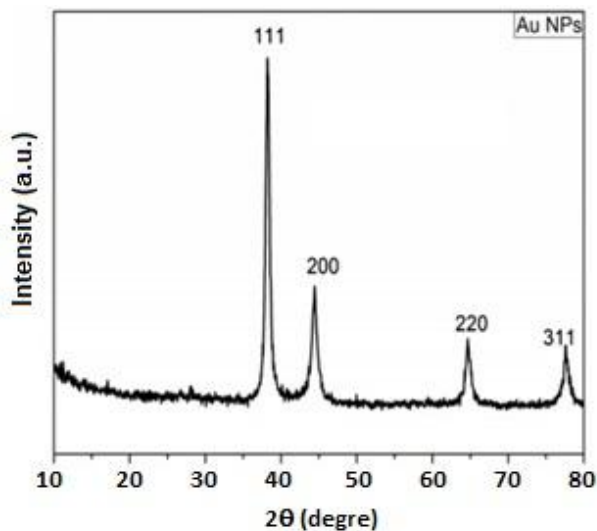
Figure 36: XRD pattern of gold nanoparticles.[102]

The size of gold crystallites can be calculated from the Scherrer equation (**Eq. 5**),[103] considering the Full Width at Half Maximum (FWHM) of the most intense peak ((111) plane) in the diffraction pattern.

$$B = \frac{K\lambda}{L cos\varnothing}$$

B = peak width; L = crystallite size; ϑ = diffraction angle; λ = X-ray wavelength; K =constant that is function of the crystallite shape (generally taken as 1.0 for spherical particles).

In most of the cases the so obtained values of crystallite size are in agreement with those obtained by TEM, but, this procedure cannot be applied if the metal loading is < 0.5wt% and the size is < 2nm, due to the low intensity of diffraction peaks.

2.5.3: X-RAY PHOTOELECTRON SPECTROSCOPY (XPS)

XPS is the most widely used technique for surface chemical analysis allowing to elucidate the electronic structure, elemental composition and oxidation states of the elements lying on the surface of the sample. The photoelectric effect is a physical phenomenon resulting from the radiation-matter interaction and is characterized by the emission of electrons from a surface, usually of a metal, when this is hit by electromagnetic radiation (*i.e.* photons) having a certain wavelength. The kinetic energy of the emitted photoelectron (E_K) is related to the energy

of the exciting radiation hv and the binding energy of the electron in the atom (E_B) described by Einstein's equation (**Eq. 6**), where φ is the work function of the sample.

$$E_B = hv - E_K - \varphi$$

<div align="right">**Eq. 6**</div>

In the case of core-shell MNPs, a major issue is the interpretation of data that requires knowledge about the chemical core and the size of the particles. In particular, the essential problem is the conversion of the relative XPS intensities, usually expressed as a ratio of the intensity of photoelectrons from the shell to the intensity of photoelectrons from the core, into the shell thicknesses of the MNPs. Shard published an accurate empirical method to convert the XPS intensities into shell thicknesses of spherical core-shell MNPs.[104]

There is an interesting work in the literature where XPS is used to detect the oxidation state of gold in different AuNPs catalysts synthesized by DP method.[105] In **Figure 37** is shown the best fitting of the XPS curves for the Au-CeO$_2$, Au-TiO$_2$ and Au-SiO$_2$ catalysts, highlighting the different contribution of the gold species onto the surface at variance of the support. The Au-CeO$_2$ catalyst shows two photoelectron peaks at binding energy BE of 84.5 and 85.8 eV; the band at about 84 eV is typically attribute to Au(0) while the peak around 85 eV is assigned to Au(I) species.[106] From the intensity of the peaks one can envisage that the most abundant species are Au(0) with a small fraction of oxidized Au(I) species. The same oxidation states of gold are detected on the surface of the Au-

TiO$_2$ catalyst (BE = 84.4 and 85.6 eV) where a greater amount of Au(I) species are present. The spectrum of Au-SiO$_2$ catalyst show photoelectron peaks at BE of 84.4 and 86.5 eV, typical of Au(0) and Au(III) species,[106] where the major fraction is the latter.
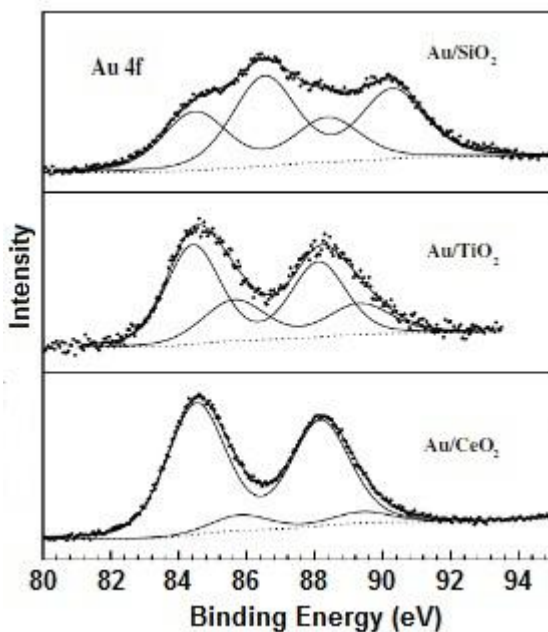
Figure 37: XPS curve fitting of Au photoelectron peak in Au-CeO$_2$, Au-TiO$_2$ and Au-SiO$_2$ catalysts. The scattered points are referred to the experimental data while the solid line to the best fitting curve.[105]

2.5.4: TRASMISSION AND SCANNING ELECTRON MICROSCOPY (TEM AND SEM)

TEM and SEM are microscopic techniques used for the resolution imaging[107] and can provide information about both AuNPs (like size and shape of NPs) and support (like presence of porosity, size of the pores). These techniques exploit the interaction between a uniform current density electron beam and a sample, under vacuum condition. When the electron beam reaches the sample, a part of these electrons is transmitted, while, another part is elastically or inelastically scattered. The magnitude of the interaction depends on several factors, such as size, sample density and elemental composition. In TEM analysis, the final image is built with the information acquired from the transmitted electrons and the electron energies of the electron beam are usually within a range of 80 to 300 keV to enable the electrons to pass through the material. TEM is commonly used to analyze nanoparticle size and shape, since it provides not only direct images of the sample but also the most accurate estimation of the nanoparticle homogeneity. Some limitations are: difficulty in quantifying a large number of particles or misleading images due to orientation effects.[97]

SEM technique is designed primarily to examine material surfaces and for this reason, the electron energy of the electron beam is much lower than TEM, typically 1-30 keV. The images are produced by scanning the sample with a beam of electrons. As the electrons interact with the sample, they produce secondary electrons, back-scattered electrons and characteristic

71

X-rays.[107] These signals are collected to form images with a typical resolution between 1-20 nm. Although SEM technique cannot see features to the level of detail as a TEM; however it is much faster, less restrictive and can sometimes be performed with limited or no sample preparation.

2.5.5: DYNAMIC LIGHT SCATTERING (DLS)

DLS technique is widely used for the determination of the size and size distribution of AuNPs, but can also be employed for the evaluation of shape, aggregation state and even to evaluate surface modifications.[96,97] It is performed for particles in colloidal suspension and for this reason the hydrodynamic size of particles is measured, which includes the physical size of the nanoparticle core, the surface coating and solvent layer associated with the particle. When a laser beam illuminates a suspension, the particles scatter the light but because of the Brownian motions acting on them, the scattering intensity fluctuates over time. Analysis of this intensity fluctuations yields information on diffusion processes and thus particle size can be calculated using Stokes-Einstein equation (**Eq. 7**), where d_H is the hydrodynamic diameter of the particle, k is the Boltzmann's constant, T is the absolute temperature, η is the viscosity of the solution and D is the diffusion coefficient of the particles in the solution.

$$d_H = {kT}/{3\pi D\eta} \qquad \text{Eq. 7}$$

A limitation of DLS is that large particles scatter much more light and even a small number of large particles can obscure the contribution from smaller particles. DLS can be used also to study the aggregation of AuNPs. Goon et al.[108] studied the aggregation stability of AuNPs supported on Fe_2O_3 (AuNPs-F_2O_3) and AuNPs-F_2O_3 functionalized with polyethyleneimine (PEI). These particles were subjected to sonication and the hydrodynamic diameters were measured up to 1h of irradiation time. **Figure 38** shows that AuNPs-Fe_2O_3 start aggregating immediately after sonication, while PEI-coated particles are significantly more stable against aggregation, with DLS hydrodynamic diameters constant at about 200 nm.
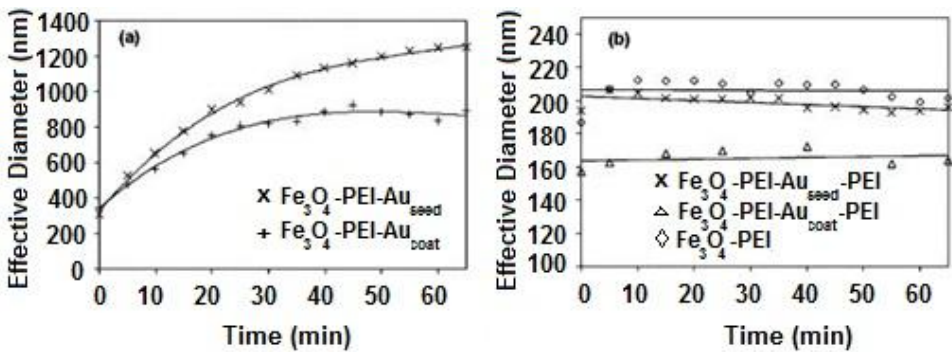
Figure 38: DLS measurements on (a) particles without PEI; (b) particles with PEI functionalization.[108]

2.6: AIM OF THE PROJECT

The development of new methodologies in organic synthesis that allow to minimize the environmental concerns and reduce production costs, energy consumption and toxic waste production is becoming of increasing interest in sustainable catalysis: in this context, the use of heterogeneous catalysts is relevant and desirable. Compared to homogeneous catalysts, actually the heterogeneous catalysts offer several advantages such as easy recovery and reuse and elimination of metal contaminants from the final product. In particular, heterogeneous gold catalysts consisting of AuNPs supported on conventional metal oxides and polymer matrices, are of increasing interest for their biocompatibility, high activity and selectivity in a wide range of organic reactions, which can be carried out under very mild conditions; examples include the pioneering examples of CO oxidation to CO_2, selective aerobic oxidation of alcohols, selective reduction of unsaturated alcohols and nitroarenes.

In this context, the AuNPs-sPSB resulted very promising in organic reactions of aromatic compounds due to high affinity and permeability of these compounds into the nanoporous and nanochannels of the δ and ε crystalline forms of the crystalline polymer support. Excellent results were actually obtained in the selective aerobic oxidation of alcohols, nitrobenzene reduction and aerobic oxidative esterification of cinnamyl alcohol. The polymeric support, under the different crystalline phases, directly affect the activity and selectivity of the reactions.

In this research project, we tested the AuNPs-sPSB catalyst in intermolecular hydroamination of phenylacetylenes with anilines to produce a wide range of arylketimines, a commodity of interest as organic synthetic intermediates and for pharmaceutical applications. The reaction mechanism has been thoroughly investigated using kinetic studies, supported by DFT calculations, to gain insight in the structure of the reaction intermediates and to assess the rate determining step of the complex reaction mechanism. We also tested the AuNPs-sPSB catalyst in the selective oxidation and oxidative esterification of 2,5-hydroxymethylfurfural HMF, a platform molecule in Green Chemistry, to produce the corresponding oxidation and esterification products as desirable research targets.

Finally, aiming to investigate the suitability of heterogeneous gold catalysts in cascade reactions, the photoactive commercial AuNPs-TiO$_2$ catalyst has been tested in intramolecular hydroamination/asymmetric transfer hydrogenation of 2-(2-propynyl)anilines to obtain chiral tetrahydroquinolines. The performance of this catalyst has been then compared to that of the homogenous Au(I) catalyst already applied in this process.

CHAPTER 3

....

INTERMOLECOLAR HYDROAMINATION REACTION CATALYZED BY AuNPs-sPBS

CHAPTER 3: INTERMOLECOLAR HYDROAMINATION REACTION CATALYZED BY AuNPs-sPBS

3.1: HYDROAMINATION REACTION

The hydroamination reaction of alkenes and alkynes is a convenient synthetic route because it is one of the most cost-effective processes, with high efficiency and sustainability due to the 100% atom-economy of the reaction. Hydroamination is a versatile reaction that allows the direct formation of a new carbon-nitrogen bond by the addition of amines to an unsaturated carbon-carbon bond.[109] While hydroamination reactions of alkenes lead directly to stable amines, alkynes are converted into reactive species such as enamines and imines (**Figure 39**), which can undergo to further transformations. This makes this process of particular interest as it allows a useful way to obtain important building blocks for the chemical and pharmaceutical industry. Intermolecular or intramolecular version of this reaction can be performed allowing, in the second case, the obtainment of heterocyclic compounds.
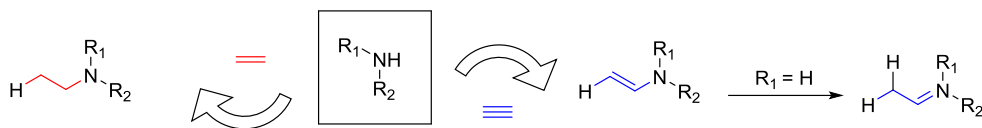
Figure 39: hydroamination reaction of alkynes and alkenes.

Hydroamination reaction of unsymmetrically substituted alkenes or alkynes is complicated by the formation of two isomeric products, the Markovnikov and anti-Markovnikov product (**Figure 40**) and it is important to control the selectivity of the process.[110]
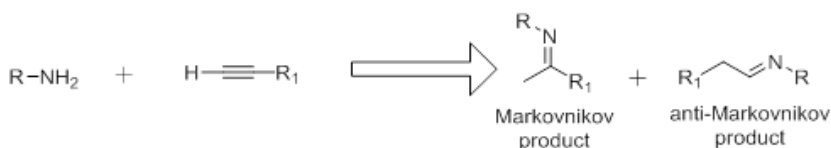
Figure 40: Markovnikov and anti-Markovnikov products obtained from hydroamination reaction of unsymmetrically substituted alkyne.

Moreover, thermodynamic and kinetic aspects of the reaction must be taken into consideration. The thermodynamic data for the addition of a simple amine, such as ethylamine or ammonia, to ethylene are shown in **Figure 41**. This reaction is almost thermoneutral and thus an equilibrium state between the reactants and products can be anticipated; the increase of temperature, shifts the reaction toward the reagents because of the negative reaction entropy $\Delta S°$.[111] The addition of ammonia to acetylene is estimated to be approximately 60-70 kJ mol^{-1} more exothermic than ethylene,[112] so the hydroamination reactions of alkynes are generally more easy to be performed.

High activation barriers are observed in the addition of amines across carbon–carbon multiple bonds because of electrostatic repulsion between electron rich π system of the alkyne or alkene and the electron lone pair of the nitrogen atom. In conclusion, an efficient catalyst is required to promote the hydroamination reaction at temperatures as low as possible.
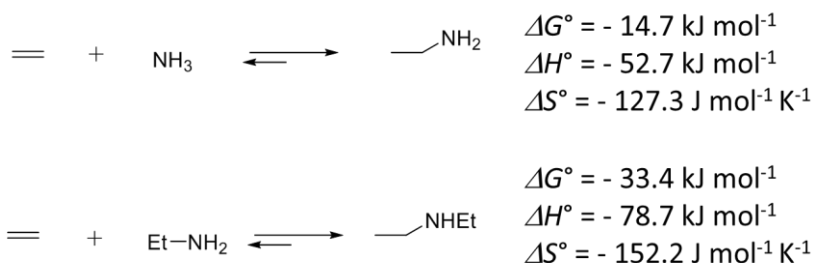
Figure 41: thermodynamic data for the addition of ethylamine or ammonia to ethylene.

Different catalytic approaches have been developed, in particular with alkynes. The use of homogenous rare-earth metal complexes, group 4 metal complexes or late transition metal complexes is widely explored, as well as base or acid catalyzed processes.[110,111,113,114] Much less investigated is the use of heterogeneous catalysts. Examples of inorganic solid catalysts like zeolites or clays have been reported:[113] in these cases, the catalytic activity depends on the amount and strength of Brønsted

acid sites in the solid catalysts. In addition, metal-ion exchanged zeolites and clays or supported complexes on oxide surfaces have also been used.[113] In the first case, the strong Lewis acidity of the metal cation yields stable catalyst-substrate adduct and efficiently catalyzes the reaction. In the second case, the pK_a of the support and the basicity of the ligand have to be considered of fundamental interest since hydroamination activity decreases with the increase of these factors. Supported MNPs are known to catalyze hydroamination reaction; in particular, AuNPs have been preliminary tested in hydroamination of alkynes as described in the following paragraph.

It is noteworthy that irradiation with microwaves (in presence of homogeneous metal catalysts or in metal free conditions) resulted in an acceleration of the hydroamination reaction and a drastic reduction of the reaction times.[115,116]

3.2: HYDROAMINATION REACTION OF ALKYNES CATALYZED BY SUPPORTED AuNPs

Hydroamination of phenylacetylene (PA) with aniline (AN) has been used as a benchmark reaction to assess the activity and selectivity of supported AuNPs (**Figure 42**). Generally, high temperature and/or long time of reaction are required to convert the reagents into the desiderate imines,

with high yields and selectivity; the turnover frequency (TOF) or turnover number (TON) are thus quite low.
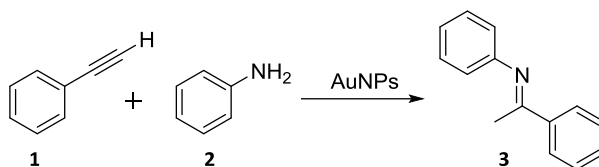
Figure 42: hydroamination reaction of aniline and phenylacetylene catalyzed by AuNPs.

Different supports have been investigated, in particular those based on metal oxides. Zhu *et al.* reported a photocatalytic hydroamination of PA using AuNPs on nitrogen doped TiO_2 as catalyst.[117] The reaction in this case is promoted by visible light at 40°C using toluene as solvent; the imine **3** was obtained with 98% selectivity (conversion 79%) in 25h. This catalyst was also tested with PA or AN derivatives; amines with electron withdrawing groups (EWGs) at the aromatic ring yielded higher conversion than those with electron donating groups (EDGs). The addition of phosphotungstic acid ($H_3PO_4 \cdot 12WO_3$) as acid promoters to the AuNPs-TiO_2 catalyst increased the yield of the imine **3** (86% yield in 7h) at 80°C in neat conditions with 0.2 *mol%* Au loading.[118] Also in this case EDGs and EWGs substituents at AN and PA are well tolerated, but ANs with sterically bulky substituents required higher catalyst loading and longer

reaction times; aliphatic alkynes needed harsher conditions to achieve good yields.

More recently, Boanini reported the AuNPs-SiO$_2$ catalyst modified with a propynylcarbamate organic functionality (**Figure 43**):[119] the best results in terms of conversion (91%) and selectivity (90%) were observed in solvent-free conditions at 110 °C for 24 h, with a catalyst loading of 1 *mol%* Au.
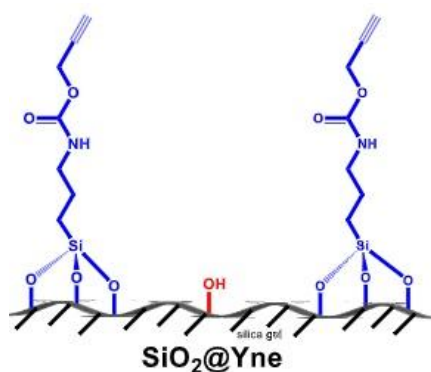
Figure 43: SiO$_2$ modified support used by Boanini *et al.*[117]

The first example of hydroamination reaction catalyzed by AuNPs supported on polymer was reported by Corma.[120] AuNPs-chitosan-SiO$_2$ hybrids were used as catalyst and in presence of air. The screening conditions were performed using the reaction of AN with the most challenging substrate 1-octyne; the catalyst displayed similar reactivity also with PA, where almost complete conversion (89%) was achieved in

22 h in toluene (1.25 *mol%* Au loading). The product **3** was produced with a selectivity of only 78%, probably due to the presence of water in the reaction system that leads to hydrolysis of the imine to the ketone.

3.3: MECHANICISTIC HYPOTHESIS ON HYDROAMINATION REACTION OF ALKYNES CATALYZED BY AuNPs

Different studies for hydroamination reaction of alkynes catalyzed by homogenous Au(I) catalyst are reported in the literature.[110,121] The general mechanistic pathway follows the route of carbon-carbon multiple bond activation of the alkyne by π-coordination to the Au-center, followed by the nucleophilic attack of the amine.

Two possible mechanisms are reported, namely the inner sphere and outer sphere mechanism.[122,123] In the inner sphere mechanism a coordination of the aniline to [Au] occurs prior of the carbon–nitrogen bond formation, leading to the enamine product from the *syn*-addition (**a**, **Figure 44**). In the outer sphere mechanism, a direct nucleophilic attack of the amine to the coordinated alkyne occurs, leading to the enamine product of *anti*-addition (**b**, **Figure 44**). As final step, the enamine product can undergo a tautomeric rearrangement to give the imine product.

The mechanism for hydroamination reaction of alkynes catalyzed by AuNPs catalysts is not yet understood and only very few hypotheses have been reported in the literature.[124,125] One possibility is that the

mechanism proposed for the homogenous Au(I) catalysts, comprising the activation/coordination of the alkyne followed by the internal/external nucleophilic attack of the amine, works in the similar manner in heterogeneous gold catalysts.
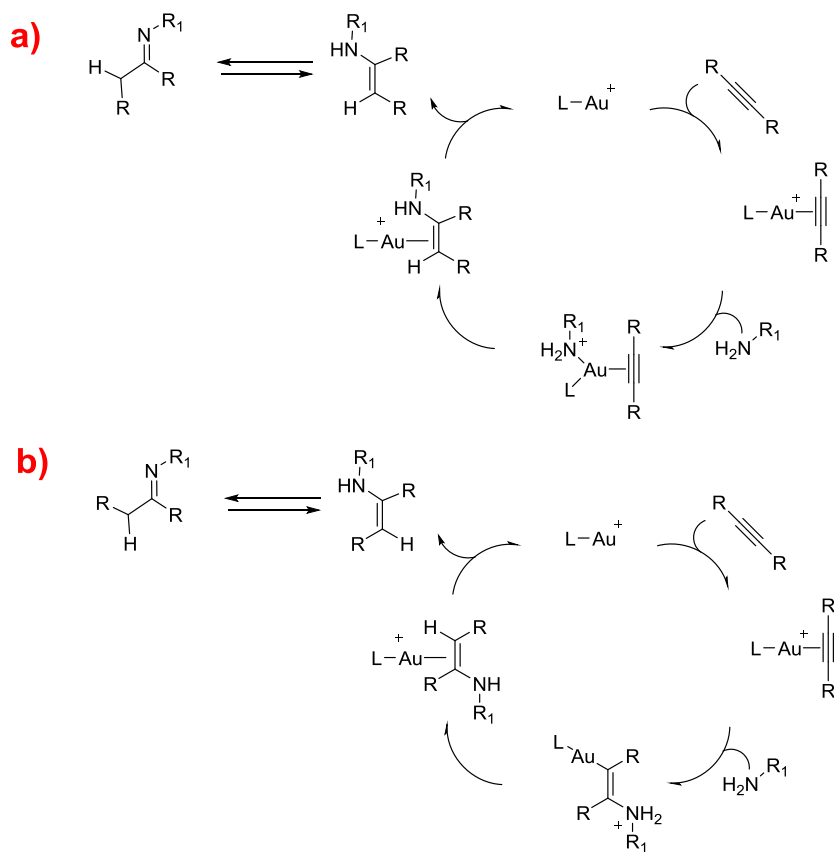
Figure 44: proposed mechanistic pathways for hydroamination reaction catalyzed by homogenous Au(I) catalysts: a) inner sphere mechanism, b) outer sphere mechanism.

A different reaction pathway, supported by a computational approach, has been proposed by Bordoloi *et al.*[124] The activation of AN over the Au(0) surface leads to an amido-Au complex, followed by the coordination of the alkyne to the Au-surface. Then the nucleophilic attack of the N atom to the carbon-carbon multiple bond leads to the enamine formation; finally, the enamine tautomerizes to give the Markovnikov product (**Figure 45**). However, the energetic barriers and the reaction intermediates are located at energy values too high, appearing in contrast with the experimental data.
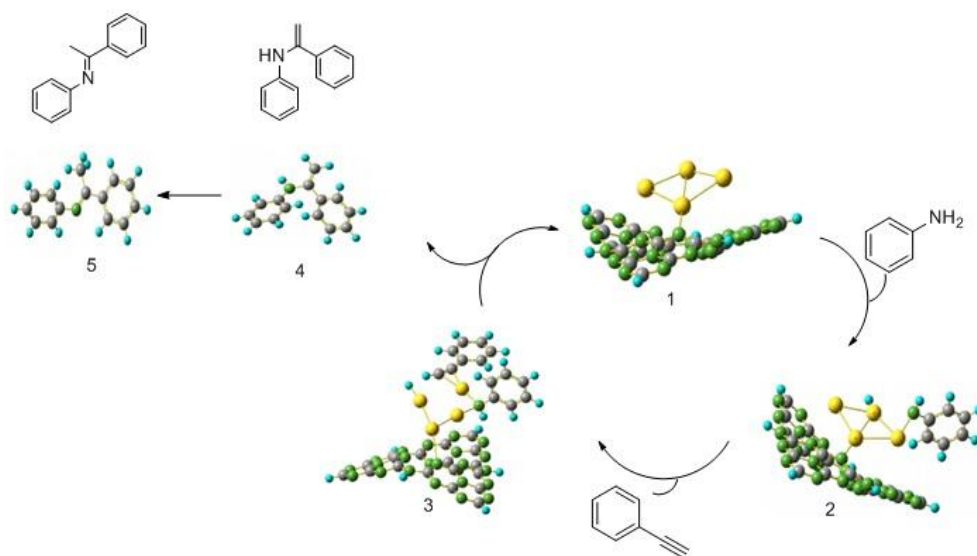
Figure 45: mechanistic pathway for hydroamination of FA and AN catalyzed by heterogeneous Au(0) catalyst.

3.4: HYDROAMINATION REACTION CATALYZED BY AuNPs-sPSB: CATALYST PREPARATION AND CHARACTERIZATION.

sPSB polymer with styrene content of 88 *mol%* (93 *wt%*) has been used as AuNPs support in order to preserve polymer crystallinity and impart good swelling properties in THF. The AuNPs-sPSB catalyst was synthesized in the δ and β crystalline phases and 2 *wt%* of Au, as previously described, and used without further treatment. The catalyst was characterized by wide angle x-rays diffraction (WAXD) analysis, TEM images before the use and XPS analysis.

The WAXD patterns of the sPSB support, AuNPs-sPSB catalyst in δ crystalline phase and β crystalline phase are reported in **Figure 46**. Diagnostic 2Θ signals are shown for the δ form of sPSB containing toluene molecules coming from the synthetic process (**a**, **Figure 46**); the same pattern is observed for the AuNPs-sPSB (**b**, **Figure 46**) in δ form where THF molecules replace the toluene molecules in the crystalline lattice. The average size of the AuNPs, determined by the Scherrer equation[103] applied to the <111> reflections of crystalline gold in *fcc* is of 5.3 nm. The annealing of the catalyst at 170 °C for 5h, removes the clathrated molecules and converts the polymeric support to the β crystalline form (**c**, **Figure 46**), leading to a partial coalescence of the AuNPs with an increase of the average size to 9.0 nm.

The XPS analysis of AuNPs-(δ)sPSB (**Figure 47**) shows that the gold precursor is completely reduced to Au(0) during the catalyst synthesis.

 The conventional and high resolution transmission electron microscopy (CTEM and HRTEM, respectively) images are reported in **Figure 48**. In general, the AuNPs are homogeneously dispersed in the polymer matrix before and after the thermal treatment (panels **a** and **d**, **Figure 48**). The HRTEM of AuNPs-(δ)sPSB shows the formation of only a few aggregates (**b**, **Figure 48**) and the presence of AuNPs with irregular cuboctahedral morphology (**c**, **Figure 48**). After the annealing, both twinned and single AuNPs with a spheroidal-like morphology are detected (panels **e** and **f**, **Figure 48**).
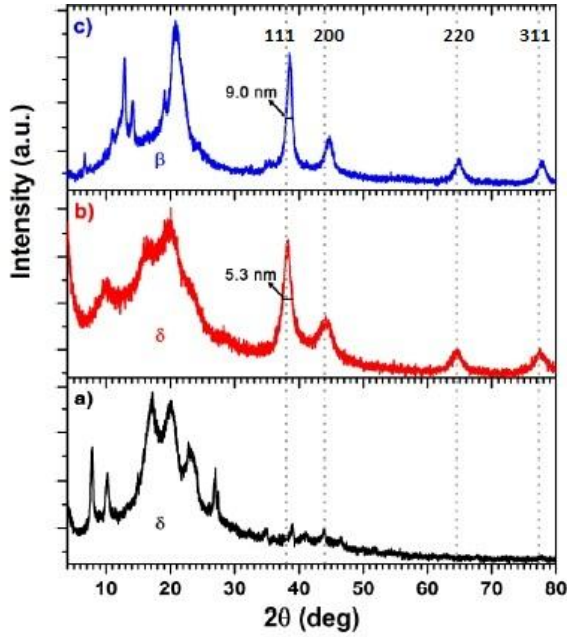
Figure 46: WAXD patterns of a) sPSB matrix, b) AuNPs-(δ)sPSB, c) AuNPs-(β)sPSB. Greek letters indicate the crystalline form of sPSB. Dotted lines mark the reflections of *fcc* crystalline lattice planes of nanocrystalline gold.
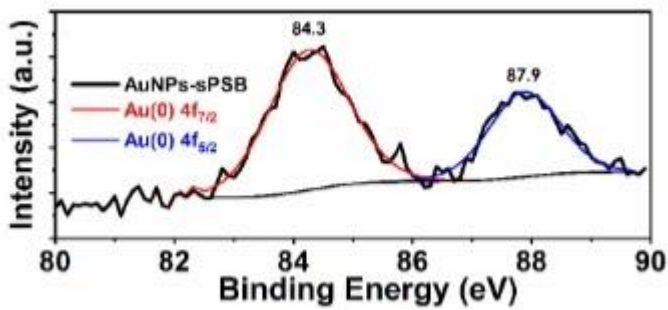
Figure 47: XPS profile of AuNPs(δ)-sPSB with Au(0) 4f$_{7/2}$ and 4f$_{5/2}$ predicted traces.
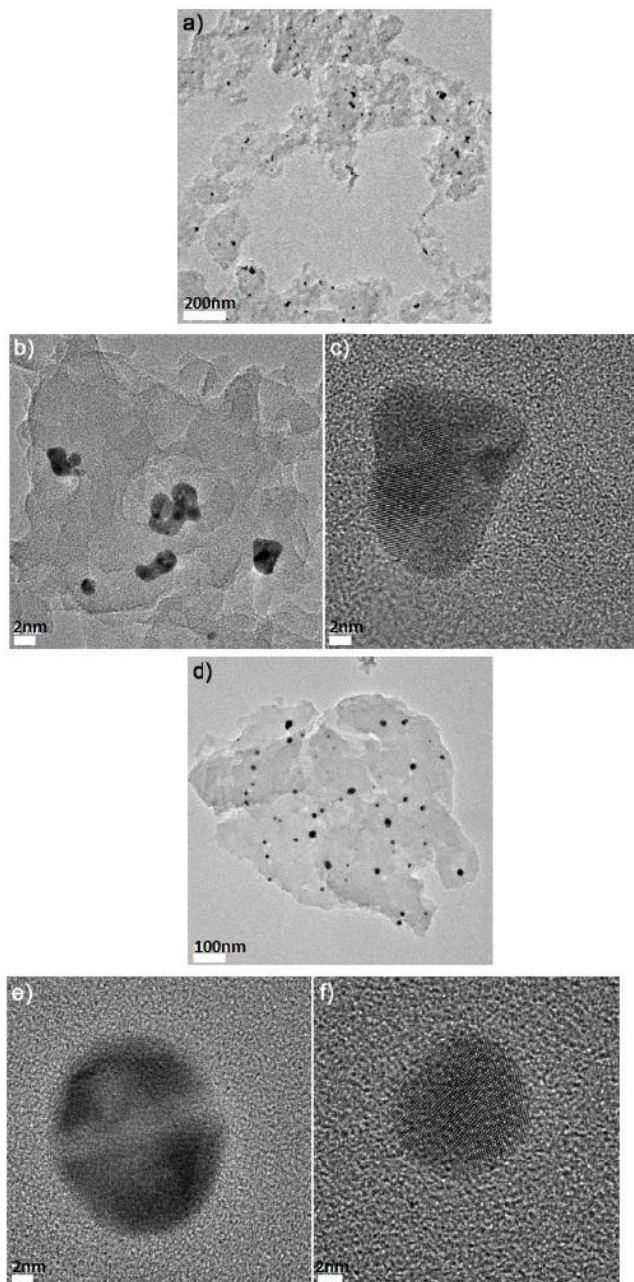
Figure 48: CTEM (panels a, d) and HRTEM (panels b, c, e, f) images of AuNPs-(δ)sPSB (panels a-c), and AuNPs-(β)sPSB (panels d-f).

3.4.1: HYDROAMINATION REACTION CATALYZED BY AuNPs-sPSB: CATALYTIC TESTS.

Hydroamination of PA with AN was studied to gain information about the activity and selectivity of the AuNPs-sPSB catalyst and to investigate the role of the polymeric matrix on the reaction mechanism. The hydroamination reaction was initially studied under inert atmosphere and neat condition, at 100°C, using 0.2*mol%*Au loading (molar ratio Au:PA = 1:500) and AN:PA molar ratio of 1.2. The use of inert and dry conditions is essential to prevent hydrolysis of imine to form acetophenone.

The use of AuNPs-sPSB in β crystalline phase (AuNPs-(β)sPSB) allows to obtain the Markovnikov imine **3** as the only product with almost complete conversion of PA in 7 h (entry **1**, **Table 1**); the *E/Z* selectivity of the product was always found to be >99% for the *E* configuration. The catalytic properties of AuNPs-(β)sPSB were compared with those of commercial gold catalysts, namely AuNPs-TiO$_2$, AuNPs-Al$_2$O$_3$, AuNPs-ZnO and AuNPs-CB under the same condition of entry **1**, **Table 1**. All the catalysts produced the imine derivative, with Markovnikov regiochemistry and *E* configuration with high selectivity (entries **1**, **4-7**, **Table 1**). The conversions observed with the AuNPs-Al$_2$O$_3$ and AuNPs-ZnO catalysts are rather low, 65% and 28% respectively (entries **5** and **6**, **Table 1**), while with AuNPs-CB is rather high (81%) (entry **7**, **Table 1**).

Table 1: hydroamination reaction of FA and AN catalyzed by AuNPs.
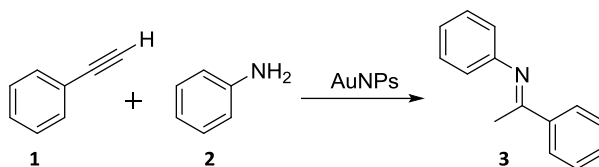
Entry[a]	Catalyst	t (h)	Conv.[b,c] (mol%)	TON[c,d]	TOF[c,e] (h⁻¹)
1	AuNPs-(β)sPSB	7	90	453	65
2	AuNPs-(β)sPSB	1	45	225	225
3	AuNPs-(β)sPSB	3	60	301	100
4	AuNPs-TiO₂	7	90	453	65
5	AuNPs-Al₂O₃	7	65	325	46
6	AuNPs-ZnO	7	28	140	20
7	AuNPs-CB	7	81	405	58

[a] Reaction conditions: PA (5.08 mmol), AN (6.09 mmol; molar ratio AN:PA = 1.2), catalyst (100 mg, molar ratio Au:PA = 1:500), 100°C. [b] Conversion of phenylacetylene. [c] Determined by ^{1}H-NMR analysis of reaction mixture (DMSO-d_6, 25 °C). [d] Turnover number (mol$_{product}$/mol$_{Au}$). [e] Overall turnover frequency (TON/reaction time).

However, AuNPs-(β)sPSB showed the best catalytic activity with a TOF value of 65h^{-1}. Surprisingly AuNPs-TiO₂ a showed catalytic activity similar to that of AuNPs-(β)sPSB, without the addition of acidic promoters (compare entries **1** and **4** of **Table 1**) or the use of UV irradiation as previously proposed in the literature.[117,118,125]

3.4.2: INFLUENCE OF THE TEMPERATURE: CONVENTIONAL HEATING AND IRRADIATION WITH MICROWAVES

The hydroamination of PA and AN was screened at different temperatures in 1 h to keep the conversions low.

Table 2: influence of the temperature on the hydroamination reaction catalyzed by AuNPs-(β)sPSB.

Entry[a]	T (°C)	Conv.[b,c] (mol%)	TON[c,d]	TOF[c,e] (h-1)
1	60	5	25	25
2	80	23	115	115
3	100	45	225	225
4	120	64	320	320

[a] Reaction conditions: PA (5.08 mmol), AN (6.09 mmol; molar ratio AN:PA = 1.2), AuNPs-(β)sPSB catalyst (100 mg, molar ratio Au:PA = 1:500), 1h. [b] Conversion of phenylacetylene. [c] Determined by ^{1}H-NMR analysis of reaction mixture (DMSO-d_6, 25 °C). [d] Turnover number (mol$_{product}$/mol$_{Au}$). [e] Overall turnover frequency (TON/reaction time).

As expected, the temperature strongly affects the reaction rate. Only traces of imine **3** were obtained at 65°C (entry **1**, **Table 2**). By increasing the temperature, an increase of the conversion was observed; at 100°C

and 120°C (entries **3**-**4**, **Table 2**) very high catalytic activities were achieved with a TOF values of 225 and 320 h^{-1} respectively. This is a remarkable result, in particular considering that the organic polymeric support is not crosslinked and is stable at high temperature without leading to gold leaching.
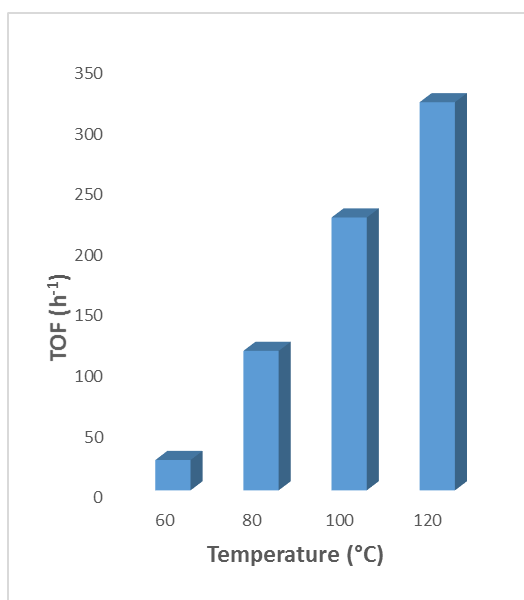
Figure 49: Effect of temperature on hydroamination reaction promoted by AuNPs-(β)sPSB: TOF as a function of temperature.

The **Figure 49** shows the trend of the TOF values for the AuNPs-(β)sPSB in the range of temperature 60-120 °C; the latter value is among the highest so far reported for heterogeneous gold catalysts.[117–120,124–131]

The use of non conventional heating by irradiation with microwaves (in combination with homogenous catalysts) is known to accelerate the hydroamination process.[113,115] In this context an attempt to promote the intermolecular hydroamination reaction, between AN and PA, using microwaves with AuNPs-(β)sPSB was made.

Table 3: influence of the microwaves on the hydroamination reaction catalyzed by AuNPs-(β)sPSB.

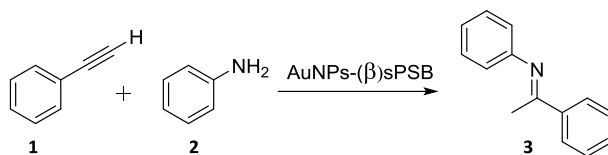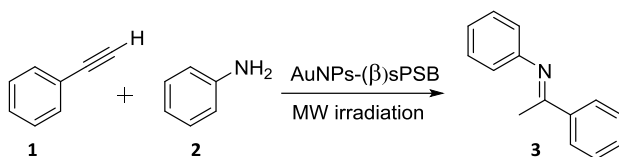| Entry[a]	t (h)	Conv.[b,c] (mol%)	TON[c,d]	TOF[c,e] (h^{-1})
1	1	41	206	206
2	3	66	332	110
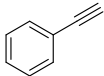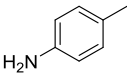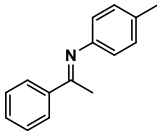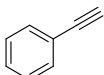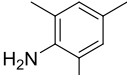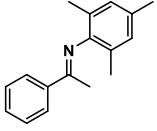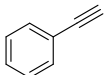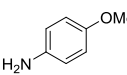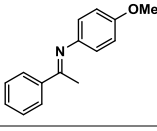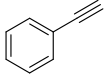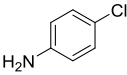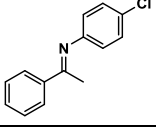
[a] Reaction conditions: PA (5.08 mmol), AN (6.09 mmol; molar ratio AN:PA = 1.2), AuNPs-(β)sPSB catalyst (100 mg, molar ratio Au:PA = 1:500), 100°C under microwaves irradiation. [b] Conversion of phenylacetylene. [c] Determined by ^{1}H-NMR analysis of reaction mixture (DMSO-d_6, 25 °C). [d] Turnover number (mol$_{product}$/mol$_{Au}$). [e] Overall turnover frequency (TON/reaction time).

The reactions were carried out in the conditions of entry **2** and **3** of **Table 1**. In these cases, the microwave irradiation did not produce modification of the conversion and selectivity values of the hydroamination reaction (**Table 3**).

3.4.3: HYDROAMINATION OF SUBSTITUTED PHENYLACETYLENES AND ANILINES.

The coupling of PA with ANs carrying different EWG and EDG onto the aromatic rings has been investigated at 100°C with a gold loading of 0.2*mol*% (molar ratio Au:PA = 1:500) (**Table 4**).
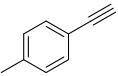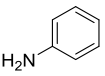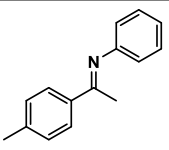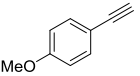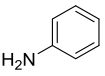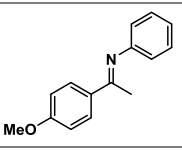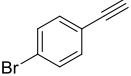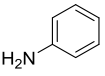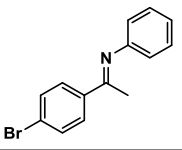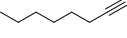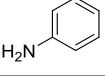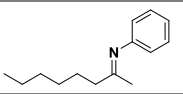
Table 4: Hydroamination reaction of PA with amines promoted by AuNPs-(β)sPSB.

Entry [a]	Alkyne	Aniline	Product[b]	Conv.[b,c] (mol%)	E/Z[b] (molar ratio)	TON [c,d]	TOF [c,e] (h^{-1})
1				78	>99:1	392	56
2				91	>99:1	458	65
3				94	>99:1	473	68
4				96	>99:1	483	69

[a] Reaction conditions: PA (5.08 mmol), AN (6.09 mmol; molar ratio AN:PA = 1.2), AuNPs-(β)sPSB catalyst (100 mg, molar ratio Au:PA = 1:500), 100°C, 7h. [b] Conversion of phenylacetylene. [c] Determined by ^{1}H-NMR analysis of reaction mixture (DMSO-d_6, 25 °C). [d] Turnover number (mol$_{product}$/mol$_{Au}$). [e] Overall turnover frequency (TON/reaction time).

In all the investigated cases, the yields are excellent and the selectivity are high in favor of the Markovnikov products, showing the thermodynamic favored *E* configuration. The introduction of EWGs group onto the aromatic group of ANs produces a limited effect,[132] being the activity values always high, with TOF values ranging from 56 h^{-1} to 69 h^{-1}.

Table 5: Hydroamination reaction of AN with alkynes promoted by AuNPs-(β)sPSB.

Entry [a]	Alkyne	Aniline	Product[b]	Conv.[b,c] (mol%)	E/Z[b] (molar ratio)	TON [c,d]	TOF [c,e] (h^{-1})
1				66	>99:1	327	47
2				89	>99:1	444	64
3				80	>99:1	402	57
4[f]				75	25:75	148	21

[a] Reaction conditions: PA (5.08 mmol), AN (6.09 mmol; molar ratio AN:PA = 1.2), AuNPs-(β)sPSB catalyst (100 mg, molar ratio Au:PA = 1:500), 100°C, 7h. [b] Conversion of phenylacetylene. [c] Determined by ^{1}H-NMR analysis of reaction mixture (DMSO-d_6, 25 °C). [d] Turnover number (mol$_{product}$/mol$_{Au}$). [e] Overall turnover frequency (TON/reaction time). [f] AuNPs-(β)sPSB catalyst (0.5*mol*%Au molar ratio Au:1-octyne = 1:200).

The results for the reaction of AN with different aromatic PAs are reported in **Table 5**. The effect of the EWGs onto the PAs seems to be more pronounced (entries **1**-**3**, **Table 5**) determining an increase of the TOF values from 47 h^{-1} of the methyl para-substituent (entry **1**, **Table 5**) to 64 h^{-1} for the methoxy para-substituent (entry **2**, **Table 5**). The reaction of AN with 1-octyne (entry **4**, **Table 5**) was carried out using a gold loading of 0.5*mol%* (molar ratio Au:1-octyne = 1:200) and produced 75% conversion in 7h. Differently from PA, a mixture of the two possible configurations *E/Z* for the imine was obtained in 25:75 molar ratio.

3.4.4: CATALYST RECYCLING.

The reusability of the AuNPs-(β)sPSB catalyst was also investigated in repeated catalytic hydroamination of PA with AN at 100 °C. In **Table 6** the TOF values for the catalytic runs are reported at 1h of reaction time, to keep the conversions low. In the first catalytic run, AuNPs-(β)sPSB showed an excellent TOF of 226 h^{-1} (entry **1**, **Table 6**). This value drops to 176 h^{-1} in the second run, remaining constant in the further runs (entries **2**-**4**, **Table 6**). The trend of the TOF with the reuse is summarized in **Figure 50.**

Table 6: Recycle tests of AuNPs-(β)sPSB in hydroamination PA with AN.

Entry[a]	Catalyst use	Conv.[b,c] (mol%)	TON[c,d]	TOF[c,e] (h^{-1})
1	1st	45	226	226
2	2nd	35	176	176
3	3rd	35	176	176
4	4th	35	176	176

[a] Reaction conditions: phenylacetylene (25.4 mmol), aniline (30.2 mmol; AN:PA = 1.2), AuNPs-(β)sPSB catalyst (500 mg, molar ratio Au:PA = 1:500), 100 °C, 1 h. [b] Conversion of phenylacetylene. [c] Determined by ^{1}H-NMR analysis of reaction mixture (DMSO-d_6, 25 °C). [d] Turnover number (mol$_{product}$/mol$_{Au}$). [e] Overall turnover frequency (TON/reaction time).

A possible explanation is that the drop into the catalytic activity could be due to a partial gold leaching, promoted by the polymeric matrix swelling with aromatic reactants:[133] this is unlikely because the activity values remain constant in the following catalytic tests.

We propose a partial modification of the surface of the AuNPs in the course of the hydroamination reaction. It is known that the morphology of AuNPs can change after exposure to reagents and solvents, determining a rearrangement of gold atoms on the nanoparticle surface and in particular of that lying on the boundaries of grains, in multigeminate defective nanoparticles.[134]
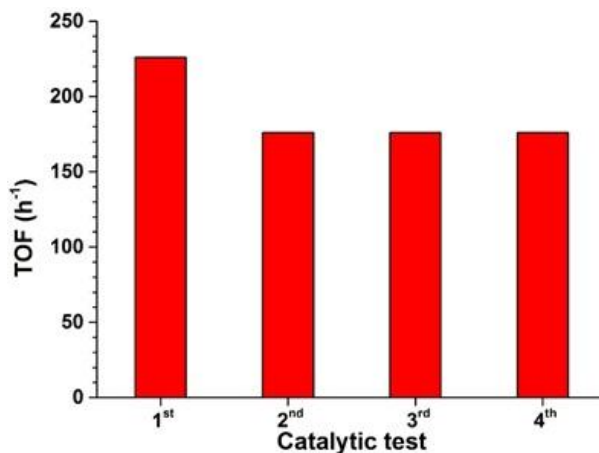
Figure 50: Recycle tests of AuNPs-(β)sPSB.

The coordinatively unsaturated gold atoms located at grain boundaries of defective particles have been also recognized to act as active catalytic sites.[135] To confirm this, the CTEM and HRTEM images for the AuNPs-(β)sPSB catalyst, before and after the first catalytic run, are compared in **Figure 51** where a morphological modification of the AuNPs is actually observed.

AuNPs-(β)sPSB shows twinned and single AuNPs with a spheroidal-like morphology (panels **b** and **c**, **Figure 51**) in the pristine catalyst, whereas a small modifications of the morphology seem to affect the AuNPs (panels **e** and **f**, **Figure 51**) in the reuse.
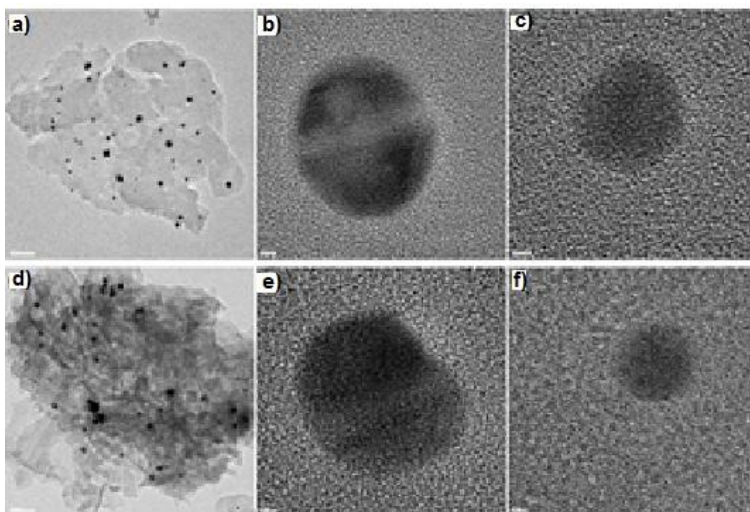
Figure 51: CTEM (panels a, d) and HRTEM (panels b, c, e, f) images of AuNPs-(β)sPSB before use (panels a-c), and AuNPs-(β)sPSB after first catalytic run (panels d-f).

Interestingly the inspection of the WAXD patterns of AuNPs-(β)sPSB before the first catalytic run (**a**, **Figure 52**) and at the end of the catalytic run (**b**, **Figure 52**) shows that the polymer support changes from the compact β crystalline to the nanoporous δ form in the course of the reaction, because of the swelling with the aromatic reactants that yields easy vehiculation of the reagents into the polymer matrix. This results leads to the conclusion that the catalyst performances are independent of the pristine crystalline phase of the polymer support.
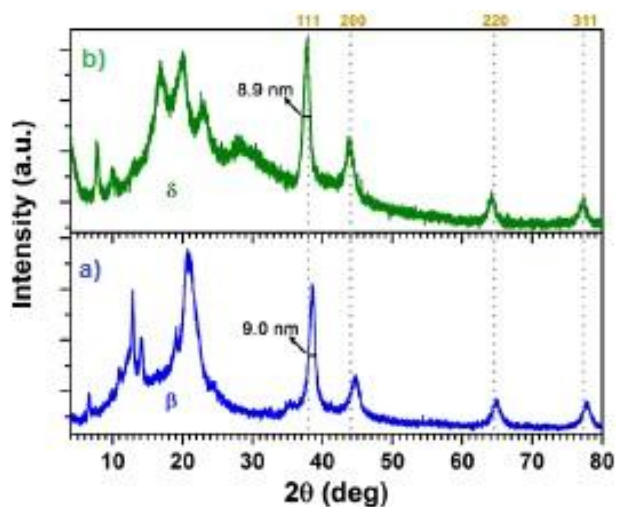
Figure 52: WAXD patterns of a) AuNPs-(β)sPSB before the catalytic run, b) AuNPs-(δ)sPSB after the catalytic run. Greek letters indicate the crystalline form of sPSB. Dotted lines mark the reflections of *fcc* crystalline lattice planes of nanocrystalline Au.

3.4.5: KINETIC INVESTIGATION OF HYDROAMINATION REACTION OF PA WITH AN or AN-d_2

To gain information about the reaction mechanism and the properties of the polymeric support, the kinetic orders of the reagents was evaluated under solvent-free conditions. The reactions of PA with AN were carried out under pseudo-first-order conditions in the range of temperature from 60 to 100°C.
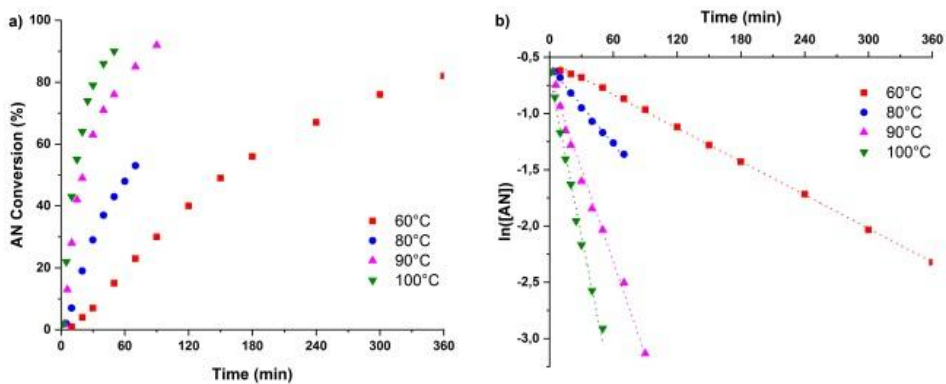
Figure 53: Investigation on kinetic order of AN: a) AN conversion *vs* time plots, b) ln([AN]) *vs* time plots.
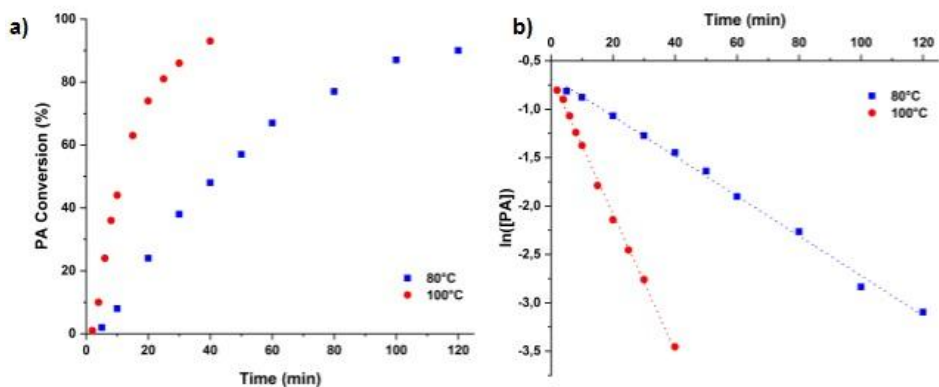
Figure 54: Investigation on kinetic order of PA: a) PA conversion *vs* time plots, b) ln([AN]) *vs* time plots.

The conversion *vs* time plot and the semilog plot of the molar concentration of each reagent, in the presence of the excess of the other

one, provided a pseudo-first order kinetics for both AN and PA (**Figure 53** and **Figure 54**).

Table 7: Hydroamination reaction of PA with AN-d_2 catalyzed by AuNPs-(β)sPSB.

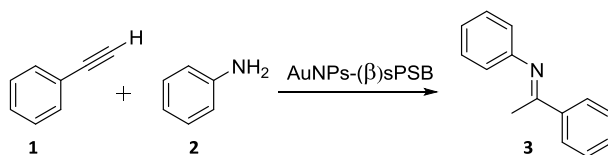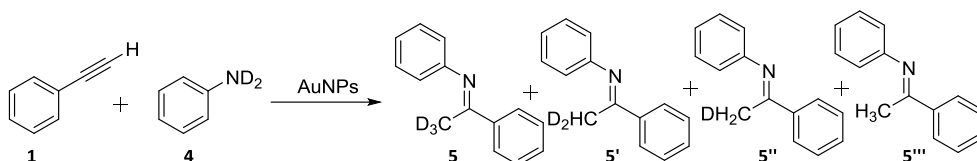| Entry[a]	T (°C)	Conv.[b,c] (mol%)	TON[c,d]	TOF[c,e] (h^{-1})
1	60	27	135	135
2	80	43	215	215
3	100	63	315	315
4	120	83	415	415

[a] Reaction conditions: PA (5.08 mmol), AN-d_2 (6.09 mmol; molar ratio AN-d_2:PA = 1.2), AuNPs-(β)sPSB catalyst (100 mg, molar ratio Au:PA = 1:500), 1h. [b] Conversion of phenylacetylene. [c] Determined by ^{1}H-NMR analysis of reaction mixture (DMSO-d_6, 25 °C). [d] Turnover number (mol$_{product}$/mol$_{Au}$). [e] Overall turnover frequency (TON/reaction time).

To test the possibility of an isotopic effect, hydroamination reaction of PA with *N,N*-Aniline-d_2 (AN-d_2) catalyzed by AuNPs-(β)sPSB was explored under the experimental conditions of **Table 2**; the results are summarized in **Table 7**.

The reagents conversion was low at 60°C (entry **1**, **Table 7**) but linearly increases with increasing the temperature. Surprisingly, the reactivity of

AN-d_2 was higher than AN (compare entries **1-4** of **Table 7** with **Table 2**). Moreover, ^{1}H-NMR analysis of the reaction mixture showed a distribution of deuterated products at the methyl group, with molar ratio 4:22:33:40 respectively for the -CH$_3$, -CDH$_2$, -CD$_2$H and -CD$_3$ derivatives (**Figure 56**).

Surprisingly, the corresponding plots of the reaction of PA with AN-d_2 were found best fitting with a second order kinetics with respect to AN-d_2 and pseudo first order for PA (**Figure 55**).
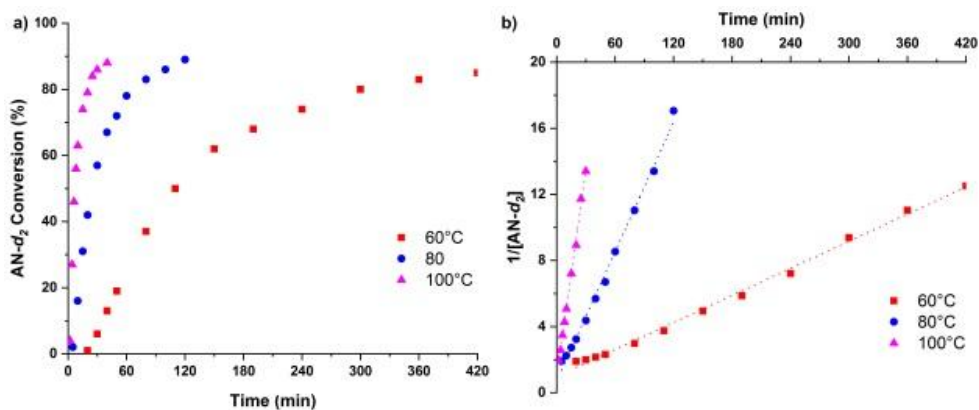
Figure 55: Investigation on kinetic order of AN-d_2: a) AN-d_2 conversion *vs* time plots, b) ln([AN]) *vs* time plots.
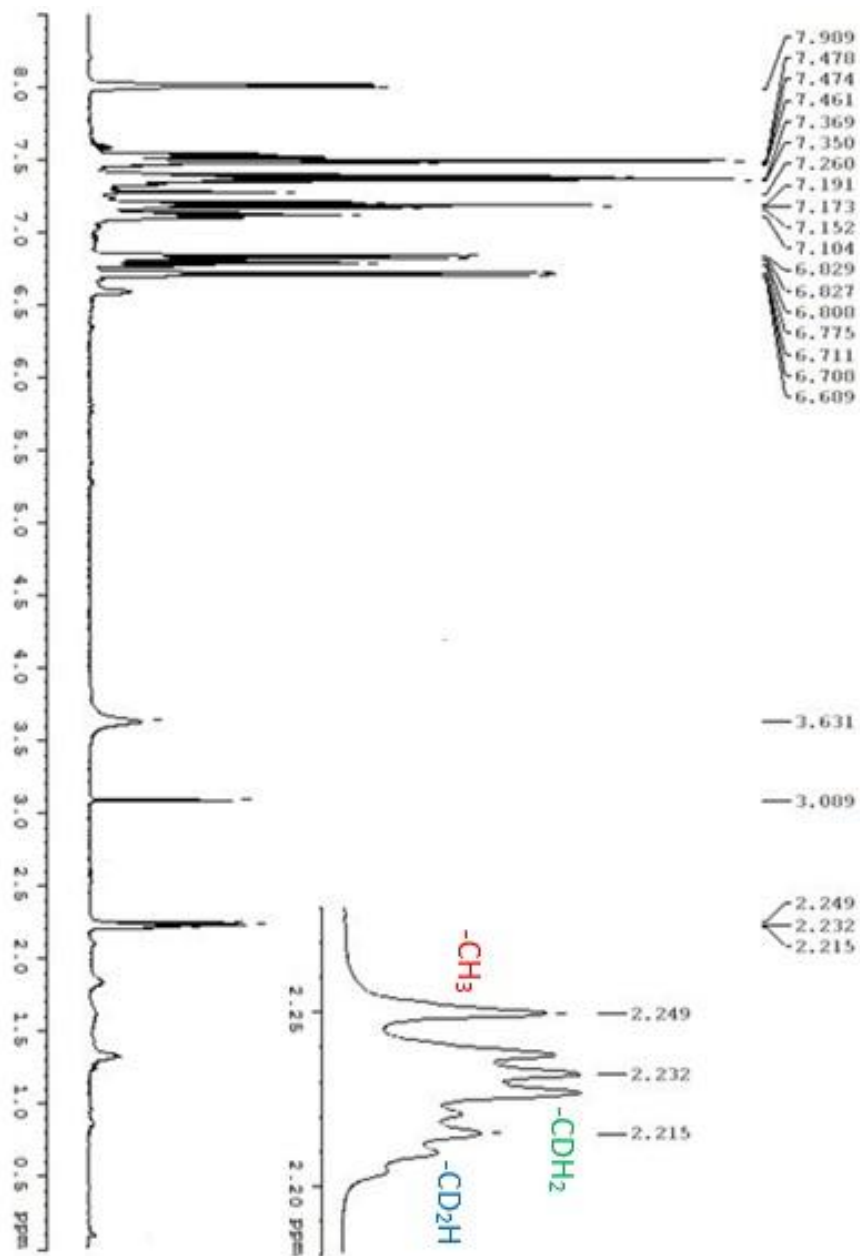
Figure 56: ^{1}H-NMR spectra of the reaction mixture of entry 4, Table 7.

The kinetic constants determined at each temperature are in the range of 0.825–$7.94 \cdot 10^{-4}$ s^{-1} for AN and in the range of 0.455 – 6.94×10^{-3} mol^{-1} s^{-1} for AN-d_2 (**Table 8**).

Table 8: Kinetic parameters for hydroamination reaction of PA with AN or AN-d_2.

Entry[a]	Amine	T (°C)	k	$\Delta H^{\ddagger}$ (kcal/mol)	$\Delta S^{\ddagger}$ (kcal/molK)	$\Delta G^{\ddagger}$ (kcal/mol)
1	AN	60	$0.825 \cdot 10^{-4}$ $\pm 6.6 \cdot 10^{-7}$ s^{-1}			25.7 ± 1.8
2	AN	80	$1.91 \cdot 10^{-4}$ $\pm 5.5 \cdot 10^{-6}$ s^{-1}	13.4 ± 1.8	-0.04 ± 0.04	26.5 ± 1.8
3	AN	90	$4.59 \cdot 10^{-4}$ $\pm 1.6 \cdot 10^{-5}$ s^{-1}			26.8 ± 1.8
4	AN	100	$7.94 \cdot 10^{-4}$ $\pm 3.2 \cdot 10^{-5}$ s^{-1}			27.2 ± 1.8
5	AN-d_2	60	$0.455 \cdot 10^{-3}$ $\pm 8.9 \cdot 10^{-6}$ $mol^{-1} s^{-1}$			26.1 ± 0.9
6	AN-d_2	80	$2.180 \cdot 10^{-3}$ $\pm 5.4 \cdot 10^{-6}$ $mol^{-1} s^{-1}$	16.1 ± 0.9	-0.03 ± 0.03	26.7 ± 0.9
7	AN-d_2	100	$6.94 \cdot 10^{-3}$ $\pm 1.2 \cdot 10^{-5}$ $mol^{-1} s^{-1}$			27.3 ± 0.9

[a] Reaction conditions: PA (10.51 mmol), AN or AN-d_2 (0.66 mmol), AuNPs-(β)sPSB catalyst (100 mg, PA:AN:Au =1035:65:1 molar ratio).

Noteworthy, at low reaction times the reaction rate of AN-d_2 is higher and faster than AN (compare the reaction profiles in panel **a** of **Figure 53** and

panel **a** of **Figure 55**). At prolonged reaction times the reaction proceeds slower (compare the reaction profiles in panel **a** of **Figure 53** and panel **a** of **Figure 55**). From the Eyring plots, the corresponding activation enthalpy ($\Delta H^{\ddagger}$), activation entropy ($\Delta S^{\ddagger}$) and activation free energy ($\Delta G^{\ddagger}$) were obtained.
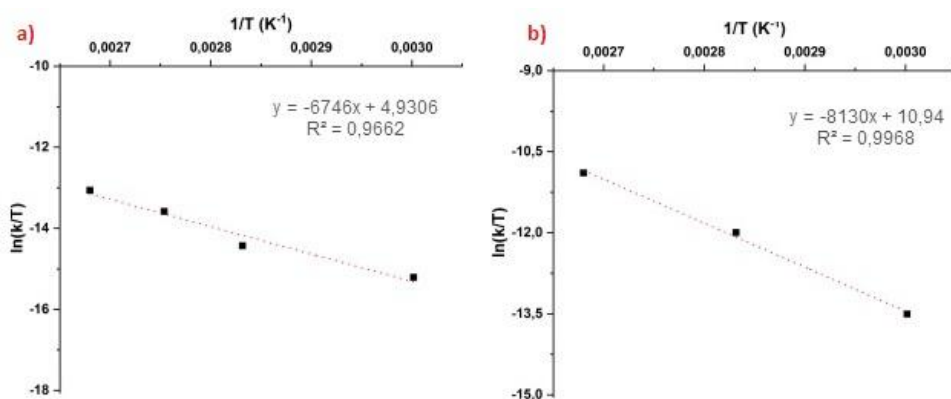
Figure 57: Eyring-Polanyi plot for a) hydroamination reaction of PA and AN (1st order constants), b) hydroamination reaction of PA and AN-d_2 (2nd order constants).

For the hydroamination reaction of AN and PA the corresponding Eyring plot (panel **a** of **Figure 57** and **Table 8**) give a $\Delta H^{\ddagger}$ and $\Delta S^{\ddagger}$ of 13.4±1.8 kcal mol^{-1} and -0.04±0.04 kcal mol^{-1} K^{-1} respectively. The entropic contribution is negative, as expected for a coupling reaction, but it is very small, while the predominant contribution is given by the $\Delta H^{\ddagger}$.

In the case of hydroamination reaction of PA and AN-d_2, the Eyring plot give a $\Delta H^{\ddagger}$ and $\Delta S^{\ddagger}$ of 16.1±0.9 kcal mol^{-1} and −0.03±0.03 kcal mol^{-1} K^{-1} respectively (panel **b** of **Figure 57** and **Table 8**). Also in this case, the entropic contribution is negative and the magnitude of the enthalpic contribution is higher. The small kinetic isotopic effect (KIE) observed (k_H/k_D = 0.18 at 60°C; = 0.09 at 80°C; = 0.11 at 100°C) can be thus considered negligible to the ends of the reaction mechanism. However, the different kinetic order and the different energetic barriers of AN-d_2 suggest a different reaction pathway for this reagent.

3.4.6: DENSITY FUNCTIONAL THEORY (DFT) MODELING.

DFT calculations were carried out to clarify the reaction mechanism for the hydroamination reaction of PA and AN, using an Au_{20} cluster as model. To understand the possible adsorption sites on the surface of the cluster, a Molecular Electrostatic Potential (MEP) analysis was carried out. As it can be observed from panel **a** of **Figure 58** on the Au_{20} cluster, some positive regions (+14 kcal mol^{-1}) where the coordination of PA is allowed and some negative regions (−6.0 kcal mol^{-1}) where the coordination of the AN is consented, are present.
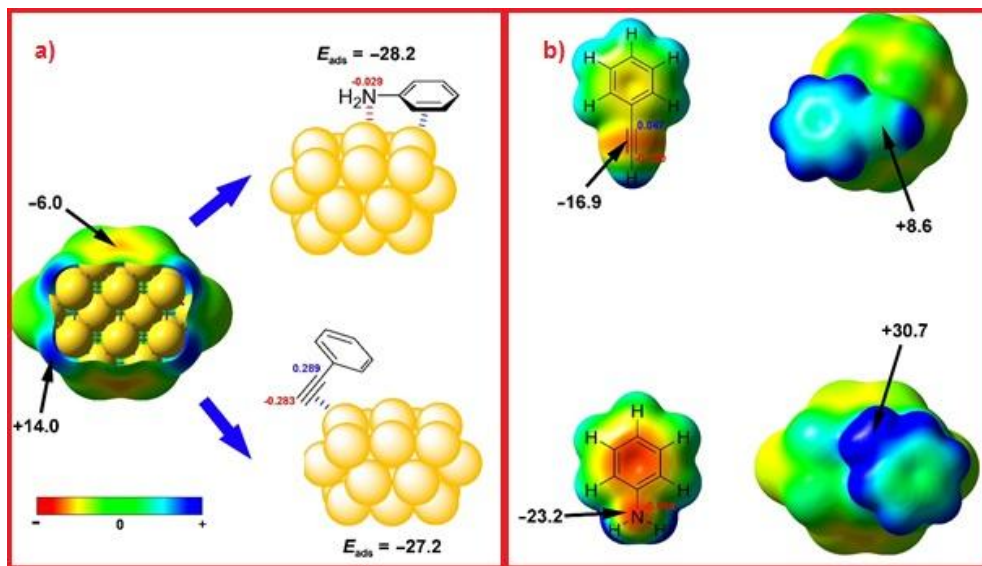
Figure 58: MEP plotted on a) Van der Waals surface and b) Mulliken charges of representative carbons (energies are given in kcal mol^{-1}).

The calculated adsorption energy of AN onto the surface of the cluster was E_{ads} = -28.2 kcal mol^{-1}, while the E_{ads} for the adsorption of PA was -27.2 kcal mol^{-1}. This suggest stronger coordination of the AN, but the nucleophilic properties of AN was strongly reduced after the adsorption (V = +30.7 kcal mol^{-1}, panel **b** of **Figure 58**); therefore a photocatalytic pre-activation of AN or the use of Brønsted bases are required to afford hydroamination reaction.[117,124]

Assuming that the reaction mechanism proceeds through the coordination and activation of AN, by analogy with alcohol oxidation catalyzed by AuNPs,[136] an energetic barrier for this reaction step of ΔG_{298}

= 50.1 kcal mol^{-1} was calculated over Au$_{20}$ cluster (**Figure 59**); this value is too large when compared with the experimental results. The mechanism should not proceed through this step.
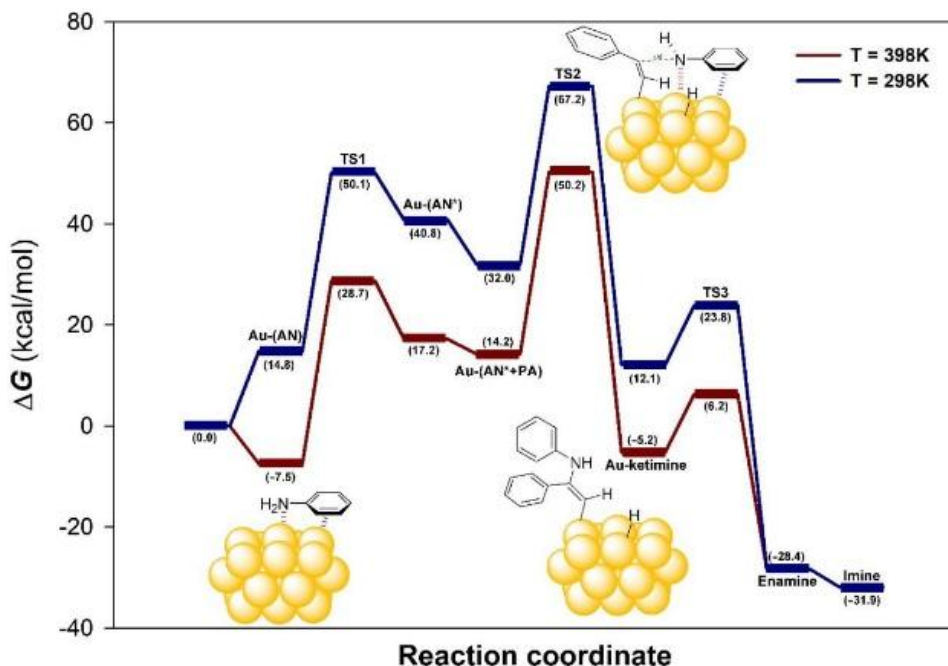
Figure 59: Gibbs energy profile for the hydroamination of PA with AN catalyzed by Au$_{20}$ cluster via pre-activation of AN.

Considering the hypothesis of coordination/activation of PA, from the MEP analysis (**b**, **Figure 58**) this reaction step would modify the electron density of PA, which change from -16.9 kcal mol^{-1} to +8.6 kcal mol^{-1}

favoring the nucleophilic attack of AN. In this case, the activation Gibbs energy of 30.6 kcal mol^{-1} is still too high, suggesting that this reaction step could govern the hydroamination reaction on Au$_{20}$ cluster. Surprisingly, the reaction pathway considering the formation of AN aggregates stabilized by hydrogen bonding (**Figure 60**), yields an activation Gibbs energy ($\Delta G_{Nuc}^{\ddagger}$) for the transition state, corresponding to the nucleophilic attack of the AN to PA, of 21.1 kcal mol^{-1}. To characterize this hydrogen bonding interaction between two anilines, the Bader`s theory Atoms in Molecules was used and a distance $R_{N\cdots H2N}$ = 1.99 Å and an electron density at the hydrogen bonding interaction ρ = 0.0433 a.u., was found (**Figure 61**). Furthermore, the presence of one more AN molecule favors also the proton transfer from the nitrogen atom to the Cβ carbon of the coordinated enamine to the gold surface (**Figure 60**), in analogy to what reported for the hydroamination reactions with hydrazine.[137] This proton transfer involves the intermediate **I$_1$** and the transition state **TS$_{PT}$** to afford the enamine-bound intermediate **I$_2$** (R_{C-Au} = 2.24 Å) that is the thermodynamic product since is more stable than the coordinate imine ($\Delta\Delta G$ = −1.4 kcal mol^{-1}). The following desorption of **I$_2$** from the surface of the Au$_{20}$ cluster is favored ($\Delta\Delta G_{des}$ = −11.1 kcal mol^{-1}) and allows the formation of the enamine tautomer **P$_1$**. This product, subsequently, undergoes to tautomerization to afford the imine product **P$_2$** ($\Delta\Delta G$ = −2.6 kcal mol^{-1}, $\Delta G^{\ddagger}_{tau}$ = −6.2 kcal mol^{-1}). Also in this case, the proton transfer was hypothesized to be mediated by another molecule of AN and the calculated **TS$_{tau}$** shows both N-H bond breaking (R_{N-H} = 1.39 Å) and C-H bond formation (R_{C-H} = 1.49 Å).
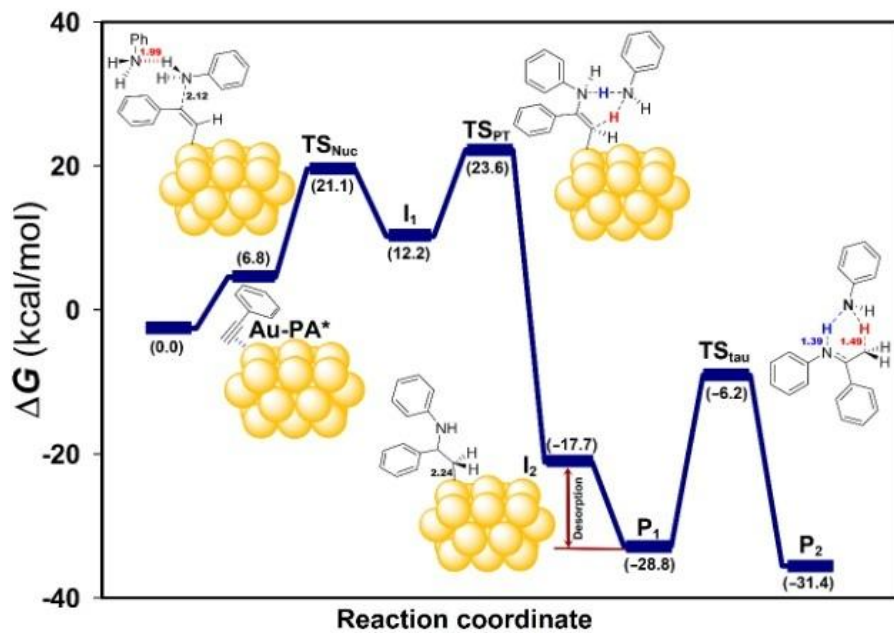
Figure 60: Gibbs energy profile for the hydroamination of PA with AN catalyzed by Au20 cluster via preactivation of PA.
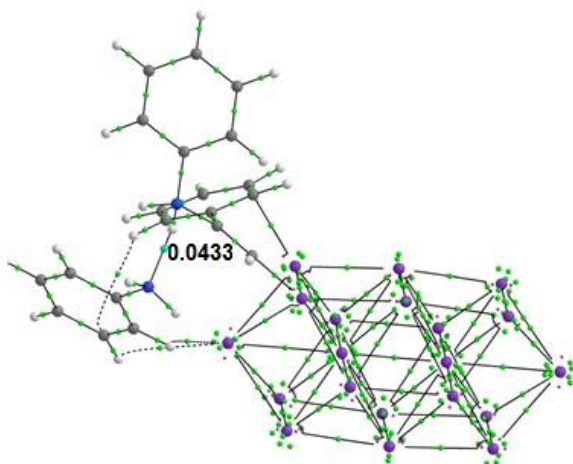
Figure 61: Distribution of bond CPs and bond paths (green spheres) in TS$_{Nuc}$.

3.4.7: MECHANISTIC CONCLUSION.

In this mechanistic study, the preliminary coordination/activation of the alkyne onto the gold surface of the catalyst was proposed in agreement with the alkynophilic character of gold, similarly to homogeneous Au(I) catalysts. The DFT analysis pointed out that the energetic barrier of the nucleophilic attack of AN to PA was assisted by one more AN molecule, determining a decrease of the $\Delta G^{\ddagger}$ value from 30.6 kcal mol^{-1} to 21.1 kcal mol^{-1}. Furthermore, when aggregates with two ANs were considered, the $\Delta G^{\ddagger}$ value dropped to 10.7 kcal mol^{-1}; this finding suggests that this reaction step cannot be considered the rate determining step. In **Figure 60** it is shown that, the proton transfer assisted by one AN yields the transition state **TS$_{PT}$** with an energetic barrier of 23.6 kcal mol^{-1}, that is comparable to the experimental $\Delta G^{\ddagger}$ found for a pseudo-first order kinetic of AN. All these results indicate that this could be the rate determining step of the process. Regarding the reaction carried out with AN-d_2, (paragraph 3.4.5), a mixture of deuterated compounds at the methyl group was found. Carrying out an NMR analysis at 80°C, in absence of AuNPs-(β)sPSB, the scrambling of deuterium between the imine **3** and AN-d_2 was observed (see experimental section). This finding suggests that the enamine-imine tautomerism is not catalyzed by gold and involves the participation of another aniline molecule, as outlined by DFT calculation.

3.5: CONCLUDING REMARKS.

In conclusion, the AuNPs-(β)sPSB catalyst is very efficient in the intermolecular hydroamination reactions of ANs with PAs bearing a variety of EDG and EWG groups. The selective formation of the corresponding ketimine, in the favored *E* configuration, is obtained with high stereo- and regio-control, under mild and neat conditions. The catalyst was recycled up to four times with only a small decrease of the catalytic activity after the first catalytic run. The excellent TOFs of 225 h^{-1} and 320 h^{-1} obtained at 100°C and 120 °C are among the highest value so far reported, for heterogeneous gold catalysts. A new mechanistic pathway has been proposed for the heterogeneous gold catalysts that seems to work similarly to the homogenous Au(I) catalysts, where the coordination/activation of the alkyne onto the gold surface seems to be necessary. An electrostatic polarization of the triple carbon-carbon bond of the PA in presence of EWGs on the aromatic ring favors the nucleophilic attack of AN in the order of OCH_3> Br> CH_3. DFT analysis established that, the formation of hydrogen bonding interaction between ANs leads to an increase in the nucleophilicity of the nitrogen atom, reducing the energetic barrier in the reaction with PA. The $\Delta G^{\ddagger}$ = 23.6 kcal mol^{-1} found for the proton transfer, from the nitrogen atom to the Cα of the enamine intermediate, in the **TS$_{PT}$**, was in good agreement with the $\Delta G^{\ddagger}$ values found in the kinetic study, suggesting that this is the rate determining step of the process. A second-order kinetics for AN-d2 was surprisingly found.

CHAPTER 4

....

INTRAMOLECULAR HYDROAMINATION REACTION CATALYZED BY AuNPs-TiO$_2$

CHAPTER 4: INTRAMOLECULAR HYDROAMINATION REACTION CATALYZED BY AuNPs-TiO₂

4.1: INTRAMOLECOLAR HYDROAMINATION REACTION OF ALKYNES

The intramolecular hydroamination of alkynes bearing an amine functionality is thermodynamically and kinetically more favored in comparison with the intermolecular version. In particular, these reactions have received considerable attention because allow the formation of nitrogen-containing heterocycles, which are very import synthetic targets in pharmaceutical chemistry.[138] In general, intramolecular hydroamination of alkynes require mild reaction conditions, leading to high yields of the products with good or excellent regio and stereo-selectivity. Transition metal catalyzed hydroamination,[110,113,139,140] suffers from short life of the catalyst, low TON and TOF, and limited reaction scope. Titanium or zirconium complexes exhibit very good results in terms of regioselectivity in hydroamination of internal and terminal alkynes, although a low functional group tolerance for these systems can be observed. Rare-earth metal complexes are highly efficient catalysts in the intramolecular hydroamination of alkynes; they exhibit a unique reactivity for the activation of unsaturated organic compounds as a result of the high electrophilicity of the f-element centers, relatively large ionic radii, and high kinetic lability. One limitation is related to high sensitivity to oxygen and moisture. Late-transition metal complexes and in

particular Lewis acidic metal complexes with a d^8 or d^{10} electronic configuration, such as Ru(0), Rh(I), Pd(II), Cu(I), Au(I), Au(III) are doubtless the most employed in intramolecular hydroamination of alkyne showing good activities, better tolerance to different functional groups and lower sensitivity to moisture and oxygen.

4.1.1: INTRAMOLECOLAR HYDROAMINATION OF ALKYNES CATALYZED BY SUPPORTED AuNPs

Heterogeneous metal catalysts active in the intramolecular hydroamination reaction of alkynes are extremely rare and only few works dealing with AuNPs have been published,[141] mainly applied in the synthesis of indoles.[118,133,142–145] In 2009 Haruta et al.[143] reported the one-pot synthesis of indoles from (2-nitroaryl)alkynes catalysed by AuNPs-Fe_2O_3. This reaction proceeds in two step: the hydrogenation/hydroamination of 1-nitro-2-(2-phenylethynyl)benzene **6** (**Figure 62**, R=H) at 60 °C for 1 h, with a H_2 pressure of 2.0 MPa and AuNPs-Fe_2O_3 (loading 2.3mol% Au) in toluene, to produce a mixture of **7** and **8** (**Figure 62**, R=H). In the second step, to complete the conversion of **8** in **7** and to avoid the formation of over reduced anilines, the H_2 pressure was released to atmospheric pressure and the system was heated at 120 °C for 1 h, to give the indole **7** in 87% yield. This one-pot synthesis of indoles was performed with both aliphatic and aromatic substituents (**Figure 62**);

in general, the reaction proceeds in high yields and the alkyne hydrogenation rate is enhanced with electron-poor groups substituent.
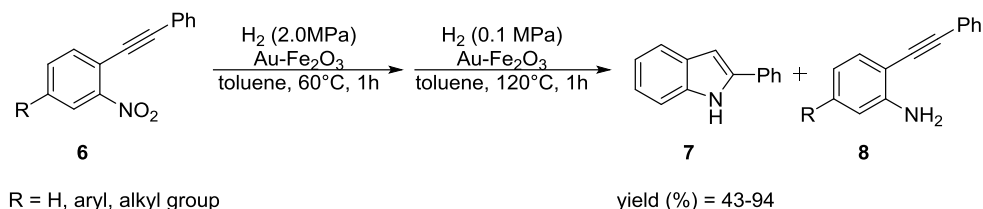
Figure 62: Synthesis of indoles by AuNPs-Fe₂O₃ catalyst under hydrogenation conditions.

Some years later a cycloisomerization of 2-alkynylanilines to indoles (**Figure 63**) along with a domino cycloisomerization/C-H oxidative homocoupling to 3,3'-biindolyl products was reported (**Figure 64**).[142]
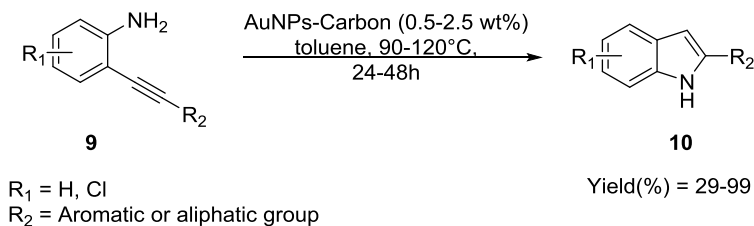
Figure 63: Cycloisomerization of 2-alkynylanilines catalyzed by Au/carbon.

In this case, the AuNPs-C catalyst was used and the effect of various substituents on both the alkyne moiety and aryl ring was studied. In general, with electroneutral substituents, (R_2= Ph or p-MeC$_6$H$_4$), cycloisomerization takes place in high yields by using 0.5 *wt%* catalyst loading at 90°C in 24h. When electron-poor substituents were employed (R_2= p-(CH$_3$CO$_2$)C$_6$H$_4$ or p-NO$_2$C$_6$H$_4$), higher catalyst loading and longer reaction time were required (90°C, 48h, 1.5 wt% catalyst loading). For strongly electron-poor substituents (R_2= C$_6$F$_5$ or o-pyridine), an increase of the reaction temperature to 120°C was found necessary for the reaction to take place.
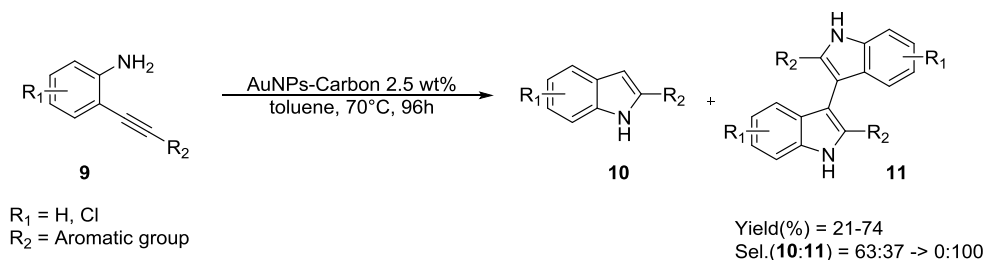
Figure 64: Domino cycloisomerization/indole homocoupling on AuNPs-Carbon catalyst.

It was also found that increasing the catalyst loading, extending the reaction time and using lower temperatures to suppress possible side reactions, **11** was isolated in fair to good yields (**Figure 64**), with both electroneutral or electronrich alkynylanilines. However, the

homecoupling reaction readily proceeds on the carbon support; when the gold catalyst loading is increased, the catalytic activity increases and thus a cooperative catalysis is invoked.

More recently Hammond *et al.*[118] reported the synthesis of indoles from 2-alkynylanilines using the commercial AuNPs-TiO$_2$ catalyst assisted by microwave heating (**Figure 65**). With arylalkynes the corresponding indole was obtained in good yields in 1h at 120°C; aliphatic alkynes need acid promoters (5 mol % of H$_3$PO$_4$·12WO$_3$) to improve the reaction rate.

R$_1$ = H, Me, Halogen
R$_2$ = Aromatic group

Yield (%) = 83-97
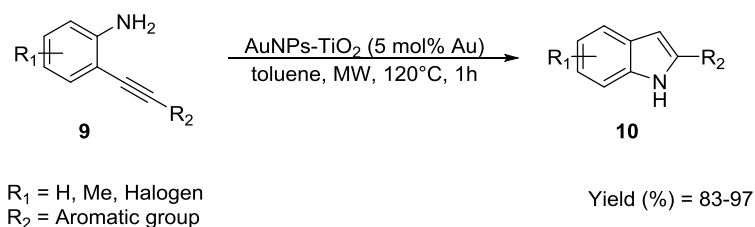
Figure 65: Indoles synthesis promoted by MW using AuNPs-TiO$_2$ as catalyst.

The polymer microencapsulated Au(III) catalyst supported on SiO$_2$ (MC-AuNPs-SiO$_2$) was used in indole synthesis by the Kobayashi group.[133] The polymer matrix consists of a functionalized polystyrene resin bearing the pending PEG-OH side groups shown in **Figure 66**.

(x : y = 60 : 40)
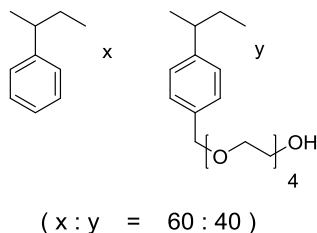
Figure 66: Copolymer used by Kobayashi *et al.*[130]

The tetraethylene glycol units played a crucial role in the gold immobilization and stabilization. The reactions were conducted in hexane at room temperature in the presence of 2 mol% of Au (**Figure 67**). The catalyst gives indoles in good yields also with aliphatic alkynes whereas is inactive with heterocycles.

R = aromatic or aliphatc group

Yield (%)= 81-95
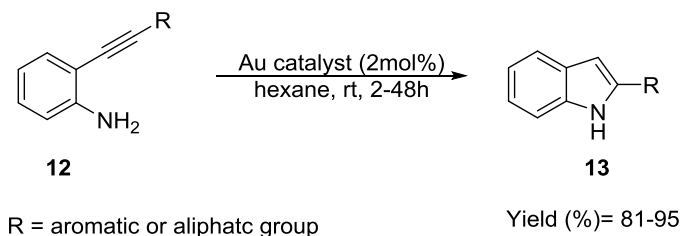
Figure 67: Indole synthesis catalyzed by MC Au-SiO$_2$.

In conclusion, heterogeneous gold catalysts are active in intramolecular hydroamination of alkynes under high temperature and/or long reaction time.

4.2: HYDROAMINATION OF ALKYNYL ANILINES FOR THE SYNTHESIS OF TETRAHYDROQUINOLINES

Among the N-heterocycles, tetrahydroquinolines (THQs) exhibit a benzene ring merged with a piperidine ring (1,2,3,4-tetrahydroquinoline **Figure 68**, **a**) or less usually, a cyclohexene ring merged with a pyridine ring (5,6,7,8-tetrahydroquinolines **Figure 68**, **b**).
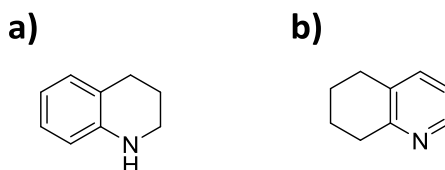
Figure 68: structural rings of a) 1,2,3,4-THQ b) 5,6,7,8-THQ.

The natural and synthetic 1,2,3,4-tetrahydroquinolines are interesting synthetic targets since they show both biological and pharmacological activities.[146,147] For example, some THQs (**Figure 69**) act as chemotherapeutic agents interacting with retroviral targets relevant to anti-HIV therapy;[148] THQs are also active against antibacterial targets or display antifungal, antiparasitic or anticancer activities (**Figure 69**). Moreover THQs have found application in asymmetric synthesis as chiral ligands.[149]
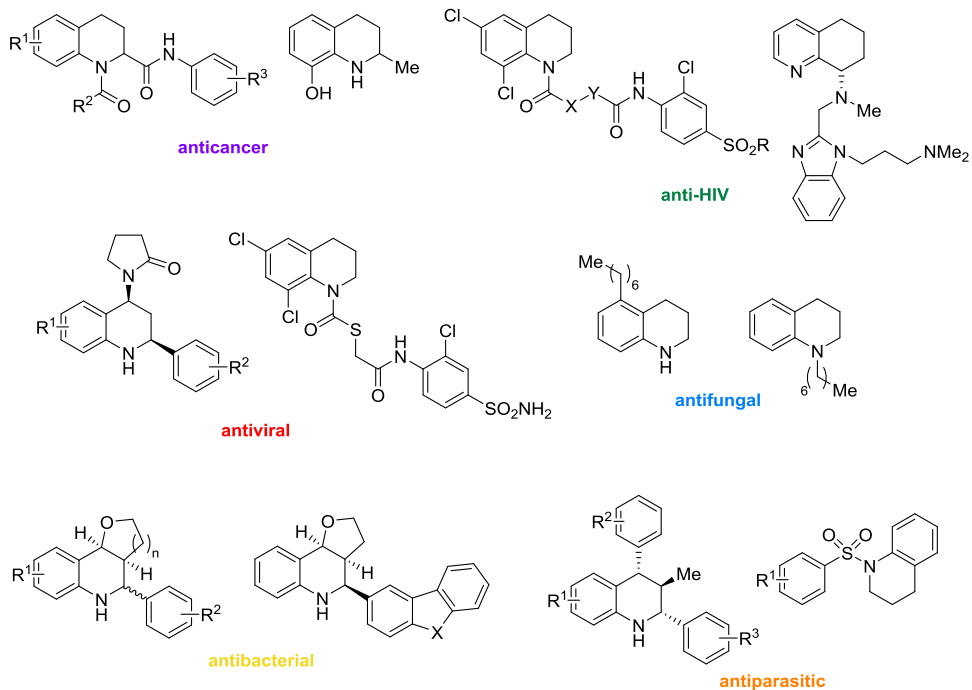
Figure 69: Bio-active 1,2,3,4-tetrahydroquinolines.

Different approaches have been proposed for the synthesis of THQs [146,147] most of them consisting of the ring closure of the piperidine ring through the formation of a carbon-nitrogen or carbon-carbon bond, in functionalized aromatic compounds (**Figure 70**). Only few papers describe the synthesis of THQs via intramolecular hydroamination reactions.[150–152]
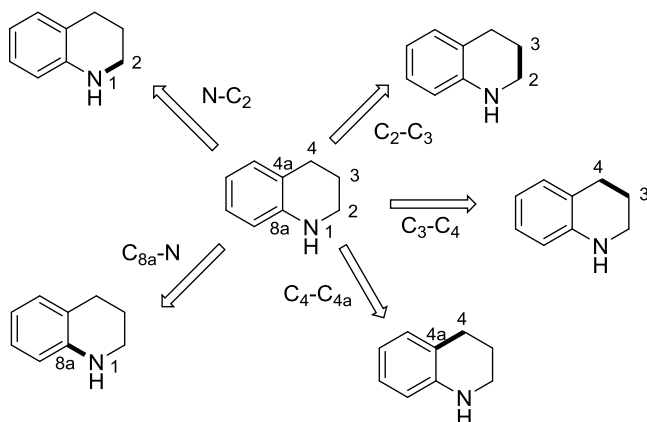
Figure 70: Approach to the synthesis of 1,2,3,4-tetrahydroquinoline via C-C and C-N bonding formation in aromatic compounds.

4.2.1: SYNTHESIS OF TETRAHYDROQUINOLINES BY INTRAMOLECULAR HYDROAMINATION REACTION OF ALKYNES

In 2007 Yamamoto *et al.*[150] reported the synthesis of 2-alkenyl-1,2,3,4-tetrahydroquinolines through the intramolecular hydroamination of anilino-alkynes catalyzed by Pd(PPh$_3$)$_4$ and benzoic acid as acid promoter (**Figure 71**). Different aniline-alkynes having a free amino group or EDGs at the N-atom, afforded the corresponding THQs in good to excellent yields. However, EWGs at the nitrogen atom led to failure of the reaction. An attempt to the enantioselective synthesis of THQs was done by introducing (*R,R*)-RENORPHOS as chiral ligand in the reaction mixture; under these conditions the THQs were obtained only in moderate yield and low enantioselectivity (*ee* up to 78%).

Reaction scheme:

Pd(PPh$_3$)$_4$ (20mol%)
PhCO$_2$H (50mol%)
120°C, toluene

14 → **15**

R = H, Me or Bn   Yield (%) = 63-98
R$_1$ = aryl or alkyl group
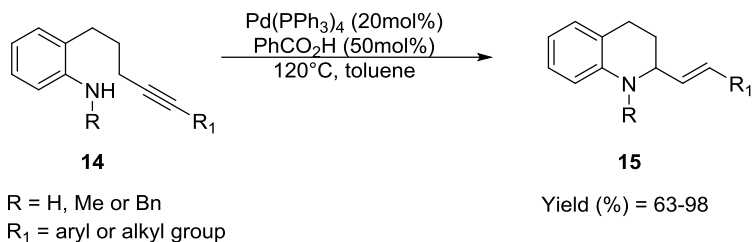
Figure 71: Palladium catalyzed synthesis of tetrahydroquinolines.

Some years later, the one pot reaction consisting of consecutive intramolecular hydroamination/asymmetric transfer hydrogenation of 2-(2-propynyl)anilines to THQs catalyzed by the Au(I) complex (CH$_3$AuPPh$_3$) (**Figure 72**) was reported in the presence of the chiral Brønsted acid ((R)-3,3'-Bis(9-phenanthryl)-1,1'-binaphthalene-2,2'-diyl hydrogen phosphate) and Hantzsch ester,[151] in toluene at room temperature for 16h. Different aromatic or aliphatic substituents on the propynyl moiety were tested with excellent results in term of yields and enantioselectivity, also under the variation of substituents on the aniline moiety.
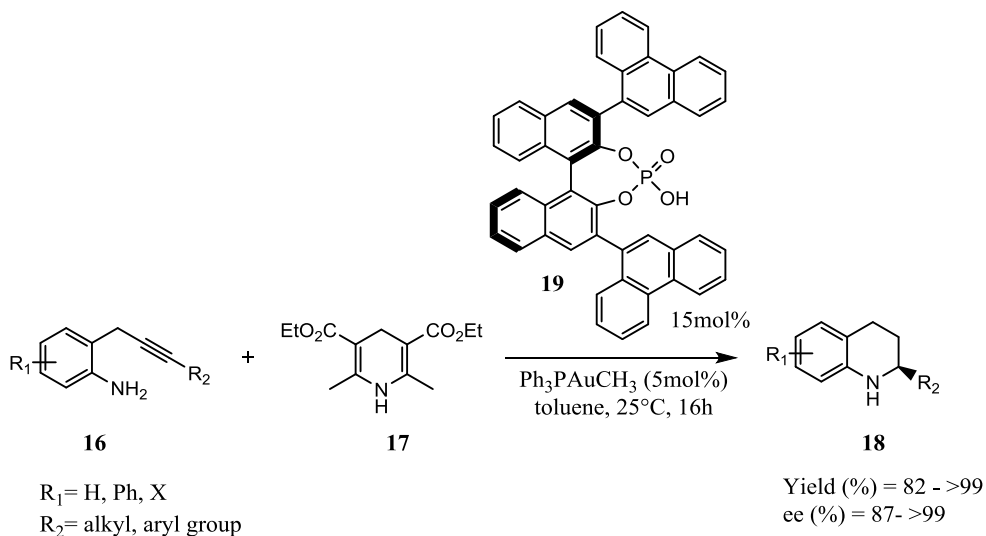
Figure 72: Homogeneous Au(I) catalyzed synthesis of tetrahydroquinolines.

4.2.1.1: MECHANICISTIC HYPOTHESIS ON THE TETRAHYDROQUIOLINE SYNTHESIS CATALYZED BY HOMOGENEOUS Au(I) CATALYST

The mechanistic pathway for the synthesis of THQs catalyzed by homogenous Au(I) catalyst is shown in **Figure 73**.[151] As in intermolecular hydroamination reaction,[122] the intramolecular reaction involves a carbon-carbon multiple bond activation by coordination of the π-system to Au(I) followed by the nucleophilic attack of the amine to form the 1,4-dihydroquinoline product (**Figure 73**, **a**-**b**). This intermediate isomerizes to 3,4-dihydroquinolinium complex in the presence of a Brønsted acid and subsequentially undergoes to an asymmetric hydride transfer by the

Hantzsch ester, to afford the enantiopure THQs as final product (**Figure 73**, **c**-**e**).[153] The regeneration of the Brønsted acid results from a proton transfer, which produces the formation of Hantzsch pyridine as byproduct (**Figure 73**, **f**).
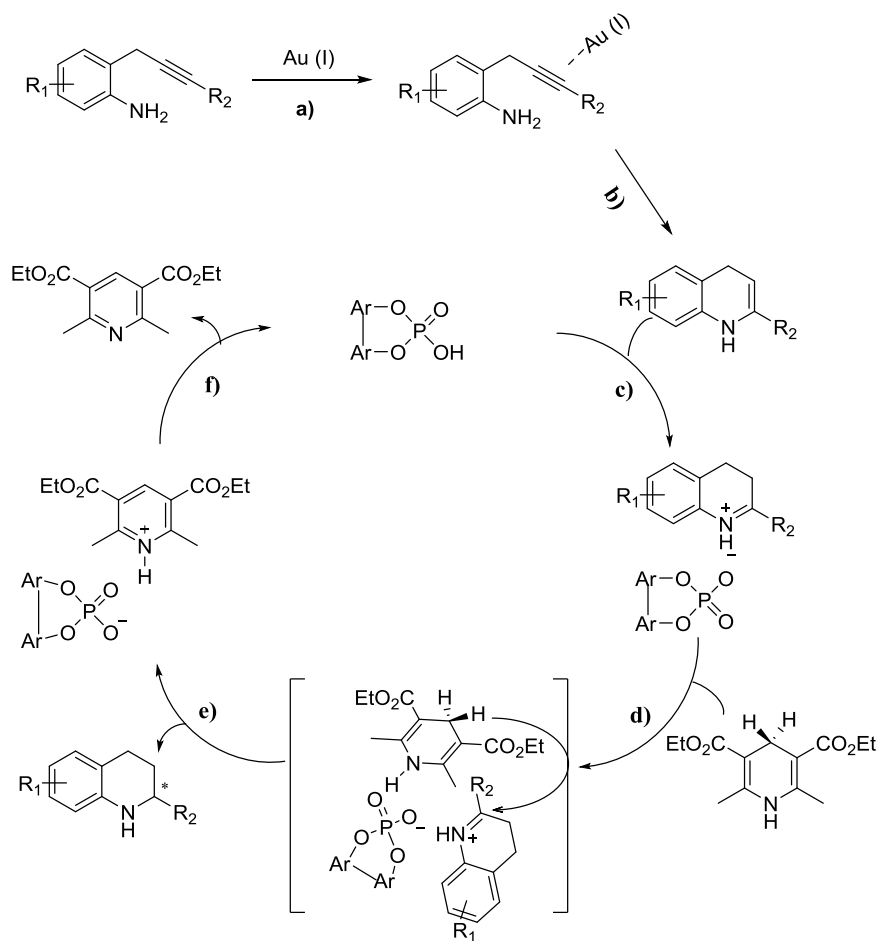
Figure 73: Reaction pathways for THQs synthesis catalyzed by Au(I) catalyst.

4.3: TETRAHYDROQUINOLINES SYNTHESIS CATALYZED BY AuNPs-TiO₂

Aiming to design a heterogeneous gold catalyst suitable in THQs synthesis, we tested the commercial AuNPs-TiO₂ successfully applied in a variety of organic reaction miming homogenous gold catalysts. The intramolecular hydroamination reaction catalyzed by AuNPs-TiO₂ in combination with a chiral phosphoric acid and Hantzsch ester was performed to convert 2-(2-propynyl)anilines into THQs (**Figure 74**).
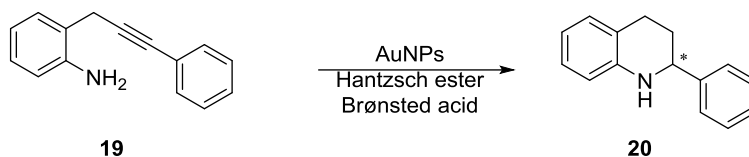
Figure 74: Tetrahydroquinolines synthesis catalyzed by AuNPs.

In a protective atmosphere of nitrogen, 2-(2-propynyl)aniline **19** reacted in presence of AuNPs-TiO₂ (5*mol%*Au loading) with Brønsted acid (*R*)-**23** (5*mol%*, **Figure 75,** (*R*)-1,1-Binaphthyl-2,2-diyl hydrogenphosphate) and Hantsch ester **25** (molar ratio **25:19** of 1.2) in Toluene at 60 °C for 2h, to give a mixture of tetrahydroquinoline **20** and indole **21** (entry **1**, **Table 9**) with a selectivity in the racemic tetrahydroquinoline **20** of 71%.

131

Table 9: Conversion of 2-(2-propynyl)aniline into THQ catalyzed by AuNPs-TiO₂.
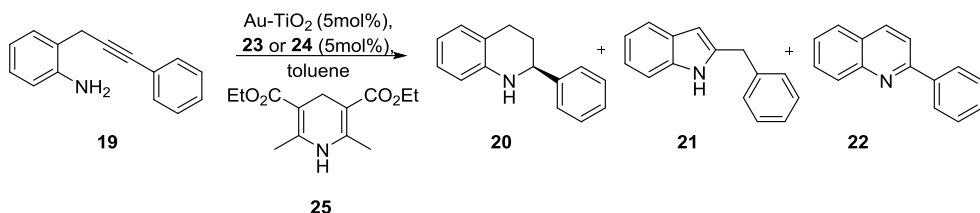
Entry	Brønsted acid	T (°C)	time (h)	Conv (mol%)[b]	Yield (mol%)[b] 20	21	22	Sel. (mol%)[b] 20	21	22	ee (%)[c] 20
1	23	60	2	92	71	21	-	77	23	-	2
2	24	60	2	92	73	19	-	80	20	-	74
3[d]	24	60	2	65	53	12	-	82	18	-	68
4	24	80	1	86	63	19	4	73	23	4	56
5	24	40	3	83	69	14	-	83	17	-	86
6[e]	24	40	3	13	10	3	-	77	22	-	74
7[f]	24	40	3	97	77	18	2	80	18	2	76

[a] Reaction conditions: 2-(2-propynyl)aniline 19 (0.1 mmol), Hantsch ester 25 (0.12 mmol), AuNPs-TiO₂ (100mg, molar ratio Au:2-(2-propynyl)aniline 19 = 1:20), Brønsted acid (0.005 mol), 1mL toluene. [b] Determined by ¹H-NMR analysis of reaction mixture (CDCl₃, 25 °C). [c] Determined by HPLC analysis. [d] Reaction in presence of air. [e] Using 20mg of catalyst (molar ratio Au:2-(2-propynyl)aniline 19 = 1:100). [f] Using 200 mg of catalyst (molar ratio Au:2-(2-propynyl)aniline 19 = 1:10).

When the Brønsted acid (*R*)-**24** ((*R*)-3,3'-Bis(9-phenanthryl)-1,1'-binaphthalene-2,2'-diyl hydrogen phosphate), **Figure 75**) was tested in

the same reaction, the tetrahydroquinoline **20** was obtained with a 74%

ee (entry **2**, **Table 9**) to confirm that the steric hindrance of the Brønsted

acid (*R*)-**24** plays an important role in the enantioselectivity control of the

reaction. In air (entry **3**, **Table 9**) the reaction proceeds with a decrease

of the yield (53%) and of enantioselectivity (60% *ee*). The reaction

temperature was also varied to understand if this parameter affects the

regioselectivity and enatioselectivity of the reaction (entries **4-5**, **Table 9**).

At 80°C and shorter reaction time, the enantioselectivity was lower,

whereas at 40°C the **20** was obtained in 83% selectivity and 86% *ee* in only

3h. The enantiomeric excesses were determinate by HPLC analysis (see

experimental section), while the absolute (*S*) configuration of THQ **20** was

assigned for comparison between the optical rotation measured ([α]$_D$,

see experimental section) and that reported in the literature[151] for this

compound.
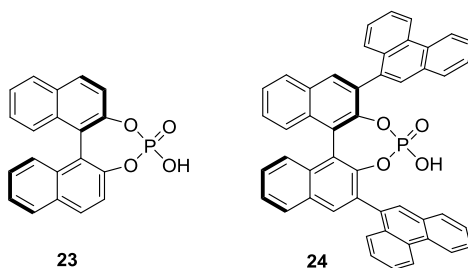
Figure 75: Brønsted acids screened.

The amount of catalyst has been thus varied (entries **6-7**, **Table 9**). A gold catalyst loading of 1*mol%* was unproductive (entry **6, Table 9**), while the reaction proceeds more rapidly at Au loading of 10*mol%*; unfortunately under this condition a decrease in enantioselectivity (compare entries **5** and **7** of **Table 9**) was observed. Differently from homogenous gold catalyst,[151] the heterogeneous gold catalyst AuNPs–TiO$_2$ yielded the formation of indole like structure. In all of these reactions, the tetrahydroquinoline **20**/indole **21** molar ratio remains unchanged. In conclusion, the reaction temperature, amount of the gold catalyst and nature of the Brønsted acid, do not seems to influence the amount of indole **21** formed, which is observed for the first time in this reaction.

4.3.1: SCREENING OF HETEROGENEUS GOLD CATALYSTS

The activity and selectivity of AuNPs-TiO$_2$ catalyst were compared with other commercial gold catalysts; in general, AuNPs-TiO$_2$ provided the best catalytic performance (compare entry **1** with entries **2**-**4** of **Table 10**).

Table 10: Screening of the catalyst.
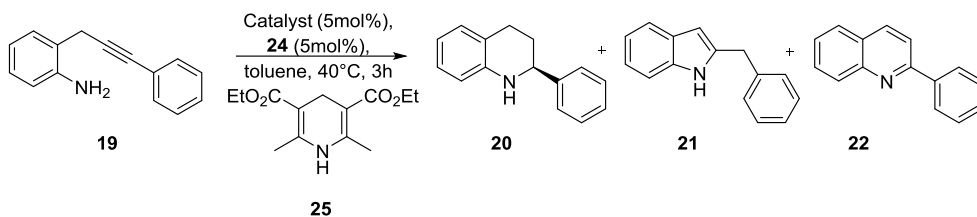
Entry	Catalyst	Conv (mol%)[b]	Yield (mol%)[b]			Sel. (mol%)[b]		
			20	21	22	20	21	22
1	AuNPs-TiO$_2$	83	69	14	-	83	17	-
2	AuNPs-CB	7	7	-	-	99	-	-
3	AuNPs-ZnO	16	11	2	2	70	15	15
4	AuNPs-Al$_2$O$_3$	56	46	10	-	82	18	-

[a] Reaction conditions: 2-(2-propynyl)aniline 19 (0.1 mmol), Hantsch ester 25 (0.12 mmol), catalyst (100mg, molar ratio Au:2-(2-propynyl)aniline 19 = 1:20), Brønsted acid 24 (0.005 mol), 3h at 40°C in 1mL toluene. [b] Determined by ^{1}H-NMR analysis of reaction mixture (CDCl$_3$, 25 °C).

4.3.2: SCREENING OF SOLVENTS

The reduction of quinolones to THQs using a Brønsted acid and Hantzsch ester system is, in general, well performed in aromatic and/or chlorinated solvents, giving high performance in terms of yields and enantioselectivity.[153] In terms of green chemistry, these solvents are certainly not sustainable and the evaluation of more green solvents could

disclose new opportunities. Thus, a screening of different solvents has been carried out and the results are shown in **Table 11**.

As expected, good results in terms of yields and enantioselectivity were achieved, in 3h in toluene and CH_2Cl_2 (entries **1**-**2**, **Table 11**); these results were thus used as benchmark for other solvents. Since the reduction of quinolones in aqueous solution has been already assessed,[154] the reaction was explored in water/toluene mixture (v/v = 1:1) and brine (entries **3**-**4**, **Table 11**). The reaction in the former mixture of solvents gave **20** in excellent enantioselectivity (88% *ee*), even if in only moderate conversion (42%) in 3h (entry **3**, **Table 11**). In brine the tetrahydroquinoline **20** was obtained in poor yield (22%); in the latter case the poor solubility of the reagent **19** in the aqueous medium (entry **4**, **Table 11**) is an important factor to be considered. Surprisingly the reaction proceeds admirably in polar coordinating solvents such as THF and 2-MeTHF, (entries **5**-**6**, **Table 11**). In THF the product **20** was obtained with 67% yield and an enantioselectivity of 88% (entry **5**, **Table 11**) whereas in the greener solvent 2-MeTHF, the tetrahydroquinoline **20** was obtained in slightly lower yield (60%) but excellent enantioselectivity of 90% (entry **6**, **Table 11**). These values strongly confirm the possibility to perform intramolecular hydroamination in more green conditions. In acetonitrile (entry **7**, **Table 11**) only a moderate yield and enantioselectivity were obtained for **20**.

Table 11: Screening of the one pot THQS synthesis catalyzed by AuNPs in different solvents.
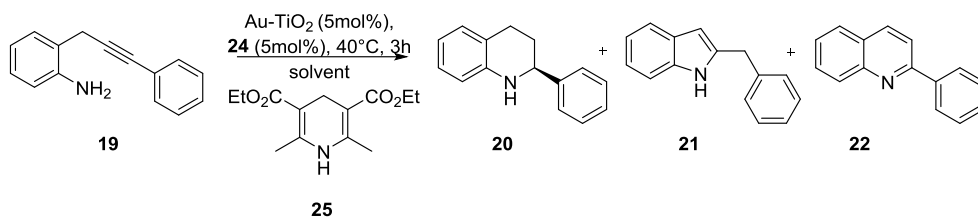
Entry	Solvent	Conv (mol%)[b]	Yield (mol%)[b]			Sel. (mol%)[b]			ee (%)[c]
			20	**21**	**22**	**20**	**21**	**22**	**20**
1	Toluene	83	69	14	-	83	17	-	86
2	Ch₂Cl₂	86	71	15	-	83	17	-	88
3	Toluene/H₂O	42	35	6	-	84	15	-	88
4	H₂O brine	28	22	5	-	80	20	-	nd
5	THF	87	67	15	4	78	18	4	88
6	2-MeTHF	77	60	13	4	78	17	5	90
7	CH₃CN	50	40	8	2	79	17	4	72

[a] Reaction conditions: 2-(2-propynyl)aniline 19 (0.1 mmol), Hantsch ester 25 (0.12 mmol), AuNPs-TiO₂ (100mg, molar ratio Au:2-(2-propynyl)aniline 19 = 1:20), Brønsted acid 24 (0.005 mol), 3h at 40°C in 1mL of solvent. [b] Determined by ¹H-NMR analysis of reaction mixture (CDCl₃, 25 °C). [c] Determined by HPLC analysis.

Considering all the above results, it can be concluded that the nature of the solvent has not a relevant effect on the formation of the indole **21**. A possible explanation for the formation of **20** and **21** using AuNPs catalysts

can be attributed to the lower electrophilicity of Au(0), compared to Au(I) of the homogeneous gold catalyst, determining a lower regioselectivity in the ring closure.

4.3.3: MECHANISTIC INSIGHTS

To rationalize these findings a possible mechanism for the synthesis of THQs by intramolecular hydroamination reaction of 2-(2-propynyl)anilines catalyzed by Au(0) is proposed (**Figure 76** and **Figure 77**). The first step sees the activation of the alkyne by coordination to surface of the catalyst (**Figure 76**, **a**), followed by the nucleophilic attack of the amine. This attack can then follow two main routes (**Figure 76**, **b** or **d**): the *endo* attack of the amine to the C≡C bond to produce 1,4-dihydroquinoline as product (**Figure 76**, **b**-**c**); or an *exo* attack of the amine to the C≡C bond to afford an enamine intermediate that gives the indole **21** as the final product, after intramolecular rearrangement (**Figure 76**, **d**-**g**). In the presence of a Brønsted acid and Hantzsch ester, the 1,4-dihydroquinoline undergoes a second catalytic cycle (**Figure 77**)[153]. Initially, a proton transfer from the Brønsted acid to the 1,4-dihydroquinoline produces an iminium intermediate (**Figure 77**, **h**) which subsequentially evolves to the desired tetrahydroquinoline **20** (**Figure 77**, **i**), through an enantioselective hydride transfer by the Hantzsch ester. A proton transfer will recycle the Brønsted acid and generate the Hantzsch pyridine (**Figure 77**, **l**) at the end of the catalytic cycle.
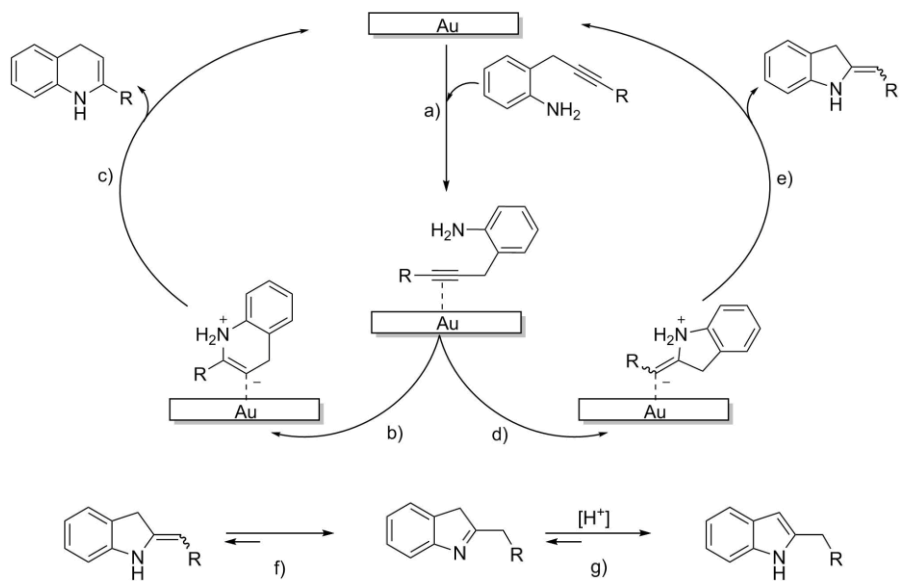
Figure 76: possible mechanistic pathway for the intramolecular hydroamination of 2-(2-propynyl)anilines catalyzed by AuNPs-TiO₂.
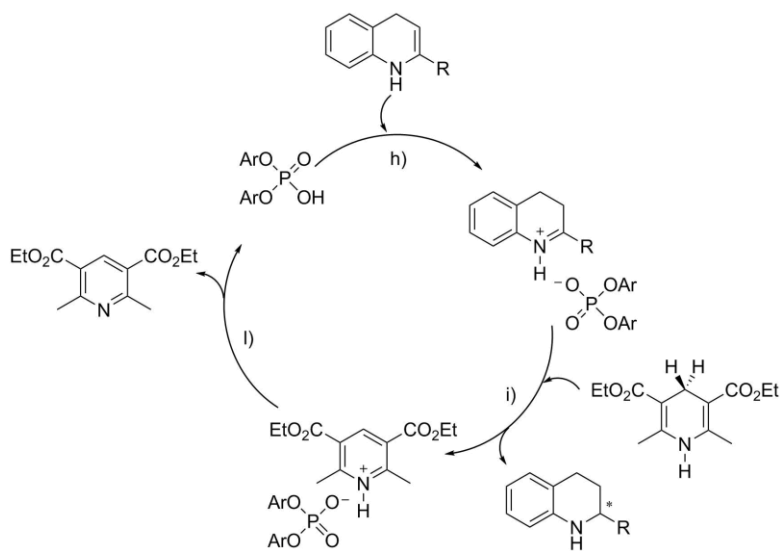
Figure 77: proposed catalytic cycle for the reduction of 1,4-dihydroquinoline to THQ.

Regarding to the absolute (*S*) configuration found for the THQ **20** a possible explanation can be found considering that the chiral phosphoric acid (*R*)-**24** acts as a bifunctional catalyst, in which the acidic proton and the P=O moiety of the catalyst form hydrogen bonds with the 1,4-dihydroquinoline and the Hantzsch ester respectively. In this well-defined cyclic transition state structure (**Figure 78**), the 1,4-dihydroquinoline is activated by protonation of the chiral Brønsted acid, forming the iminium intermediate; the hydride nucleophile (deriving from the Hantzsch ester) approaches the iminium intermediate from his less hindered face. Considering the axial chirality (*R*) of the phosphoric acid **24**, the less hindered is the *Re* face since the *Si* face is shielded by the large phenanthryl group of the catalyst. This concerted transition state leads to the (*S*)-THQ **20**.[153]
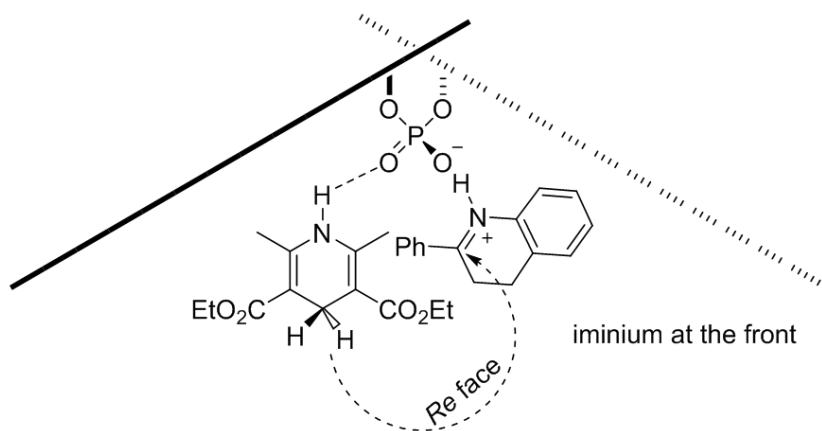
Figure 78: proposed structure for the cyclic transition state of Brønsted acid, Hantzsch ester and iminium intermediate.

4.3.4: SYNTHESIS OF SUBSTITUTED TETRAHYDROQUINOLINES

Table 12: Synthesis of THQs promoted by AuNPs-TiO₂.
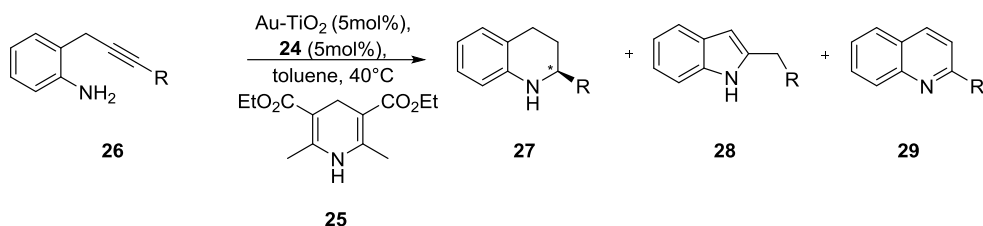
Entry	Reagent	time (h)	Conv (mol%)[b]	Yield (mol%)[b]			Sel. (mol%)[b]			ee (%)[c]
				27	28	29	27	28	29	27
1		3	83	69	14	-	83	17	-	86
2		1/2	99	95	-	-	99	-	-	99
3		3	67	66	1	-	98	2	-	70

[a] Reaction conditions: reagent 26 (0.1 mmol), Hantsch ester 25 (0.12 mmol), AuNPs-TiO₂ (100mg, molar ratio Au:reagent 26 = 1:20), Brønsted acid 24 (0.005 mol),), at 40°C in 1mL of toluene. [b] Determined by ^{1}H-NMR analysis of reaction mixture (CDCl₃, 25 °C). [c] Determined by HPLC analysis.

In this mechanistic contest, the electronic properties of the aromatic ring of the PA can play an important role in controlling the regioselectivity of the nucleophilic attack of the nitrogen atom to the π-system of the

alkyne. For this reasons different substituted 2-(2-propynyl)anilines have been synthesized (for the synthesis detail see experimental section) and tested in the reaction using AuNPs-TiO$_2$ as catalyst (**Table 12**).

All the reactions were performed in toluene at 40°C. In general, electron-donating substituents were well tolerated, providing excellent conversion and enantioselectivity. The absence of aromatic substituents in PA allowed quantitative conversion of the reagent in 3h producing THQ and indole in 5:1 molar ratio (entry **1**, **Table 12**). The absolute (*S*) configuration of THQ **20** was assigned for comparison between the optical rotation measured ([α]$_D$, see experimental section) and that reported in the literature[151] for this compound. The same procedure was also performed for the other THQs. 2-(3-(4-methoxyphenyl)prop-2-ynyl)aniline yields (*S*)-2-(4-methoxyphenyl)-1,2,3,4-tetrahydroquinoline as the only product with a remarkable enantioselectivity of 99% and a complete conversion in only 30 min (entry **2**, **Table 12**). The *p*-methoxy group thus polarizes the π-system of the alkyne coordinated to the gold surface determining an increase of the reaction rate and regioselectivity of the reaction, ruling out the ring closure to indole. DFT calculations carried out over Au$_{20}$ cluster, for the intermolecular hydroamination of AN with PA and AN with 4-methoxy phenylacetylene (**Figure 79**), also agree with what observed in the case of the intramolecular hydroamination reaction of substituted 2-(2-propynyl)anilines. In fact, an activation Gibbs energy (Δ$G_{Nuc}^{\ddagger}$) of 7.8 kcal mol^{-1} was calculated for the transition state, corresponding to the nucleophilic attack of AN aggregates (stabilized by hydrogen bonding) to

PA, while a $\Delta G_{Nuc}{}^{\ddagger} = 6.2$ kcal mol^{-1} was found in the case of the nucleophilic attack of AN aggregates to 4-methoxy phenylacetylene. Therefore, these results suggest a polarization/activation of the C≡C coordinated to the gold surface by the *p*-methoxy group.
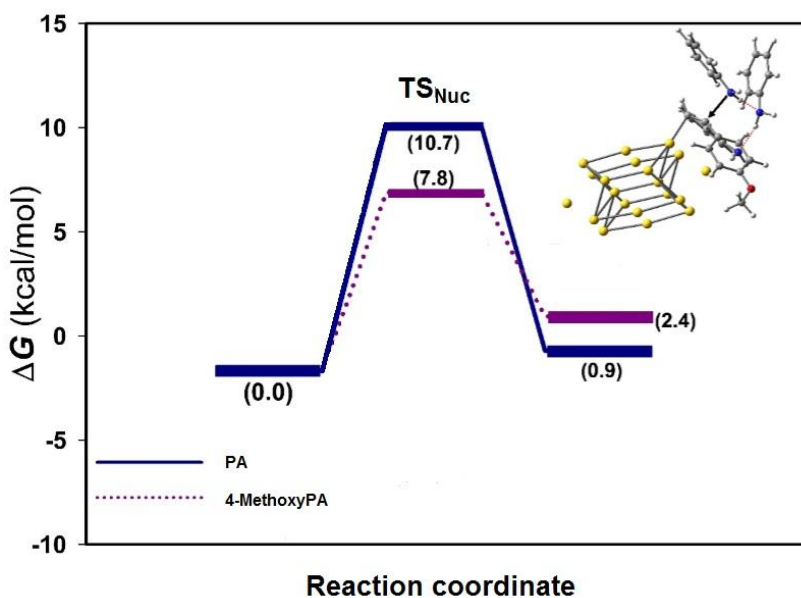
Figure 79: Gibbs energy profile for the nucleophilic attack of three aniline-assisted to the corresponding PA or 4-methoxy phenylacetylene, on Au$_{20}$ cluster.

This finding confirms the lower electrophilicity of Au(0) compared to Au(I) and suggest the relevance of the electronic properties of the alkyne on the overall reaction mechanism. In addition, an aliphatic substituent was also tested (entry **3**, **Table 12**). In this case the reaction was slower with

only 67% conversion in 3h; the (*R*)-2-hexyl-1,2,3,4-tetrahydroquinoline was almost the only product observed but a slight decrease in the enantioselectivity was observed (70% *ee*).

4.4: ENANTIOMERIC EXCESS MEASURED BY ^{1}H-NMR SPECTROSCOPY.

All the *ee* values given above were determined by HPLC analysis. An attempt to determine the enantiomeric excess was done using ^{1}H-NMR spectroscopy. (*R* or *S*)-1,1-Binaphthyl-2,2-diyl hydrogenphosphate as NMR chiral derivatizing agent (CDA) for the resolution of chiral secondary and tertiary amines was previously described in the literature.[155] This compound presents in fact a no signals in the 1-6 ppm region of the ^{1}H – NMR spectrum and is simply to use. In this study, (*R*)-1,1-Binaphthyl-2,2-diyl hydrogenphosphate **23** was added to the THQ **20** in CDCl$_3$ (molar ratio THQ:DCA = 1:0.8) and the mixture analyzed by ^{1}H-NMR. The addition of CDA to THQ causes a conversion of the two THQ enantiomers into diastereomeric complexes, thus allowing their recognition through NMR analysis (see experimental section). In **Table 13** it is reported the comparison between enantiomeric excesses obtained with ^{1}H-NMR and HPLC analysis, for the reactions reported in **Table 9**.

As it can be observed, the *ee* obtained with the ^{1}H NMR analysis were similar to those obtained by HPLC analysis, with differences of only 0-3 percentage points. Therefore, this method could be considered a valid

alternative to HPLC for the determination of the enantiomeric excess of the THQs.

Table 13: comparison between enantiomeric excesses obtained with ^{1}H-NMR and HPLC analysis.

Entry	^{1}H-NMR ee (%)[b]	HPLC ee (%)[c]
1	1	2
2	75	74
3	70	68
4	56	56
5	83	86
6	nd	74
7	79	76

[a] Reaction conditions: see Table 9. [b] Determined by ^{1}H-NMR analysis of reaction mixture using as (R)-1,1-Binaphthyl-2,2-diyl hydrogenphosphate CDA (CDCl$_3$, 25 °C). [c] Determined by HPLC analysis.

The formation of these diastereomeric complexes is not a quantitative process but rather an equilibrium reaction. The equilibrium constant K_a (**Eq. 9**) is usually referred to as a binding constant or association constant.

$$[THQ] + [CDA] \rightleftarrows [THQ \cdot CDA] \qquad \text{Eq. 8}$$

$$K_a = \frac{[THQ \cdot CDA]}{[THQ][CDA]} \qquad \text{Eq. 9}$$

The ^{1}H NMR patterns associated with the reaction in **Eq.8** depend on the K_a, concentration of CDA and rate of the reaction. If the equilibrium is fast with respect to NMR time scale, a time averaged spectrum of THQ (and/or CDA) and THQ·CDA complex is observed. In this case, any observed chemical shift is the weighted mole fraction between the free reagents and the 1:1 adduct (**Eq.10**, where δ_{obs} is the experimental chemical shift; δ_{THQ} is the chemical shift of a nucleus in THQ; $\delta_{THQ·CDA}$ is the chemical shift of a nucleus diagnostic of the THQ·CDA adduct; X_{THQ} is the mole fraction of THQ in the equilibrium mixture; $X_{THQ·CDA}$ is the mole fraction of THQ·CDA in the equilibrium mixture).[156]

$$\boldsymbol{\delta_{obs} = X_{THQ}\delta_{THQ} + X_{THQ·CDA}\delta_{THQ·CDA}}$$ Eq. 10

δ_{obs} is a linear function of $X_{THQ·CDA}$. By adding CDA to the solution, the reaction equilibrium is shifted towards the THQ·CDA adduct; $X_{THQ·CDA}$ increases and consequently also the chemical shift increases. The ^{1}H-NMR spectra (detail of the THQ enantiotopic proton Ha) for various molar ratios of THQ **20** and (*R*)-**23** is reported in **Figure 80**. In general, the addition of CDA to THQ yields a shift of the peak (compared to pure THQ) indicating the effective formation of the THQ·CDA adduct. The formation of two diastereomeric complexes was observed and the best separation was obtained for a molar ratio THQ:CDA of 1:0.8.
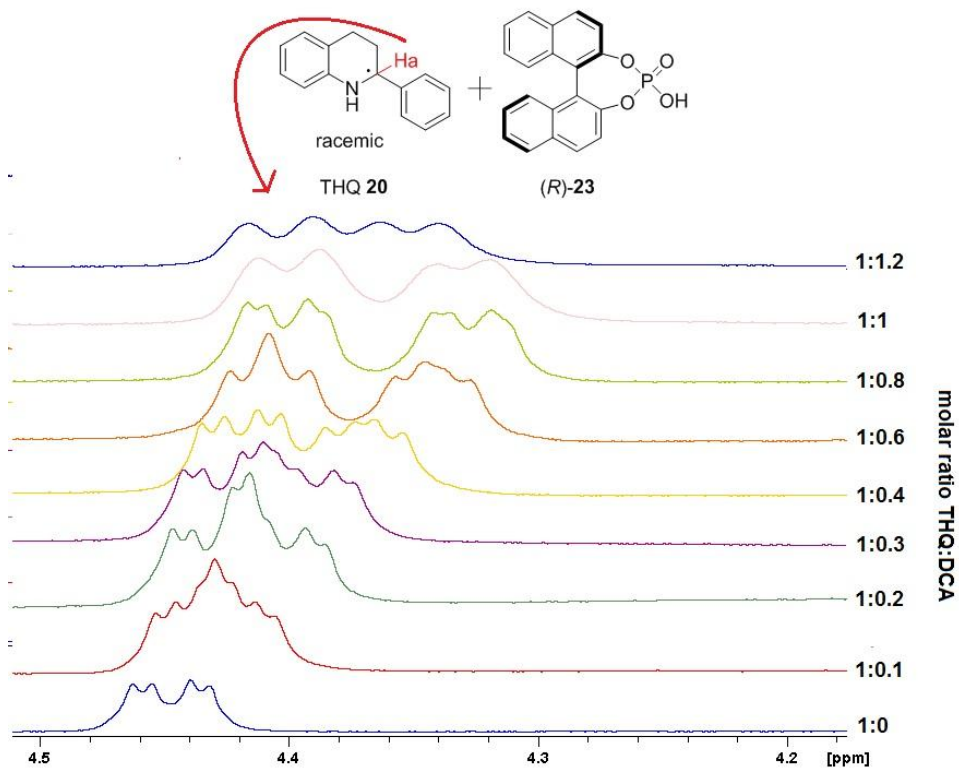
Figure 80: ^{1}H-NMR spectra at different molar ratio of the THQ 20 and (R)-23 mixture.

4.5: CONCLUDING REMARKS.

The heterogeneous gold catalyst AuNPs-TiO$_2$ was found for the first time active in the intramolecular hydroamination of 2-(2-propynyl)anilines followed by asymmetric transfer hydrogenation, to form THQs. In particular, AuNPs-TiO$_2$ combined to the Hantzsch ester and chiral phosphoric acid auxiliary ((R)-3,3'-Bis(9-phenanthryl)-1,1'-binaphthalene-2,2'-diyl hydrogen phosphate), showed excellent yields and

147

enantioselectivity in the ring closing reaction, leading to chiral substituted THQs. The lower electrophilicity of Au(0) compared to Au(I) results in lower regioselectivity for the ring closing reaction (indole *vs* quinoline structures). However, the electronic properties of the aromatic ring of PA can play an important role in controlling the regioselectivity of the nucleophilic attack of the nitrogen atom to the π-system of the alkyne. Moreover, AuNPs-TiO$_2$ exhibits, unlike the homogenous gold catalysts, good catalytic activity and enantioselectivity in solvents such as 2-MeTHF, paving the way to greener synthetic processes.

CHAPTER 5

....

AEROBIC OXIDATION AND OXIDATIVE ESTERIFICATION OF 5-HYDROXYMETHYL-2-FURFURAL CATALYZED BY AuNPs-sPBS

CHAPTER 5: AEROBIC OXIDATION AND OXIDATIVE ESTERIFICATION OF 5-HYDROXYMETHYL-2-FURFURAL CATALYZED BY AuNPs-sPBS

5.1: 5-HYDROXYMETHYL-2-FURFURAL (HMF)

Since the end of the 20th century, a strong interest for the development of new methodologies suitable for producing petrochemical intermediates from renewable sources has grown. 5-hydroxymethyl-2-furfural (HMF) plays a fundamental role in this framework; it is a platform molecule in Green Chemistry and in fact is a basic intermediate in the production of biofuels, solvents, polymers or biopolymers and pharmaceuticals compounds.[157–159] The synthesis of HMF was first reported in 1895 by Dull *et al.* who described the synthesis by heating inulin with an oxalic acid solution under pressure.[160] Since then a lot of synthetic procedure have been reported but the most used are based on dehydration of fructose. HMF can be also obtained from glucose (via isomerization to fructose), or from cellulose, starch or a glucose-based polysaccharides (for example glucan) (**Figure 81**).[161–165] Some drawbacks arise from the poor stability of this compound that cannot be stored for extended period of time since by-products like dimers and/or oligomers are readily formed when HMF contains small amounts of impurities.
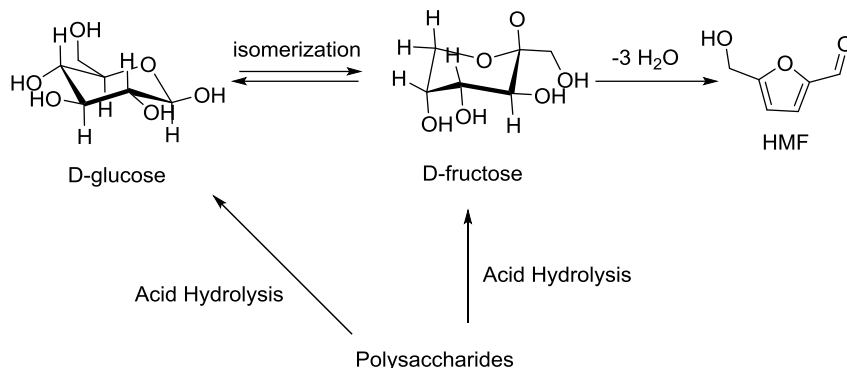
Figure 81: Synthetic ways to obtain HMF.

The hydroxyl and formyl functionalities of HMF allow synthetic transformation to target molecules, some of which shown in **Figure 82**.[164,165] The hydroxymethyl group exhibit the typical reactivity of a primary alcohol allowing the formation of esters, ethers and halides, while the formyl group can be involved in e.g. Wittig-type reactions, Baylis–Hillman reactions and aldol condensations. In addition, the furan ring can be transformed in acidic conditions into levulinic acid or other products by ring opening reactions. Levulinic acid is used as building blocks for various applications such as production of fuels, fuel additives, and polymers.[166] The selective reduction of the formyl group of HMF, performed in high yields using $NaBH_4$ as reducing agent or by hydrogenation with nickel, copper chromite, platinum oxide, cobalt oxide, molybdenum oxide or sodium amalgam catalysts[165] leads to the formation of 2,5-dihydroxymethylfuran (DHMF) used as diol in polyester synthesis and polyurethane foams.[167] The reduction of both formyl and

hydroxyl groups leads to 2,5-dimethylfuran (2,5 DMF), used as biofuel.[168] This process is well performed using carbon-supported copper/ruthenium catalysts or palladium catalysts.[164,165]
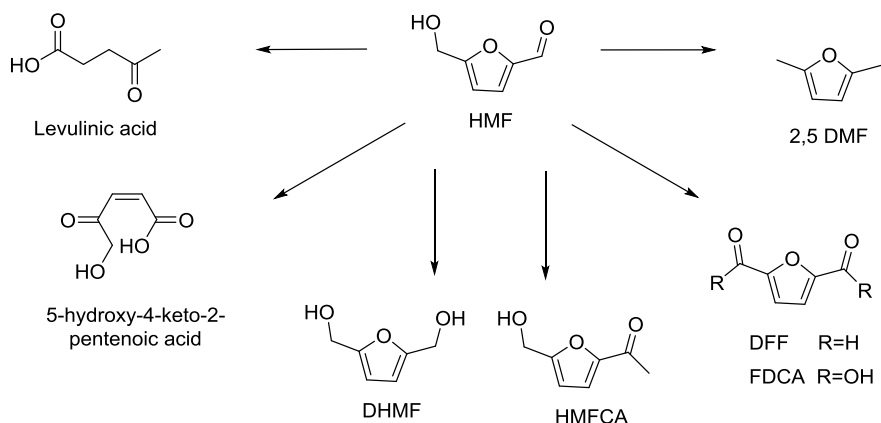
Figure 82: Transformation of HMF to other target molecules.

The oxidation of HMF is selectively carried out to form 2,5-diformylfuran (DFF), 5-hydroxymethyl-2-furancarboxylic acid (HMFCA) or 2,5-furandicarboxylic acid (FDCA). All this products are important building blocks for the industry as they can replace adipic acid, alkyldiols or terephthalic acid in polymer synthesis.[169]

Oxidation of HMF has been performed with a variety of metal catalysts, each one showing a specific selectivity. The selective oxidation of the formyl group to HMFCA was preliminary carried out using silver oxide or

a mixture of silver and copper(II) oxides under basic conditions.[164] More recently, heterogeneous gold catalysts have been employed with good results (see the following paragraph). More challenging is the selective oxidation of the hydroxymethyl group to form DFF; in fact, when the reaction is carried out with strong oxidants, oxidation of the aldehyde functionality to carboxylic acid functionality is preferred with respect to alcohol oxidation, to give FDCA as final product. To obtain the selective oxidation of the alcoholic functionality of HMF, different oxidants were tested such as chromium salts, HNO_3 and lead acetate;[164] more recently green methods, which make use of heterogeneous metal-based catalysts, have been proposed.[170] In particular, manganese, vanadium or copper-based catalysts are very promising in both homogeneous and heterogeneous conditions. Noble metals such as Pd, Pt, Ru and Au exhibit excellent catalytic activity under mild conditions.[171,172] In the next paragraph, oxidation reaction of HMF promoted by heterogeneous gold catalysts will be examined in detail.

5.2: OXIDATION OF HMF CATALYZED BY GOLD NANOPARTICLES

AuNPs catalysts have been widely explored in HMF oxidation;[164,171,172] in the most cases, FDCA is the final product. Few papers describe the selective formation of HMF to intermediate oxidation products. HMFCA is typically obtained under mild oxidation conditions. Gorbanev et al.[173] reported the formation of HMFCA in aerobic oxidation of HMF to FDCA in

basic aqueous solution at room temperature, using the AuNPs-TiO$_2$ catalyst. They observed a dependence of the reaction products (HMFCA and FDCA) on the amount of base and the applied O$_2$ pressure, noting that HMFCA is preferentially obtained, in quantities higher than FDCA, when applying low pressure of O$_2$ or low concentrations of base. Corma *et al.*[174] reported the aerobic oxidation of HMF in water using NaOH as base and the AuNPs-CeO$_2$ catalyst. They observed the formation of HMFCA as intermediate product that gradually is converted into FDCA product. In particular, at 65°C and 10 bar of air pressure, the concentration of HMFCA increases up to 100 mol% yield in 1h; after this reaction time, the concentration of HMFCA gradually decreases while that of FDCA increases (**Figure 83**). In particular, FDCA is not formed until all HMF is converted into HMFCA, indicating the slower reactivity of HMFCA compared to HMF. Davis *et al.*[175] investigated the oxidation of HMF in water by AuNPs-Carbon and AuNPs-TiO$_2$ catalysts using NaOH as base. A 92–93% selectivity towards HMFCA and 100% conversion of HMF were found when the reactions is carried out at room temperature with O$_2$ pressure of 7 bars.
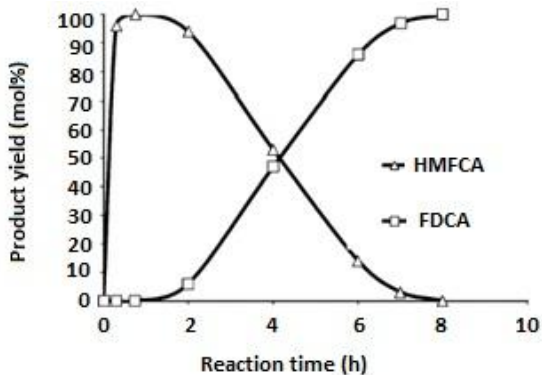
Figure 83: Kinetics for HMF oxidation at 65°C, 10 bar air pressure, in water, using Au-CeO$_2$ as catalyst.[169]

The selective formation of DFF with heterogeneous gold catalysts is less explored. An attempt to synthesize DFF from HMF or fructose was done using a bimetallic Au&Ru-NPs supported on reduced graphene oxide.[176] In this case, visible light was used to promote the reactions and DFF was obtained in 91% and 86% yield, starting from HMF or fructose respectively. The presence of DFF and the absence of HMFCA indicate that the reaction follows a different mechanical path (see the following paragraph for details). Lu *et al.*[177] reported that Au&Pd alloy-MnO$_2$ is active in the selective oxidation of HMF to DFF. The reaction at 90°C allowed to obtain the product with a selectivity >90% and a conversion into HMF of 76%.

As previously reported, the majority of publications regarding the use of heterogeneous gold catalysts in the HMF oxidation are focused on the

synthesis of FDCA[171,172] catalyzed AuNPs supported on metal oxides, in particular AuNPs-TiO$_2$ and AuNPs-CeO$_2$. Gorbanev et al.[173] reported the formation of FDCA in 71% yield at room temperature, using AuNPs-TiO$_2$ as catalyst in presence of 20 equiv. of NaOH. Cavani and co-worker tested a series of AuNPs-CeO$_2$ in the oxidation of HMF to FDCA.[178] In particular, AuNPs-CeO$_2$ is the best catalyst providing FDCA in 52% yield at 70°C, using 10 bar O$_2$ pressure and 4 equiv. of NaOH. Raising the temperature from 70 to 130 °C, the FDCA yield increased from 52% to 96%. Generally, monometallic gold catalysts require the addition of large amount of base and high oxygen pressure. To enhance the catalytic activity, bimetallic catalysts were exploited. Prati et al.[179] reported series of Au&Pd-C catalysts, with different metal ratios of the two metals, showing high activity in aerobic oxidation of HMF to FDCA. The bimetallic catalysts are more active than the monometallic gold catalysts, showing FDCA yields of 95% whereas only 36% yield was observed with the monometallic catalysts; moreover, the recycling experiments showed higher thermal stability of the bimetallic catalysts. Pasini et al.[180] reported that bimetallic Au&Cu-NPs supported on TiO$_2$ is efficient catalyst in HMF oxidation to FDCA; also in this case, the bimetallic catalyst showed superior activity and stability compared to monometallic AuNPs-TiO$_2$.

In a perspective of Green Chemistry, the use of high concentration of Brønsted bases is not sustainable; the research interests thus moved toward the development of base-free methodologies. The AuNPs catalysts were thus tested under base-free condition[181] at 20 bar of air,

110 °C for 2h. AuNPs-MgO is the most efficient catalyst leading to quantitative HMF conversion into FDCA (91% yield); in general the conversions and selectivity in FDCA strongly depend on the basicity of the support, in the order MgO > NiO > TiO$_2$ ≈ ZrO$_2$ ≈ CeO$_2$. Gupta et al.[182] reported oxidation of HMF to FDCA with the AuNPs-hydrotalcite (AuNPs-HT) catalyst in water; 99% yield into FDCA were reached at 95°C, using 50 mL/min oxygen flow as oxidant; the catalyst could be reused at least three times without significant loss of activity and selectivity.

5.2.1: OXIDATIVE ESTERIFICATION OF HMF CATALYZED BY GOLD NANOPARTICLES

Many research interests were devoted to the oxidative esterification of HMF to dialkyl esters of industrial value (**Figure 84**). In particular, furan-2,5-dimethylcarboxylate (FDMC) is applied in the production of poly(ethylene furanoate) (PEF) and poly(trimethylene furandicarboxylates) (PTF), that are valid alternatives to poly(ethylene terephthalate) (PET).
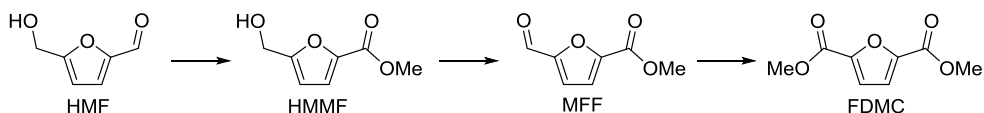
Figure 84: Oxidative esterification of HMF products.

Christensen *et al*[183] reported the first example of direct oxidative esterification of HMF to FDMC with a heterogeneous gold catalyst. The reaction was performed with AuNPs-TiO$_2$ at 130°C using MeOH as solvent and sodium methoxide as base at 4 bars of O$_2$ pressure. HMF was oxidatively esterified to FDMC with excellent yield (98%) in only 3h. Corma *et al.*[184] reported the first example of base free oxidative esterification of HMF to FDMC, using AuNPs-CeO$_2$; the reaction was performed in MeOH at 130°C with 10 bar O$_2$ and FDMC was quantitatively obtained in 5h. AuNPs-TiO$_2$, AuNPs-Fe$_2$O$_3$ and AuNPs-Carbon were also tested but AuNPs-CeO$_2$ resulted the most active; the authors proposed that the ceria support acts as an oxygen supplier to the system by releasing and adsorbing oxygen through a redox process involving the Ce^{4+}/Ce^{3+} redox couple. Attempts to catalyze oxidative esterification of HMF to FDMC were done using AuNPs-Zr(OH)$_4$, where part of the hydroxide groups was sulphated in order to obtain different sulphation degree on the final supports;[185,186] the effect of this different sulphation degree on the final supports, on the reactivity and selectivity of the reaction, was studied. Three different catalysts with 0%, 2% and 8% of sulphate groups on the final support were tested at 130°C with 3 bar O$_2$ pressure in base free conditions. The conversion of HMF was quantitative in 5h for all the investigated catalysts, but AuNPs-Zr(OH)$_4$ with 2% of sulphate groups showed the best selectivity, although only of 32%, toward FDMC.

5.3: MECHANISTIC HYPOTHESIS ON OXIDATION AND OXIDATIVE ESTERIFICATION OF HMF CATALYZED BY GOLD NANOPARTICLES

The reaction pathways in HMF oxidation over different AuNPs catalysts depend on the reaction medium and catalyst characteristics.[187] The mechanism can follow the two routes shown in **Figure 85**. In the first path, the formyl group of HMF is oxidized to a carboxylic group to form HMFCA; the subsequent selective oxidation of the hydroxymethyl group to formyl group produces 5-formyl-2-furancarboxylic acid (FFCA) and the definitive oxidation of FFCA yields FDCA. In the second path, the hydroxymethyl group is oxidized to formyl group of DFF. The selective oxidation of one formyl group produces a carboxylic group of FFCA; the further oxidation of the latter yields FDCA.
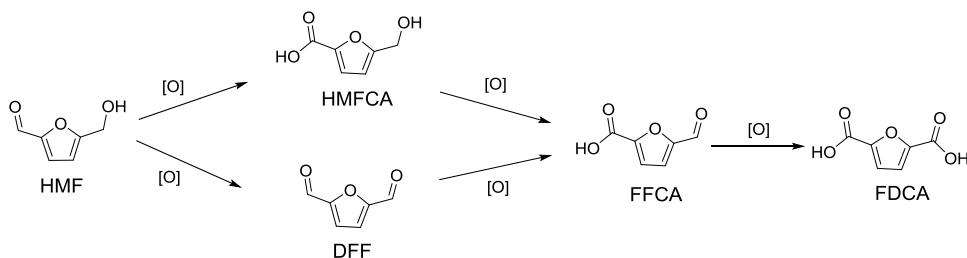
Figure 85: Mechanistic pathways for the oxidation of HMF.

In general, the gold catalysts follow, under basic conditions, the first path[174] since the oxidation of the hydroxymethyl group is slow compared

160

to the formyl group and HMFCA is thus favored. Moreover, the basic conditions favor HMFCA since the formyl group of HMF undergoes a rapid and reversible hydration leading to the hemiacetal intermediate, through the nucleophilic attack of the hydroxide anion (**Figure 86**). The following β-hydride elimination, facilitated by the hydroxide ions adsorbed on the gold surface, leads to the carboxylic acid.[136] Once FFCA is formed, it is converted to FDCA through the formation of a second hemiacetal intermediate (**Figure 86**).
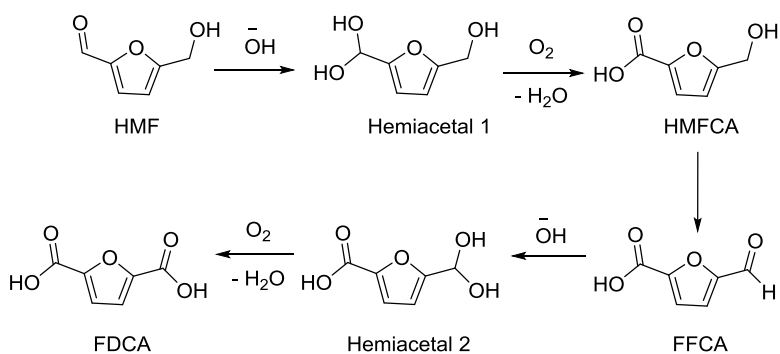
Figure 86: mechanistic pathway for the HMF oxidation via hemiacetal formation.

In the absence of a base, the catalyst characteristics could drive the reaction to different pathways. The AuNPs-HT catalyst[182] proceeds through the first reaction pathway because of the basic properties of the support and the hemiacetal intermediate is thus formed. In the presence of e.g. Au&Pd catalysts,[188] the reaction follows the second pathway

because the presence of Pd in the MNPs facilitates the oxidation of the alcoholic group, leading to the formation of DFF.

Corma and co-workers have proposed a possible pathway for the oxidative esterification of HMF catalyzed by AuNPs-CeO$_2$ (**Figure 87**).[184] Initially, HMF reacts with MeOH to form the hemiacetal **a**. At this point, the reaction can follow two different paths: the intermediate **a** can undergo either oxidation reaction to give **b** or reacts with another molecule of MeOH to form the acetal **f**. The intermediate **b**, also known as 5-hydroxymethyl methylfuroate (HMMF), is gradually oxidized, in the first path, into the monoester aldehyde **c,** known as methyl 5-formyl-2-furoate (MFF), which in turn is converted into **d**, after hemiacetalization. Most of the intermediate **d** is converted into the final product FDMC, while a small fraction can be transformed in the monoester acetal **e**, which is oxidized to FDMC. In the second path, **f** is oxidized into the acetal aldehyde **g**, which in turn is transformed into the hemiacetal **h**; this intermediate is then oxidized into **e** and finally converted into FDMC.
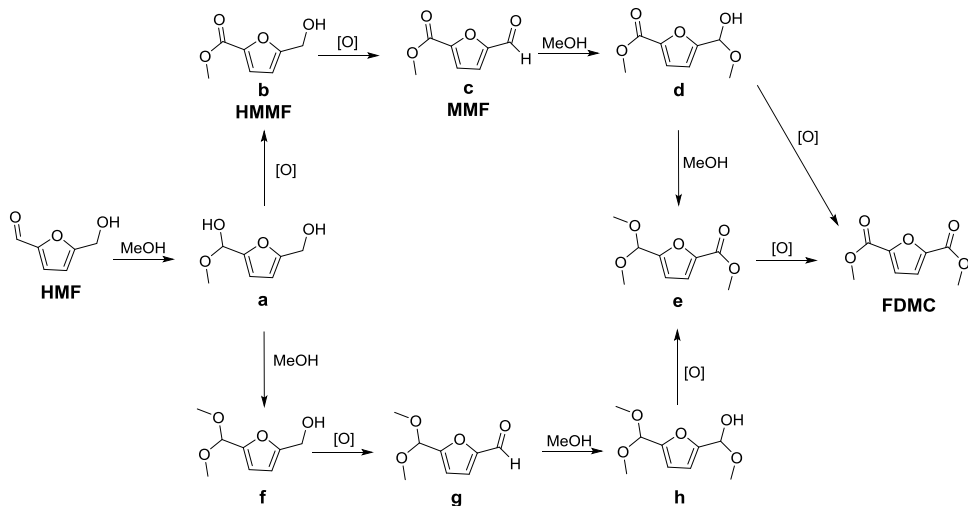
Figure 87: Mechanistic pathways for the oxidative esterification of HMF.

5.4: SELECTIVE OXIDATION OF HMF AND OXIDATIVE ESTERIFICATION OF HMF CATALYZED BY THE AuNPs-sPSB CATALYST

The majority of the works regarding the use of heterogeneous gold catalysts applied to the oxidation and oxidative esterification of HMF are based on metal oxide supports. As seen previously, AuNPs-sPSB is an efficient catalyst in different organic reactions.[86–89] In the light of these results, we tested AuNPs-sPSB in the oxidation of HMF and oxidative esterification of HMF, to investigate the role of the nanoporous polymeric matrix in these reactions.

5.4.1: THE AuNPs-sPBS CATALYST

The AuNPs-sPSB catalysts containing the polymeric support in the δ, β and ε crystalline phases were synthesized as previously described with a gold concentration of 2 *wt%* and characterized by wide angle x-rays diffraction (WAXD) analysis and transmission electron microscopy (TEM) images. In **Figure 88** the conventional transmission electron microscopy (CTEM) images are reported; it can be observed that the nanoparticles are homogeneously dispersed in the polymer matrix of each catalyst. In the **Figure 89**, the WAXD patterns for the δ, β and ε crystalline phase of AuNPs-sPSB catalysts are reported. The average size of AuNPs was determined by Scherrer equation[103] applied to the <111> reflections of crystalline gold.
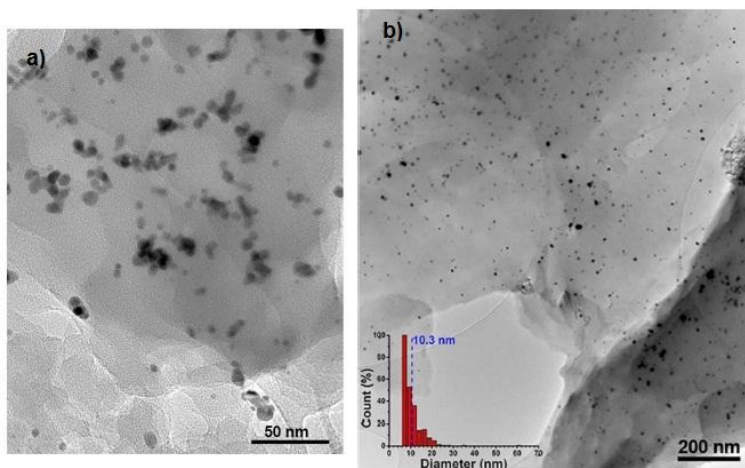
Figure 88: CTEM image of a) AuNPs-(δ)sPSB and b) AuNPs-(ε)sPSB.
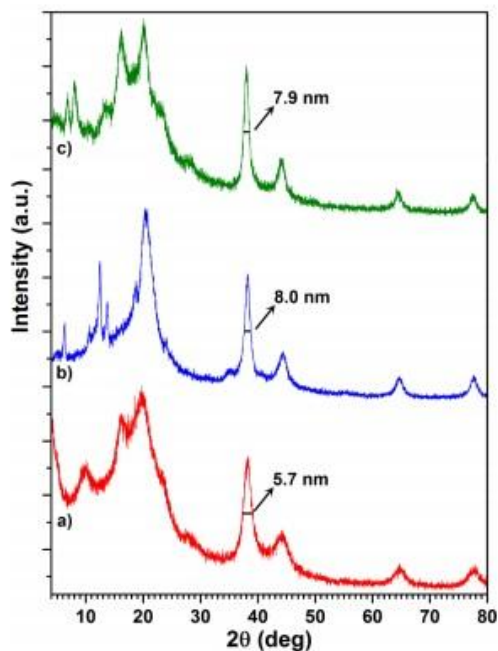
Figure 89: WAXD patterns of a) AuNPs-(δ)sPSB, b) AuNPs-(β)sPSB, c) AuNPs-(ε)sPSB. Greek letters indicate the crystalline form of sPSB. Dotted lines mark the reflections of *fcc* crystalline lattice planes of nanocrystalline gold.

5.4.2: OXIDATION OF HMF CATALYZED BY THE AuNPs-sPSB CATALYST

The HMF oxidation was initially studied carrying out the reaction in *N,N*-dimethylformamide (DMF), at 80°C, using an O_2 pressure of 1.5MPa, in presence of Cs_2CO_3 as base. The role of the polymer crystalline phase was preliminarily investigated (**Table 14**).

Table 14: Effect of the crystalline phase.
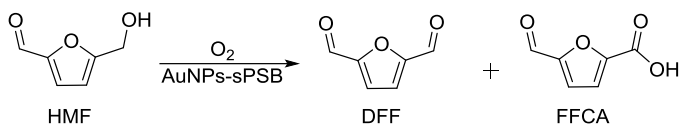
Entry[a]	Crystalline phase	Conv (mol%)[b]	Selectivity (mol%)[b]		TON[c]	TOF (h^{-1})[d]
			DFF	FFCA		
1	δ	47	16	84	12	0.7
2	β	24	25	75	6	0.4
3	ε	72	29	71	18	1.1

[a] Reaction conditions: hydrate HMF (0.127 mmol), AuNPs-sPSB ([Au]=2 wt%, molar ratio Au:HMF = 1:25), Cs_2CO_3 (0.127 mmol), DMF (2 mL), 16h at 80°, O_2 (1.5 MPa). [b] Determined by ^{1}H-NMR analysis of reaction mixture (anisole as external standard). [c] Overall turnover number (moles of reacted HMF/moles of Au). [d] Overall turnover frequency (TON/reaction time).

The AuNPs–(ε)sPSB catalyst provided in 16h the best conversion of HMF (compare entry **3** with entries **1**-**2**, **Table 14**); in all cases, DFF and FFCA are the main reaction products, where the latter is the most abundant. An important aspect to be considered is that the oxidation of the formyl group of DFF to FFCA proceeds via hemiacetal intermediate in presence of water. For this reason, the further tests reported in the following paragraphs were carried out in anhydrous solvents and using molecular sieves in the reaction medium to trap the water resulting from the alcohol oxidation.

5.4.2.1: EFEECT OF THE TEMPERATURE

Table 15: Effect of the temperature.

Entry[a]	T (°C)	Conv (mol%)[b]	Selectivity (mol%)[b]		TON[c]	TOF (h^{-1})[d]
			DFF	FFCA		
1	40	17	80	20	4	0.3
2	50	32	73	27	8	0.5
3	60	47	74	26	12	0.7
4	70	72	67	33	18	1.1
5	80	78	80	20	20	1.2
6	90	75	60	40	19	1.2
7	100	84	26	74	25	1.6
8	110	78	5	95	20	1.2

[a] Reaction conditions: hydrate HMF (0.127 mmol), AuNPs-(ε)sPSB ([Au]=2 wt%, molar ratio Au:HMF = 1:25), Cs$_2$CO$_3$ (0.127 mmol), DMF (2 mL), 16h, O$_2$ (1.5 MPa), molecular sieves (~50mg). [b] Determined by ^{1}H-NMR analysis of reaction mixture (anisole as external standard). [c] Overall turnover number (moles of reacted HMF/moles of Au). [d] Overall turnover frequency (TON/reaction time).

The effect of the temperature on the HMF oxidation reaction was tested in the range of 40 - 110°C (**Table 15**).

When the reaction temperature is raised, the HMF conversion increases up to reach the quantitative conversion at 100°C (entry **7**, **Table 15**). In the absence of water, the selectivity toward DFF increased to 73-80% in the range of temperature 40-80°C (entries **1**-**5**, **Table 15**). In particular, the best conversion and selectivity into DFF were obtained (entry **5**, **Table 15**) at 80°C while at higher temperature, e.g. 90-110°C, the selectivity into DFF decreased drastically in favor of FFCA (entries **6**-**8**, **Table 15**). The best selectivity in FFCA was obtained at 110°C (entry **8**, **Table 15**).

5.4.2.2: EFFECT OF THE BASE

The concentration of base in the reaction solution was investigated as an important reaction parameter; the results are shown in **Table 16**.

The tested bases are all less active than Cs_2CO_3 (compares entry **1** with entries **2**-**5**, **Table 16**); for this reason, the latter was considered the optimal external base and was used in the following catalytic runs.

Table 16: Effect of the different bases.

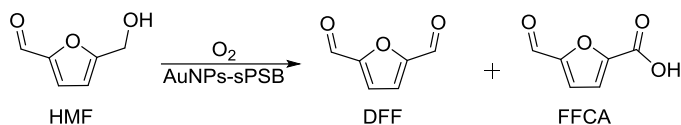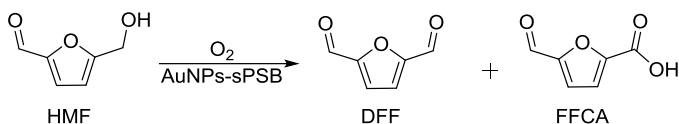| Entry[a]	Base	Conv (mol%)[b]	Selectivity (mol%)[b]		TON[c]	TOF (h^{-1})[d]
			DFF	FFCA		
1	Cs$_2$CO$_3$	47	74	26	12	0.7
2	KOH	28	78	22	7	0.4
3	NaOH	28	78	22	7	0.4
4	Na$_2$CO$_3$	23	87	13	6	0.4
5	K$_2$CO$_3$	32	78	22	8	0.5

[a] Reaction conditions: hydrate HMF (0.127 mmol), AuNPs-(ε)sPSB ([Au]=2 wt%, molar ratio Au:HMF = 1:25), base (0.127 mmol), DMF (2 mL), 16h at 60°C, O$_2$ (1.5 MPa), molecular sieves (~50mg). [b] Determined by ^{1}H-NMR analysis of reaction mixture (anisole as external standard). [c] Overall turnover number (moles of reacted HMF/moles of Au). [d] Overall turnover frequency (TON/reaction time).

Under the optimized condition of temperature for DFF formation (80°C), the amount of this base was investigated (**Table 17**).

Although the catalyst shows a modest activity even in the absence of a base (entry **4**, **Table 17**) the best results were obtained using one equiv. of Cs$_2$CO$_3$ (entry **1**, **Table 17**); when the concentration of this base is

increased the HMF conversion increases, whereas the selectivity changes in favor of FFCA (compares entry **1** with entries **2**-**3**, **Table 17**).

Table 17: Effect of the amount of base used.

Entry[a]	Equivalent of base	Conv (mol%)[b]	Selectivity (mol%)[b]		TON[c]	TOF (h^{-1})[d]
			DFF	FFCA		
1	1	78	80	20	20	1.2
2	2	>99	40	60	25	1.6
3	4	>99	18	82	25	1.6
4	-	32	77	23	8	0.5

[a] Reaction conditions: hydrate HMF (0.127 mmol), AuNPs-(ε)sPSB ([Au]=2 wt%, molar ratio Au:HMF = 1:25), Cs_2CO_3, DMF (2 mL), 16h at 80°C, O_2 (1.5 MPa), molecular sieves (~50mg). [b] Determined by ^{1}H-NMR analysis of reaction mixture (anisole as external standard). [c] Overall turnover number (moles of reacted HMF/moles of Au). [d] Overall turnover frequency (TON/reaction time).

5.4.2.3: EFFECT OF THE OXIGEN PRESSURE

Table 18: Effect of the oxygen pressure.

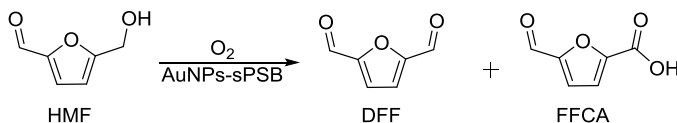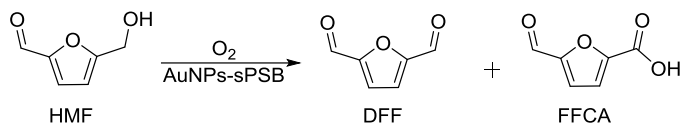| Entry[a]	P_{O_2} (MPa)	Conv (mol%)[b]	Selectivity (mol%)[b]		TON[c]	TOF (h^{-1})[d]
			DFF	FFCA		
1	0.1	54	56	44	14	0.8
2	1.0	67	64	36	17	1.1
3	1.5	78	80	20	20	1.2
4	2.0	88	72	28	22	1.4
5	2.5	83	68	32	23	1.5
6	3.0	94	70	30	24	1.5
7	3.5	93	56	44	23	1.5

[a] Reaction conditions: hydrate HMF (0.127 mmol), AuNPs-(ε)sPSB ([Au]=2 wt%, molar ratio Au:HMF = 1:25), Cs_2CO_3 (0.127 mmol), DMF (2 mL), 16h at 80°C, O_2, molecular sieves (~50mg). [b] Determined by ^{1}H-NMR analysis of reaction mixture (anisole as external standard). [c] Overall turnover number (moles of reacted HMF/moles of Au). [d] Overall turnover frequency (TON/reaction time).

The oxygen pressure was screened for determining the optimal reaction conditions (**Table 18**).

When the oxygen pressure was increased from 0.1 to 1.5 MPa an increment in DFF selectivity was observed (entries **1**-**3**, **Table 18**); a further increase of the O_2 pressure resulted into an increase of the HMF conversion but into a shift of selectivity toward FFCA (entries **4**-**7**, **Table 18**). The best selectivity value for DFF was obtained at O_2 pressure of 1.5 MPa (entries **3**, **Table 18**).

5.4.2.4: EFFECT OF THE POLYMERIC SUPPORT

The activity and selectivity of the AuNPs-(ε)sPSB catalyst were compared with commercial gold catalysts at 80°C and 110 °C; the main results are summarized in **Table 19**.

The AuNPs-(ε)sPSB catalyst allowed obtaining high selectivity in DFF and FFCA at 80°C and 110°C respectively (entries **1**-**2**, **Table 19**). In particular, this is the only catalyst that produced predominantly DFF (compare entry **1** with entries **3**, **5** of **Table 19**) and provided the highest chemoselectivity for FFCA, without FDCA formation (compare entry **2** with entries **4**, **6** of **Table 19**).
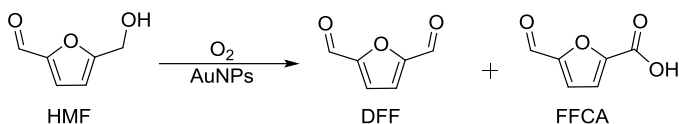
Entry[a]	Catalyst	T (°C)	Conv (mol%)[b]	Selectivity (mol%)[b]		TON[c]	TOF (h^{-1})[d]
				DFF	FFCA		
1	AuNPs-(ε)sPSB	80	78	80	20	20	1.2
2	AuNPs-(ε)sPSB	110	78	5	95	20	1.2
3	AuNPs-CB	80	58	9	91	14	0.9
4[e]	AuNPs-CB	110	65	23	71	16	1.0
5	AuNPs-TiO$_2$	80	59	23	77	15	0.9
6[f]	AuNPs-TiO$_2$	110	75	<1	69	19	1.2

[a] Reaction conditions: hydrate HMF (0.127 mmol), catalyst (molar ratio Au:HMF = 1:25), Cs$_2$CO$_3$ (0.127 mmol), DMF (2 mL), 16h, O$_2$ (1.5 MPa), molecular sieves (~50mg). [b] Determined by ^{1}H-NMR analysis of reaction mixture (anisole as external standard). [c] Overall turnover number (moles of reacted HMF/moles of Au). [d] Overall turnover frequency (TON/reaction time). [e] FDCA (yield=4.0mol%; selectivity=6%). [f] FDCA (yield=7.9 mol%; selectivity=22 %).

The high selectivity of AuNPs-(ε)sPSB for DFF at low temperature has been attributed to the hydrophobic nature of the polymer matrix, which makes difficult the diffusion of water (resulting from the alcohol oxidation) to the gold catalyst, hampering the formation of the hemiacetal species. At higher temperature, FFCA was rapidly formed

because of the enhanced reactivity of water resulting from the first oxidation step.

5.4.2.5: EFFECT OF THE SOLVENT

Table 20: Effect of the solvent.
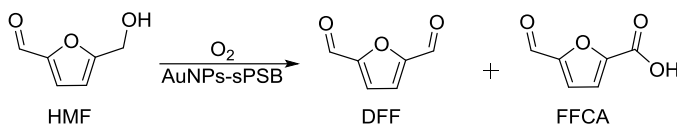
Entry[a]	Solvent	T (°C)	Conv (mol%)[b]	Selectivity (mol%)[b]		TON[c]	TOF (h^{-1})[d]
				DFF	FFCA		
1	DMF	80	78	80	20	20	1.2
2	DMF	110	78	5	95	20	1.2
3	DMA	80	65	78	22	16	1.0
4	DMA	110	>99	-	>99	25	1.6

[a] Reaction conditions: hydrate HMF (0.127 mmol), AuNPs-(ε)sPSB ([Au]=2 wt%, molar ratio Au:HMF = 1:25), Cs_2CO_3 (0.127 mmol), solvent (2 mL), 16h, O_2 (1.5 MPa), molecular sieves (~50mg). [b] Determined by ^{1}H-NMR analysis of reaction mixture (anisole as external standard). [c] Overall turnover number (moles of reacted HMF/moles of Au). [d] Overall turnover frequency (TON/reaction time).

DMF and *N,N*-dimethylacetamide (DMA) were tested as solvent. The performance of AuNPs-(ε)sPSB does not much depend on the nature of the solvent (**Table 20**). Indeed, it can be observed that a quantitative conversion of HMF into FFCA was obtained at 110°C using DMA (entry **4**, **Table 20**).

5.4.2.6: REUSABILITY OF AuNPs-(ε)sPSB

Under the optimized reaction conditions for the DFF formation, the reusability of AuNPs-(ε)sPSB was tested. The catalyst was reused for at least four runs without observing deactivation or leaching of AuNPs, since the conversion of HMF remained very high; disappointingly the selectivity changed progressively toward the FFCA formation (**Table 21**).

To understand this change in selectivity, WAXD analysis was performed on the catalyst recovered at the end of the catalytic run. In **Figure 90**, the pattern of reflections due to crystalline Cs_2CO_3 entrapped in the polymer matrix was detected; this suggests that there is an increase of the Cs_2CO_3/Au molar ratio in the recycling tests determining the observed change in selectivity described in the literature and in our study at variance of the base concentration. Actually, the data of **Table 17** showed that the increase of external base concentration yields FDCA as favored product.

Table 21: Recycling test.
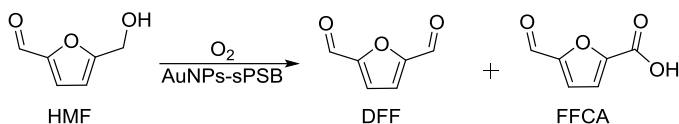
Entry[a]	Conv (mol%)[b]	Selectivity (mol%)[b]	
		DFF	FFCA
1	86	63	37
2	83	20	80
3	86	17	83

[a] Reaction conditions: hydrate HMF (0.127 mmol), AuNPs-(ε)sPSB ([Au]=2 wt%, molar ratio Au:HMF = 1:25), Cs₂CO₃ (0.127 mmol), DMF (2 mL), 16h, 80°C, O₂ (1.5 MPa), molecular sieves (~50mg). [b] Determined by ¹H-NMR analysis of reaction mixture (anisole as external standard). [c] Overall turnover number (moles of reacted HMF/moles of Au). [d] Overall turnover frequency (TON/reaction time).


Figure 90: WAXD pattern of AuNPs-sPSB catalyst after the 4th catalytic tests.

5.4.3: OXIDATIVE ESTERIFICATION OF HMF CATALYZED BY AuNPs-sPSB CATALYST

The oxidative esterification of HMF to FDMC, was investigated using AuNPs-(ε)sPSB as catalyst, Cs_2CO_3 as base and 1.5 MPa of oxygen pressure (**Table 22**).

When the reaction was carried out in MeOH at 25°C, HMMF was obtained in high yield and selectivity (entry **1**, **Table 22**) suggesting that, at this temperature, the hydroxymethyl group of HMMF was not oxidized. The increase of temperature to 70°C led to the equimolar mixture of HMMF and FDMC (entry **2**, **Table 22**) as a result of the increased oxidation rate of the hydroxymethyl group. However, the increase of temperature to 110°C resulted in a lower catalytic activity (entry **3**,**Table 22**). To improve the swelling of the polymeric support and allow higher mobility and diffusion rate of the reactants toward the catalytic sites, the addition of co-solvents was investigated. The addition of DMF to MeOH led to the formation of HMMF in high yield and high selectivity at 25°C (compare entry **4** with entry **1** of **Table 22**). Increasing the reaction temperature, only moderate conversions of HMF were obtained (entries **5**-**6**, **Table 22**); surprisingly a conversion of the crystalline phase of the polymer support from the porous ε to the not permeable β crystalline phase was monitored under this reaction condition (**b**, **Figure 91**).

Table 22: Oxidative Esterification of HMF catalyzed by AuNPs-(ε)sPSB

Entry [a]	Solvent	T (°C)	Conv (mol%)[b]	Selectivity (mol %)[b]		TON[c]	TOF (h^{-1})[d]
				HMMF	FDMC		
1	MeOH	25	>99	78	22	25	1.6
2	MeOH	70	>99	56	44	25	1.6
3	MeOH	110	33	51	49	8	0.5
4	DMF/MeOH 4:1	25	86	96	4	21	1.3
5	DMF/MeOH 4:1	70	44	76	24	11	0.7
6	DMF/MeOH 4:1	110	48	49	51	12	0.7
7	DMA/MeOH 4:1	25	35	64	36	9	0.5
8	DMA/MeOH 4:1	70	68	40	60	17	1.1
9	DMA/MeOH 4:1	110	89	10	90	22	1.4
10[e]	DMA/MeOH 4:1	110	>99	-	>99	25.0	5.0

[a] Reaction conditions: hydrate HMF (0.127 mmol), AuNPs-(ε)sPSB ([Au]=2 wt%, molar ratio Au:HMF = 1:25), Cs$_2$CO$_3$ (0.127 mmol), solvent (2.5 mL), 16h, O$_2$ (1.5 MPa), molecular sieves (~50mg). [b] Determined by ^{1}H-NMR analysis of reaction mixture (anisole as external standard). [c] Overall turnover number (moles of reacted HMF/moles of Au). [d] Overall turnover frequency (TON/reaction time). [e] 3.5 MPa O$_2$, reaction time 5h.
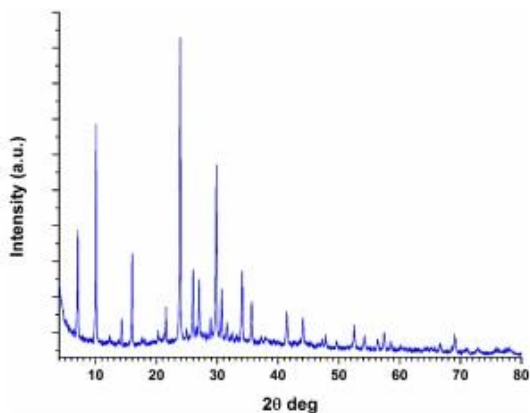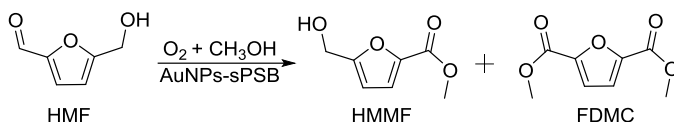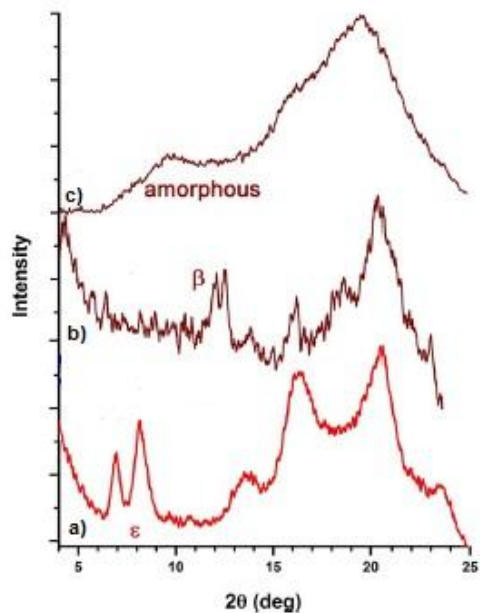
Figure 91: WAXD patterns of the AuNPs–sPSB catalyst a) before catalytic test, b) after catalytic tests in DMF at 110°C, c), after catalytic tests in DMA at 110°C.

Similarly, when a mixture of DMA and MeOH was used, moderate conversions were obtained at low reaction temperatures (entry **7**-**8**, **Table 22**); when the temperature was increased to 110°C the selective formation of FDMC was obtained (entry **9**, **Table 22**). The presence of DMA at high temperature resulted in the amorphization of the polymer matrix (**c**, **Figure 91**) allowing to obtain FDMC in high yield and selectivity. Finally, the increase of the oxygen pressure to 3.5MPa produced selectively FDMC in shorter reaction time (entry **10**, **Table 22**).

5.4.3.1: THE ROLE OF THE SUPPORT

Table 23: Effect of the support

$$\text{HMF} \xrightarrow[\text{AuNPs}]{O_2 + CH_3OH} \text{HMMF} + \text{FDMC}$$

Entry[a]	Catalyst	Solvent	T (°C)	Conv (mol%)[b]	Selectivity (mol%)[b] HMMF	FDMC	TON[c]	TOF (h⁻¹)[d]
1	AuNPs-(ε)sPSB	DMF/MeOH 4:1	25	86	96	4	21	1.3
2	AuNPs-(ε)sPSB	DMA/MeOH 4:1	110	89	10	90	11	0.7
3	AuNPs-CB	DMF/MeOH 4:1	25	0	-	-	0	0
4	AuNPs-CB	DMA/MeOH 4:1	110	40	19	52	10	06
5	AuNPs-TiO₂	DMF/MeOH 4:1	25	33	67	33	8	0.5
6	AuNPs-TiO₂	DMA/MeOH 4:1	110	55	21	45	14	0.9

[a] Reaction conditions: hydrate HMF (0.127 mmol), catalyst (molar ratio Au:HMF = 1:25), Cs_2CO_3 (0.127 mmol), solvent (2.5 mL), 16h, O_2 (1.5 MPa), molecular sieves (~50mg). [b] Determined by ^{1}H-NMR analysis of reaction mixture (anisole as external standard). [c] Overall turnover number (moles of reacted HMF/moles of Au). [d] Overall turnover frequency (TON/reaction time).

The role of the support was investigated by comparing the performances of AuNPs-(ε)sPSB with those of commercial gold catalysts.

AuNPs-(ε)sPSB provided the best selectivity in HMMF at 25°C (compare entry **1** with entries **3**, **5** of **Table 23**) whereas the synthesis of FDMC was obtained in elevated conversion and selectivity at 110°C (compare entry **2** with entries **4**, **6** of **Table 23**). This confirms our previous suggestion that the polymer support acts as a conveyor and concentrator of reactants towards the catalytic sites.

5.4.4: OXIDATION OF HMF IN WATER

The possibility of carrying out selective HMF oxidation to FDCA in green solvents like water, with the AuNPs-(ε)sPSB catalyst, was also investigated; the results are reported in **Table 24** and **Table 25**.

At 100°C and 3.5 MPa of oxygen pressure (entry **1**, **Table 24**) the selectivity of AuNPs-(ε)sPSB is scarce as well as after the addition of DMA in the reaction mixture (entry **2**, **Table 24**).

Table 24: Oxidation of HMF in water
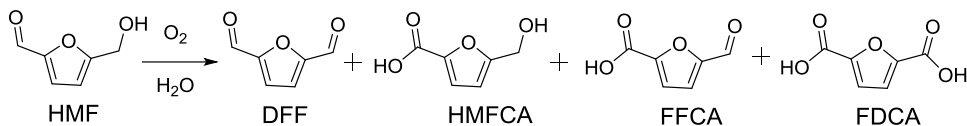
Entry [a]	Solvent	P_{O_2} (MPa)	Conv (mol%)[b]	Selectivity (mol%)[b]				TON[c]	TOF (h^{-1})[d]
				DFF	HMFCA	FFCA	FDCA		
1	H_2O	3.5	74	7	40	46	7	18	1.2
2	H_2O/DMA 4:1	3.5	83	5	42	34	19	21	1.3

[a] Reaction conditions: hydrate HMF (0.127 mmol), AuNPs-(ε)sPSB ([Au]=2 wt%, molar ratio Au:HMF = 1:25), Cs_2CO_3 (0.127 mmol), solvent (3 mL), 100°C, 16h, O_2. [b] Determined by ^{1}H-NMR analysis of reaction mixture (anisole as external standard). [c] Overall turnover number (moles of reacted HMF/moles of Au). [d] Overall turnover frequency (TON/reaction time).
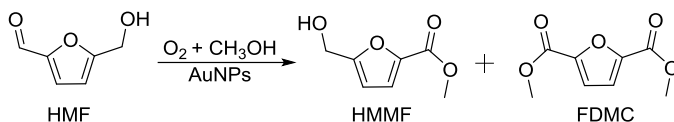
The further addition of MeOH and the increase of the reaction temperature to 110°C, led to a complete conversion of HMF and selectivity in FDCA of 77% in 16h (entry **2**, **Table 25**); extending the reaction time to 24h led to the selective formation of the FDCA (entry **3**, **Table 25**). Using KOH as base produced the selective formation of FDCA in shorter reaction time (entry **4**, **Table 25**). Both H_2O and MeOH compete for the nucleophilic attack to the formyl group of the HMF. The polymer matrix favors the latter due to its hydrophobic nature and oxidation to FDMC mainly occurs. The last step is the base-catalyzed hydrolysis of FDMC to give the final product FDCA.

Table 25: Oxidative Esterification of HMF in water

Entry [a]	Solvent	P_{O_2} (MPa)	Conv (mol%) [b]	Selectivity (mol)%[b]				TON [c]	TOF (h^{-1})[d]
				FFCA	FDCA	MFCA	FDMC		
1[e][f]	H₂O/DMA/ CH₃OH 1:4:1	1.5	78	32	20	38	10	20	1.2
2	H₂O/DMA/ CH₃OH 1:4:1	1.5	>99	10	77	6	7	25	1.6
3[e]	H₂O/DMA/ CH₃OH 1:4:1	1.5	>99	-	>99	-	-	25	1.6
4[g]	H₂O/DMA/ CH₃OH 1:4:1	1.5	>99	-	>99	-	-	25	1.6

[a] Reaction conditions: hydrate HMF (0.127 mmol), AuNPs-(ε)sPSB ([Au]=2 wt%, molar ratio Au:HMF = 1:25), Cs₂CO₃ (0.127 mmol), solvent (3 mL), 110°C, 16h, O₂. [b] Determined by ¹H-NMR analysis of reaction mixture (anisole as external standard). [c] Overall turnover number (moles of reacted HMF/moles of Au). [d] Overall turnover frequency (TON/reaction time). [e] Reaction time 24h. [f] Reaction temperature 90°C. [g] KOH as a base (0.159 mmol).

5.4.5: MECHANISTIC INSITE OF THE OXIDATION AND OXIDATIVE ESTERIFICATION OF HMF CATALYZED BY AuNPs-sPSB

The reaction pathways for the oxidation and oxidative esterification of HMF over AuNPs-sPSB catalyst are reported in **Figure 92**. The course of reaction depends strongly on the crystalline phase of the polymeric support and the reaction conditions applied. Concerning the oxidation process, the oxidation of the hydroxymethyl group occurs under mild conditions of temperature and external base concentration, leading to the formation of DFF (reaction pathway **a** of **Figure 92**). Under more drastic conditions, a subsequent oxidation of the formyl group to carboxylic function via the *gem*-diol intermediate occurs, leading to the formation of FFCA (reaction pathway **a** of **Figure 92**). In presence of water, the oxidation of the formyl group proceeds faster than that of the alcoholic one, leading to HMFCA and then to FFCA (reaction pathway **b** of **Figure 92**). When MeOH is used as solvent, HMMF is formed as in the oxidative esterification process; this suggests that the reaction occurs via hemiacetal through the pathway **c** of **Figure 92**. Using a mixture of DMA and water as solvent, a distribution of oxidation products (DFF, HMMF, FFCA and FDCA) is observed indicating that the reaction proceeds through both pathways **a** and **b,** and then path **d** of **Figure 92**. When methanol is added to the DMA/water mixture, the distribution of products (FFCA, FDCA, MFCA and FDMC) changes indicating that the reaction proceeds through the pathways **c** and **e** of **Figure 92**.
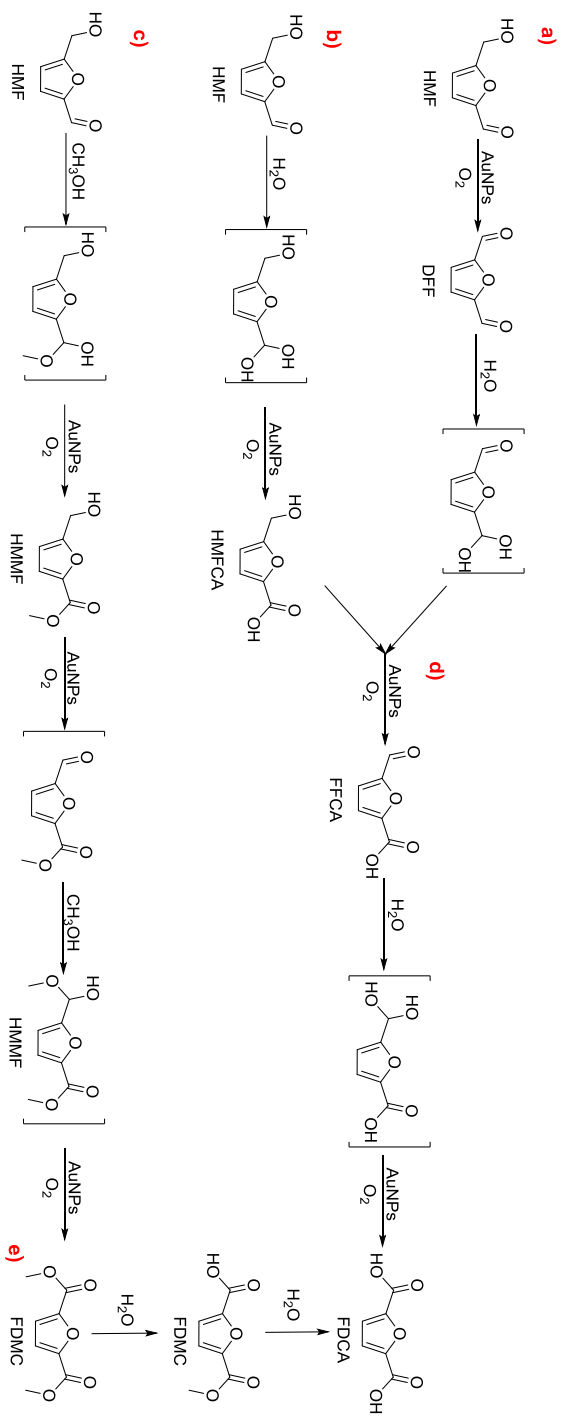
Figure 92: possible mechanistic pathways for the oxidation and oxidative esterification of HMF catalyzed by AuNPs-sPSB

185

5.5: CONCLUDING REMARKS.

The AuNPs–(ε)sPSB catalyst is very active and selective in the oxidation and oxidative esterification of HMF. In particular, using a precise control of the reaction conditions, the polymer matrix allows fine tuning of the reactivity of HMF. The selective oxidation of HMF into DFF was performed in moderate reaction conditions (80°C, 1 eq. base, 1.5 MPa O_2 pressure), while under more severe conditions (110°C or base excess) FFCA is obtained in high yield and selectivity. An important role was played by water, resulting from the first oxidation step to DFF, which favors the formation of FFCA through the *gem*-diol intermediate. In the oxidative esterification of HMF the selective formation of HMMF was achieved at room temperature using MeOH or a mixture of DMF/MeOH as solvent. At high temperatures, the choice of the solvent was fundamental in determining the phase of the polymer matrix and the corresponding activity and selectivity. In particular, DMA allowed the formation of FDMC in high yield and selectivity because of the amorphization of the polymer phase. The selective oxidation of HMF to FDCA was achieved by oxidative esterification of HMF to FDMC performed in a mixture of H_2O/ DMA /MeOH followed by base-catalyzed hydrolysis of the FDMC.

CONCLUDING REMARKS

In this PhD project, the AuNPs-sPSB catalyst has been successfully applied in the intermolecular hydroamination of PAs with ANs, as well as in the oxidation and oxidative esterification of HMF. In all investigated cases the desired products were obtained in high yields and with excellent selectivity since the crystalline phase of the polymeric matrix allows controlling the accessibility of the reactants to the catalytic sites and to tune the reactivity of the AuNPs.

The intermolecular hydroamination reaction of ANs and PAs was performed under mild and neat conditions; in all the cases, the corresponding ketimine was selectively obtained in the thermodynamic favored *E*-configuration. The kinetic investigation showed that the hydroamination was of first-order respect to both AN and PA, suggesting fast diffusion of the aromatic reactants through the porous phase of the polymer support. A remarkable feature of this reaction is that the compact β crystalline phase of the native catalyst crystallizes into the porous δ phase after treatment with the aromatic reagents, suggesting that the swelling in these solvents/reagents in the course of the reaction induces crystallization of the support in the porous phase of interest. The activation parameters were calculated from the Eyring Polanyi plot and found of $\Delta H^{\ddagger}$ = 13.4±1.8 kcal mol^{-1} and $\Delta S^{\ddagger}$ = -0.04±0.04 kcal mol^{-1} K^{-1}. The kinetic study of hydroamination of PA with AN-d_2 surprisingly resulted of first order with respect to the alkyne and of second order with

respect to AN-d_2 suggesting a different reaction pathway for this reagents; no kinetic isotopic effect was observed with AN-d_2.

DFT modelling was thus carried out on the hydroamination reaction between AN and PA to shed light on the reaction mechanism. A new reaction pathway was proposed in which the alkyne is coordinated onto the surface of the catalyst where it is activated for the nucleophilic attack of AN. Moreover, the formation of AN aggregates increases the nucleophilicity of AN leading to a lower energetic barrier in this reaction step. The lack of isotopic effect rules out that the N-H activation is in the rate determining step as proposed by analogy with the O-H activation in aerobic oxidation of alcohols.[136] The agreement between the calculated and experimental energetic barrier supports that the proton shift from the anilinium cation to the Cβ carbon of the enamine intermediate, coordinated at the surface of the AuNPs, is the rate determined step; this reaction is driven by one more AN molecule interacting with the coordinated substrate via hydrogen bonding.

In oxidation and oxidative esterification of HMF catalyzed by AuNPs-sPSB a precise control of the conditions allowed a fine tuning of the reactivity of HMF, leading to different products. In particular, the HMF oxidation under moderate conditions (80°C, 1 eq. base) produces selectively DFF while FFCA is the main reaction product under more severe conditions (110°C or base excess). The choice of the solvent is a critical reaction parameter. In MeOH or in a mixture of DMF/MeOH, HMMF is produced whereas the selective formation of FDMC was achieved in DMA. These

outcomes were attributed to a change of the crystalline phase of the polymer support by solvent annealing. Moreover, the selective oxidation of HMF to FDCA was achieved by oxidative esterification of HMF to FDMC followed by the base-catalyzed hydrolysis of FDMC. The porous ε crystalline phase of the support showed the best catalytic activity in HMF oxidation, followed by the δ phase; the compact β crystalline phase provided the worst performance as result of the more difficult access of the reagents to the catalytic sites.

The one pot intramolecular hydroamination followed by enantioselective reduction to produce chiral THQs was successfully obtained with the AuNPs-TiO$_2$ catalyst. This catalyst, combined to the Hantzsch ester and chiral phosphoric acid auxiliary ((R)-3,3'-Bis(9-phenanthryl)-1,1'-binaphthalene-2,2'-diyl hydrogen phosphate) allowed, under mild conditions, the synthesis of chiral substituted THQs starting from 2-(2-propynyl)anilines, with excellent yields and regioselectivity in the ring closing reaction and very high enantioselectivity in the consecutive reduction to THQs. In particular, the synthesis of (S)-2-(4-methoxyphenyl)-1,2,3,4-tetrahydroquinoline with 95% yield and 99% ee, was achieved in only 30 min in toluene at 40°C. The heterogeneous Au(0) catalyst shows lower electrophilicity compared to homogeneous Au(I) catalysts;[151] this results in lower regioselectivity in the ring closing reaction leading to both indoles and quinolines. A fundamental role is played by the electronic properties of the aromatic ring of PA that can

modify the regioselectivity of the nucleophilic attack of the nitrogen atom to the π-system of the alkyne moiety.

CHAPTER 6

....

EXPERIMENTAL SECTION

CHAPTER 6: EXPERIMENTAL SECTION

6.1: GENERAL PROCEDURE AND MATERIALS

Reagents and reaction conditions are specifically described in the following paragraphs.

Tetrachloroauric acid trihydrate (≥49.0 wt% of Au, Sigma-Aldrich), sodium triethylborohydride (1.0 M in THF; Sigma-Aldrich), phenylacetylene (PA; 98%; Sigma-Aldrich), aniline (AN; 98 %; TCI Chemicals), p-toluidine (99 %; Sigma-Aldrich), 4-chloroaniline (98 %, Sigma-Aldrich), 2,4,6-trimethylaniline (98 %, Sigma-Aldrich), 4-bromoaniline (97 %, Sigma-Aldrich), 1-bromo-4-ethynylbenzene (97 %, Sigma-Aldrich), 4-ethynylanisole (97 %, Sigma-Aldrich), p-anisidine (>99 %, Sigma-Aldrich), 4-ethynyltoluene (97 %, Sigma-Aldrich), 1-octine (95 %; TCI Chemicals), AuNPs-TiO$_2$ (1 *wt%*Au on titania support; Strem Chemicals), AuNPs-ZnO (1 *wt%*Au on zinc oxide; Strem Chemicals), AuNPs-Al$_2$O$_3$ (1 *wt%*Au on aluminium oxide; Strem Chemicals), AuNPs–CB (1 *wt%*Au on amorphous carbon black support; Strem Chemicals), Au(III) standard solution for analysis ICP-OES of AuNPs-sPSB (1.000±0.002 g/L of gold in water with 2 wt% of HCl; Carlo Erba Reagenti), Diethyl 1,4-dihydro-2,6-dimethyl-3,5-pyridinedicarboxylate (95%, Sigma-Aldrich), (*R*)-(−)-1,1'-Binaphthyl-2,2'-diyl hydrogenphosphate (>98%, Sigma-Aldrich), (R)-3,3'-Bis(9-phenanthryl)-1,1'-binaphthalene-2,2'-diyl hydrogen phosphate (>98%, Sigma-Aldrich), sodium chloride (Sigma Aldrich), methanol (HPLC grade for catalytic tests, Sigma Aldrich), H$_2$O (HPLC purity, Romil), chloroform

(HPLC grade, Romil), cesium carbonate (97.9%, Sigma–Aldrich), potassium hydroxide (90%, Sigma–Aldrich), sodium hydroxide (98%, Sigma–Aldrich), sodium carbonate anhydrous (99.5%, Sigma–Aldrich), potassium carbonate anhydrous (99.9%, Sigma–Aldrich), oxygen (5.0 grade; Linde) and deuterated solvents (Sigma-Aldrich) were used as received.

The solvents were dried prior the use using the following procedures. THF (Sigma-Aldrich, 99%) was pre-dried with potassium hydroxide, then refluxed for 48h over sodium and benzophenone in nitrogen atmosphere and distilled at atmospheric pressure. Toluene (Sigma-Aldrich, 99.5%), 2-MeTHF (Sigma-Aldrich, >99%), CH_2Cl_2 (Sigma-Aldrich, 99.8%), CH_3CN (Sigma-Aldrich, 99.8%) were pre-dried over $CaCl_2$; THF over KOH. MeOH (HPLC grade; Sigma–Aldrich) was dried by heating at reflux for 1 h over magnesium turnings. DMF (99.8%, Sigma–Aldrich) and DMA (99%, Sigma–Aldrich) were purified by stirring for 12 h over CaH_2. Molecular sieves (3Å, Sigma– Aldrich) were activated by treatment at 200°C in vacuum. The sPSB copolymer (88 mol% ; 93 wt% of styrene)[90], the AuNPs-sPSB catalysts (Au content of 2.0 wt%)[86,87], *N,N*-Aniline-d_2[189] and 2-(2-propynyl)anilines[151] were synthesized and characterized according to the reported procedures.

6.2: INSTRUMENTS AND CHARACTERIZATIONS

6.2.1: ICP-OES ANALYSIS

ICP-OES was performed on Perkin-Elmer Optima 7000 DV instrument. The sample was prepared as follow. 0.0500 g of the sample were digested in a Kjeldahl apparatus using 2.5 mL of H_2SO_4 (98 *wt%*) at 250°C for 30 min followed by treatment with H_2O_2 (4mL, 30 *wt%*) at room temperature. The solution was heated at 250°C producing a colorless solution. At room temperature, 1.5 mL of aqua regia were added and the solution was diluted to reach the final volume of 10 mL with a HCl solution (10 v%) and a sample of the resulting solution was analyzed. The calibration was obtained preparing seven solutions with variable concentration of Au(III) by dilution of a standard solution (1.000±0.002 g/L in water with 2 wt% of HCl) with water and an aqueous solution of HCl (10 v%).

6.2.2: WAXD ANALYSIS

WAXD patterns were obtained in reflection mode with an automatic Bruker D8 powder diffractometer and nickel-filtered CuKα radiation. The catalyst was dried at 25°C under vacuum for 12 h. The average size of AuNPs was obtained by considering the Scherrer equation ($D=K/\Gamma cos\theta$) where **D** is the weighted average diameter of Au(0) crystallites, **K** is a constant (=1.4476°) which depends from the crystallite shape and

wavelength of the X-Ray. **Γ** and **θ** are the full width at half maximum and Bragg angle of the (111) peak of Au(0).[103]

6.2.3: TEM ANALYSIS

Conventional TEM analysis was carried out with a Tecnai Spirit transmission electron microscope (FEI) working at acceleration voltage of 120 kV, equipped with a lanthanum hexaboride thermionic electron source and a twin objective lens. The images were acquired using a Gatan Orius CCD camera. HRTEM was carried out with a Titan transmission electron microscope (FEI) working at acceleration voltage of 300 kV, equipped with an ultra-bright field emission electron source (X-FEG), a super-twin objective lens. The images were acquired using a Gatan 2kx2k CCD camera. For both CTEM and HRTEM imaging, the specimens were prepared by dispersing and sonicating the AuNPs-sPSB catalyst in isopropanol, followed by deposition of a small droplet onto a grid for TEM imaging (carbon film supported by 300-meshes copper) supplied by TedPella (USA).

6.2.4: XPS ANALYSIS

XPS analysis were performed at normal angle emission in a Specs setup, using Al Kα monochromatic radiation (hv = 1486.7 eV) of an X-ray gun,

operating with 300 W (12 kV/25 mA) power. A flood gun with electron acceleration at 1eV and electron current of 100 mA was used in order to avoid charging effects. The energy of photo-ejected electrons was measured using a Phoibos 150 analyzer, operating with pass energy of 30eV. The spectra were fitted using Voigt profiles combined with their primitive functions, for inelastic background. The spectra were collected in the energy range corresponding to Au(0) 4f $_{7/2}$ Au(0) 4f $_{5/2}$ peaks.

6.2.5: ATOMIC ABSORPTION ANALYSIS

Atomic absorption spectroscopy analysis was performed on a PerkinElmer AAnalyst 100 spectrophotometer by using an Au hollow cathode lamp (PerkinElmer). The sample preparation was performed as reported for ICP-OES ANALYSIS.

6.2.6: NMR ANALYSIS

NMR spectroscopy was performed on Avance Bruker spectrometers (600, 400 and 300 MHz for ^{1}H). The chemical shifts were referenced to tetramethylsilane, as external reference, using the residual protium signal of the deuterated solvent. Deuterated solvents were purchased from Sigma-Aldrich and used as received. $CDCl_3$ and DMSO-d6 were generally used as solvent in the NMR experiments.

6.2.7: HPLC ANALYSIS

The enantiomeric excess was determined by chiral HPLC using CHIRACEL® OD-H column (250 x 4.6mm, 5μm), with UV detector set at 254nm and flow rate of 1.0 mL/min. UV measurements were made at 24-26°C using spectrophotometric grade solvents. The HPLC solvents, hexane and isopropanol, were purchased from Sigma-Aldrich and used as received.

6.3: COMPUTATIONAL METHODS APPLIED TO STUDY THE MECHANISM OF INTERMOLACULAR HYDROAMINATION REACTION OF PA AND AN

Theoretical DFT calculations were performed using the Gaussian 16 program package.[190] All geometry optimizations were executed using the pure Perdew, Burke and Ernzerhof functional[191] and the Ahlrichs basis set def2-SVP[192] was selected. To include also dispersive interactions, such as Au···H–C and Au···π,[193] the Grimme's dispersion correction[194] with Becke-Johnson damping was used in these optimizations. To characterize structures of minima ($N_{imag} = 0$) or transition states ($N_{imag} = 1$), analysis of corresponding frequencies was performed. All models were built starting from an Au_{20} cluster obtained from crystallographic coordinates. Initially, Au cluster was optimized using a D_{2h} point group symmetry. Then, all models were optimized on the surface keeping the optimization all Au atoms frozen. Gibbs free energies (ΔG_{298}, in kcal mol^{-1}) were invoked for

the discussion on the relative stabilities of the considered structures. Molecular Electrostatic Potential (MEP) surface of Au_{20} was also calculated at the same level of theory and plotted onto the van der Waal surface (0.001 a.u. isodensity value). The Bader's "Atoms in molecules" theory has been applied by means of the AIMall calculation package.[195]

6.4: GENERAL PROCEDURE FOR THE SYNTHESIS OF AuNPs-(δ)sPSB CATALYST

The AuNPs-(δ)sPSB catalyst (2wt% in Au) was synthesized according to the procedure reported in literature.[86] In a 1 L round-bottomed three-necked flask, equipped with a magnetic stirring bar, a sample of sPSB (5.00g),[90] is suspended in THF (700 mL) and the mixture is stirred for 24h at room temperature in nitrogen atmosphere and then heated at reflux to improve the polymer swelling. At the end of this process the solution is slowly cooled to room temperature and $HAuCl_4$ (220 mg, 0.56 mmol) is added to under fast stirring at room temperatures for 10 minutes to produce a yellow solution. Triethylborohydride in THF solution (20 mL, 1.0 M) is then added; the color of the mixture rapidly turned from yellow to purple and the slurry is precipitated in a plenty of methanol. The AuNPs-(δ)sPSB catalyst is recovered by filtration, washed with fresh methanol and dried in vacuo at room temperature.

6.4.1: SYNTHESIS OF AuNPs-(β)sPSB CATALYST

The thermal treatment at 170°C for 5h of AuNPs-(δ)sPSB resulting from the synthetic procedure yields the AuNPs-(β)sPSB catalyst.

6.4.2: SYNTHESIS OF AuNPs-(ε)sPSB CATALYST

The AuNPs-(ε)sPSB is obtained treating the AuNPs-(β)sPSB catalyst with a solvent mixture $CHCl_3/H_2O$ (v/v = 1/1) for 24h. The achieved catalyst is then filtered, washed with MeOH and dried in vacuo at room temperature.

6.5: SYNTHESIS OF N,N-ANILINE-d_2

The N,N-Aniline-d_2 was synthesized according to the literature.[189] In a 250 mL round bottom flask, equipped with a magnetic stirring bar, freshly distilled aniline (51.1 mg, 0.55 mmol) is stirred vigorously with deuterium oxide (100 mL) for 3 h. The mixture is loaded into a separatory funnel and the aqueous layer removed. The organic layer is washed with deuterium oxide (3x 25 mL) and dried over BaO. The N,N-Aniline-d_2 is distilled under vacuum and stored over 4Å molecular sieves (>98% deuteration yield).

6.6: SYNTHESIS OF SUBSTITUTED 2-(2-PROPYNYL)ANILINES

The 2-(2-propynyl)anilines were synthesized according to the literature[151] using the synthetic steps summarized schematically in **Figure 93**.
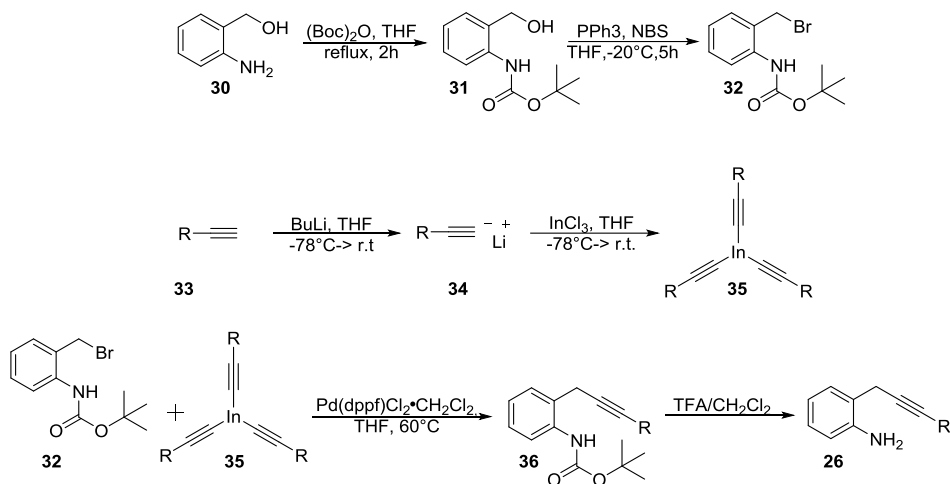
Figure 93: procedure for the synthesis of 2-(2-propynyl)anilines.

- **STEP 1: Synthesis of *tert*-butyl (2-(hydroxymethyl)phenyl carbamate 31.**[196]

  In a 50 mL round bottom flask equipped with a magnetic stirring bar, di-*tert*-butyl carbonate (1 equiv., 20mmol) is added under inert atmosphere to a solution of (2-aminophenyl) methanol **30** (1 equiv., 20 mmol) in THF (20 mL) at room temperature. The solution is heated at reflux for 3h under stirring and then

quenched by addition of water at room temperature. The reaction mixture is extracted with Et$_2$O and the organic phase is washed with water and brine, filtered and concentrated to dryness producing a yellow oil **31** (yield >99%) which was not further purified.

^{1}H-NMR chemical shifts of diagnostic signals are:

 (400 MHz CDCl3, 25 °C), δ (ppm) = 7.90 (1H, d, *J* = 8.1), 7.63 (1H, brs) 7.30 (1H, t, *J* = 7.8 Hz), 7.16 (1H, d, *J* = 7.5 Hz), 7.01 (1H, t, *J* = 7.5 Hz), 4.68 (2H, d, *J* = 5.8 Hz), 1.52 (9H, s).
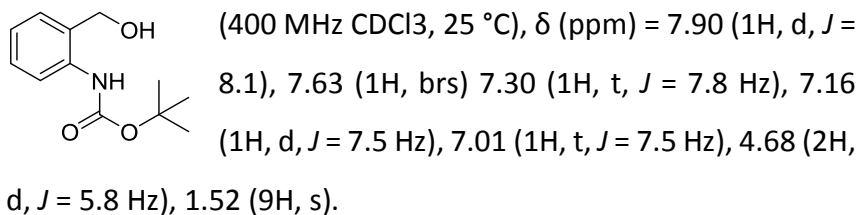
- **STEP 2: Synthesis of tert-butyl (2-(bromomethyl)phenyl) carbamate 32.**[197]

  In a 50 mL round bottom flask equipped with a magnetic stirring bar, at -20°C under inert atmosphere, triphenylphosphine (1.2 equiv., 8.0 mmol) and *N*-Bromosuccinimide (1.2 equiv., 8.0mmol) are slowly added to a solution of *tert*-butyl (2- (hydroxymethyl) phenyl)carbamate **31** (1 equiv., 6.7mmol) in THF (25mL. The mixture is left under stirring for 24h and then dried under vacuum. The mixture is purified by chromatography using silica gel support and 90:10 v/v Hexane:AcOEt as eluent. The product **32** was isolated as white solid (yield 68%).

¹H-NMR chemical shifts of diagnostic signals are:
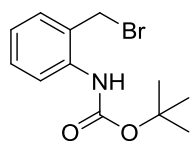
 (400 MHz CDCl3, 25 °C), δ (ppm) = 7.85 (1H, d, J = 8.2), 7.72 (1H, t, J = 7.8 Hz), 7.28 (1H, d, J = 7.6 Hz), 7.06 (1H, t, J = 7.6 Hz), 6.68 (1H, brs) 4.51 (2H, s), 1.54 (9H, s).

- **STEP 3: Synthesis of the organo-lithium reagents 34.**[198]

In a 100 mL round bottom flask equipped with a magnetic stirring bar, n-butyllithium solution in hexane (2.5 M, 1.2 equiv.) is dropwise added to a solution of the alkyne **33** (10.0 mmol, 1.0 equiv.) in THF (50 mL) at -78°C. The mixture is left under stirring at this temperature for 30 min, then slowly heated to room temperature and left for additional 30 min under stirring. The resulting solution is monitored by ¹H-NMR to observe the disappearance of the ¹H-signal of the alkyne proton.
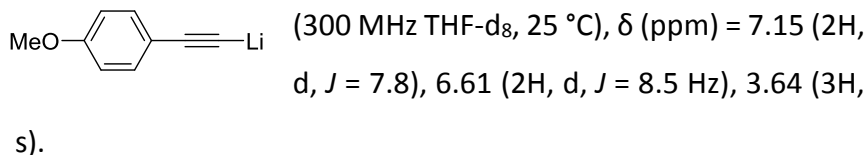
¹H-NMR chemical shifts of diagnostic signals are:

(phenylethynyl)lithium
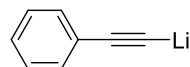
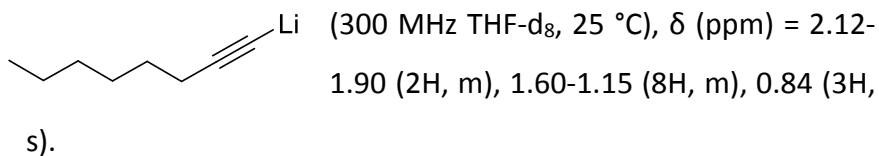 (400 MHz THF-d₈, 25 °C), δ (ppm) = 7.17 (2H, d, J = 7.0), 7.01 (2H, t, J = 7.6 Hz), 6.91 (1H, t, J = 7.3 Hz).

((4-methoxyphenyl)ethynyl)lithium

MeO—⟨benzene ring⟩—≡—Li   (300 MHz THF-d_8, 25 °C), δ (ppm) = 7.15 (2H, d, J = 7.8), 6.61 (2H, d, J = 8.5 Hz), 3.64 (3H, s).

Octynyllithium

⟨chain⟩—≡—Li   (300 MHz THF-d_8, 25 °C), δ (ppm) = 2.12-1.90 (2H, m), 1.60-1.15 (8H, m), 0.84 (3H, s).

- **STEP 4: Synthesis of triorgano-indium reagents 35.**[199]

  In a 250 mL round bottom flask equipped with a magnetic stirring bar, the solution of organo-lithium **34** previously obtained (10.0 mmol, 1.0 equiv.) is dropwise added at -78°C to a solution of dry InCl$_3$ (3.4 mmol, 0.34 equiv.) in THF (50 mL). The mixture is stirred at this temperature for 30 min and then slowly heated to room temperature and left for additional 30 min under stirring. The resulting solution is analyzed by ^{1}H-NMR spectroscopy.

^{1}H-NMR chemical shifts of diagnostic signals are:

Tris(phenylethynyl)indium
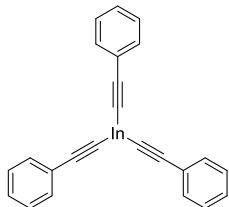
(300 MHz THF-d$_8$, 25 °C), δ (ppm) = 7.39-7.27 (6H, m), 7.18-7.00 (9H, m).

Tris((4-methoxyphenyl)ethynyl)indium
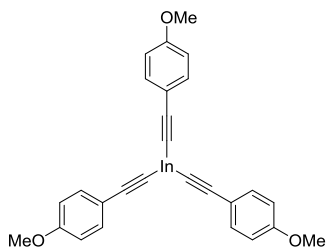
(300 MHz THF-d$_8$, 25 °C), δ (ppm) = 7.26-7.17 (6H, m), 6.71-6.66 (6H, m), 3.66 (9H, s).

Tri(octynyl)indium

(300 MHz THF-d$_8$, 25 °C), δ (ppm) = 2.12-1.90 (2H, m), 1.60-1.16 (8H, m), 0.83 (3H, s).
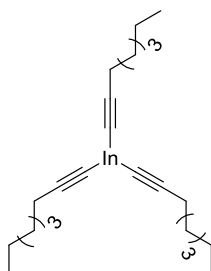
- **STEP 5: Coupling *tert*-butyl-(2-(bromomethyl)phenyl)carbamate 32 with triorgano-indium 35.[151]**

  In a 100 mL round bottom flask equipped with a magnetic stirring bar, a solution of triorgano-indium **35** (1 equiv., 3.0mmol) is added to a mixture of the *tert*-butyl-(2-(bromomethyl)phenylcarbamate **32** (2 equiv., 6.0 mmol) and Pd(dppf)Cl$_2$.CH$_2$Cl$_2$ (0.06 equiv., 0.18 mmol) in dry THF (10 mL). The resulting mixture is stirred at reflux for 3 h. The reaction is then quenched by the addition of MeOH (5 mL); THF was then partially distilled in vacuo. CH$_2$Cl$_2$ (25 mL) is added and the resulting solution is washed with aqueous HCl (5%), saturated aqueous NaHCO$_3$ and brine solution in the order. The organic phase is dried, filtered and concentrated in vacuo. The residue is purified through flash chromatography (petroleum ether: EtOAc 98:2) to produce **36**.

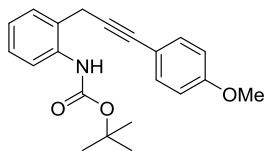 ^{1}H-NMR chemical shifts of diagnostic signals for the synthetized products **36** (δ in ppm, CDCl$_3$, 25 °C) are:

tert-butyl (2-(3-phenylprop-2-yn-1-yl)phenyl)carbamate
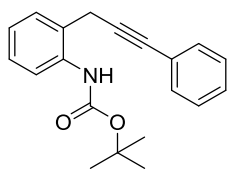
Yellow solid (yield 70%) (400 MHz), δ = 7.82 (1H, d, *J* = 7.3 Hz), 7.47- 7.40 (2H, m), 7.36-7.27 (5H, m), 7.08 (1H, t, *J* = 7.6 Hz), 6.99 (1H, brs), 3.75 (2H, s), 1.53 (9H, s).

tert-butyl (2-(3-(4-methoxyphenyl)prop-2-yn-1-yl)carbamate

Orange solid (yield 68%) (300 MHz), δ = 7.82 (1H, d, *J* = 7.8 Hz), 7.43- 7.26 (4H, m), 7.06 (1H, t, *J* = 7.5 Hz), 7.02 (1H, brs), 6.82 (2H, t, *J* = 8.9 Hz), 3.80 (3H, s), 3.72 (2H, s), 1.52 (9H, s)

tert-butyl (2-(non-2-yn-1-yl)phenyl)carbamate
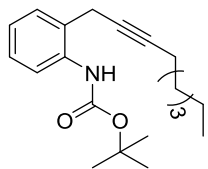
Yellow solid (yield 64%) (300 MHz), δ = 7.82 (1H, d, *J* = 7.5 Hz), 7.23 (1H, d, *J* = 8.6), 7.09-6.96 (3H, m), 3.47 (2H, s), 2.30-2.12 (2H, m), 1.74-1.15 (8H, m), 1.53 (9H, s), 0.88 (3H, s).

- **STEP 6: Synthesis of substituted 2-(2-propynyl)anilines 26.**[151]

In a round bottom flask **36** is dissolved in CH_2Cl_2 (final concentration solution 0.2 M) and trifluoroacetic acid (TFA) is added (ratio CH_2Cl_2 / TFA = 5/1). The reaction is stirred at room temperature for 1 h. After this time, the residue is diluted with CH_2Cl_2 and the mixture washed with saturated $NaHCO_3$ solution and brine. The organic phase is dried and concentrated in vacuo. The residue is purified through flash chromatography on silica gel, to obtain the product **26**.

^{1}H-NMR chemical shifts of diagnostic signals for the synthetized products **26**(δ in ppm, CDCl$_3$, 25 °C) are:

2-(3-phenylprop-2-ynyl)aniline
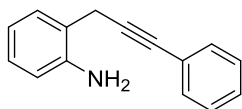
Yellow oil (yield 94%) (400 MHz), δ = 7.39-7.45 (2H, m), 7.27- 7.32 (4H, m), 7.12 (1H, t, *J* = 7.7 Hz), 6.79 (1H, t, *J* = 7.5 Hz), 6.72 (1H, d, *J* = 7.7 Hz), 3.91 (2H, brs), 3.67 (2H, s).

2-(3-(4-methoxyphenyl)prop-2-ynyl)aniline
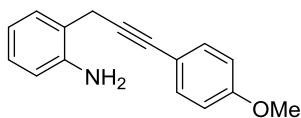
Brown solid (yield 87%) (300 MHz), δ = 8.01 (2H, d, *J* = 8.7 Hz), 7 .43 (1H, d, *J* = 7.5 Hz), 7.20- 7.30 (2H, m), 7.10- 7.18 (2H, m), 6.97 (2H, d, *J* = 8.9 Hz), 3.87 (3H, s), 2.87 (2H, brs), 2.86 (2H, s).

2-(non-2-ynyl)aniline
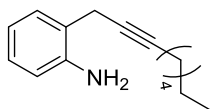
Brown oil (yield 70%) (300 MHz), δ = 7.17 (1H, d, *J*= 7.8 Hz), 7.08 (1H, t, *J*= 7.8 Hz), 6.74 (1H, t, *J*= 7.5 Hz), 6.69 (1H, d, *J*= 7.8 Hz), 3.89 (2H, brs), 3.41 (2H, s), 2.14-2.25 (2H, m), 1.15- 1.74 (6H, m), 0.88 (3H, t, *J*= 6.6 Hz).

6.7: GENERAL PROCEDURE ADOPTED FOR THE CATALYTIC TESTS

6.7.1: GENERAL PROCEDURE FOR INTERMOLECOLAR HYDROAMINATION REACTION CATALYZED BY AuNPs-sPSB

A 10 mL round bottom flask, equipped with a magnetic stirring bar, is charged with AuNPs-sPSB (100 mg; 2 *wt%* Au), alkyne (5.08 mmol), anilines (6.09 mmol), equilibrated at 100 °C and stirred for 7 h. After cooling to room temperature, DMSO-d_6 is added and the mixture is centrifuged (4000 rpm) to remove the catalyst, and then analyzed by ^{1}H-NMR spectroscopy. The resulting solution is analyzed by ^{1}H-NMR.

Below are reported ^{1}H-NMR chemical shift of diagnostic signals[200–202] for the reaction products (δ in ppm, DMSO-d_6, 25 °C):

(*E*)-*N*-1-diphenylethan-1-imine
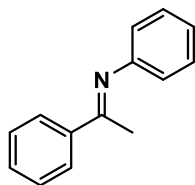
(400 MHz), δ = 7.99 (2H, d, *J* = 6.4 Hz), 7.52-7.45 (3H, m), 7.36 (2H, t, *J* = 7.7 Hz), 7.00 (1H, t, *J* = 7.7 Hz), 6.78 (2H, d, *J* = 7.3 Hz), 2.20 (3H, s);

(*E*)-1-(4-bromophenyl)-*N*-phenylethan-1-imine
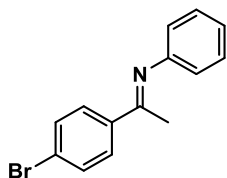
(400 MHz), δ = 7.92 (2H, d, *J* = 8.6 Hz), 7.68 (2H, d, *J* = 8.5 Hz), 7.36 (2H, t, *J* = 7.8 Hz), 7.08 (1H, t, *J* = 7.4 Hz), 6.79 (2H, d, *J* = 7.2 Hz), 2.18 (3H, s);

(*E*)-*N*-phenyl-1-(p-tolyl)ethan-1-imine
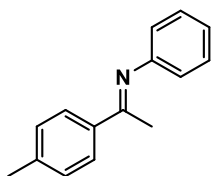
(400 MHz), δ = 7.88 (2H, d, *J* = 8.1 Hz), 7.35 (4H, t, *J* = 7.9 Hz), 7.07 (2H, t, *J* = 7.5 Hz), 6.77 (2H, d, *J* = 7.6 Hz), 2.31 (3H, s), 2.17 (3H, s);

(*E*)-1-(4-methoxyphenyl)-*N*-phenylethan-1-imine
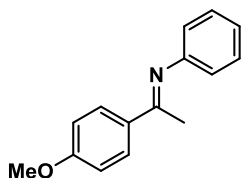
(400 MHz), δ = 7.95 (2H, d, *J* = 8.8 Hz), 7.34 (2H, t, *J* = 7.8 Hz), 7.04-6.98 (3H, m), 6.76 (2H, d, *J* = 7.3 Hz), 3.82 (3H, s), 2.15 (3H, s);

(*E*)-1-phenyl-*N*-(p-tolyl)ethan-1-imine
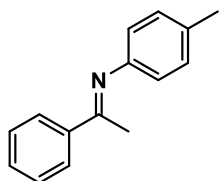
(300MHz), δ = 8.00-7.94 (2H, m), 7.52-7.44 (3H, m), 7.16 (2H, d, *J* = 7.9 Hz), 6.68 (2H, d, *J* = 8.1 Hz), 2.29 (3H, s), 2.19 (3H, s);

(*E*)-*N*-(4-methoxyphenyl)-1-phenylethan-1-imine
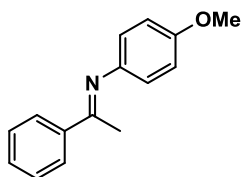
(300MHz), δ = 8.00-7.94 (2H, m), 7.51-7.43 (3H, m), 6.93 (2H, d, *J* = 8.7 Hz), 6.75 (2H, d, *J* = 8.7 Hz), 3.75 (3H, s), 2.21 (3H, s);

(*E*)-*N*-mesityl-1-phenylethan-1-imine
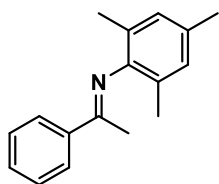
(400 MHz), δ =8.02 (2H, d, *J* = 6.6 Hz), 7.53-7.44 (3H, m), 6.86 (2H, s), 2.22 (3H, s), 2.02 (3H, s), 1.90 (6H, s);

(E)-N-(4-bromophenyl)-1-phenylethan-1-imine
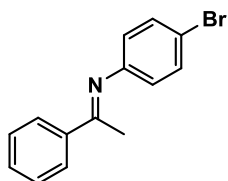
(400 MHz), δ = 7.98 (2H, m), 7.56-7.45 (4H, m), 7.11 (1H, d, J = 8.7 Hz), 6.77 (2H, d, J = 8.6 Hz), 2.20 (3H, s);

(E)-N-(4-chlorophenyl)-1-phenylethan-1-imine
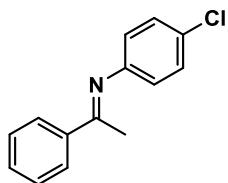
(400 MHz), δ = 7.98 (2H, m), 7.56-7.44 (4H, m), 7.00 (1H, d, J = 8.6 Hz), 6.82 (2H, d, J = 8.5 Hz), 2.21 (3H, s);

(Z)-N-phenyloctan-2-imine
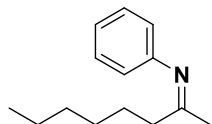
(600 MHz) δ = 1.71 (3H, s);

(E)-N-phenyloctan-2-imine
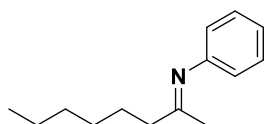
(600 MHz), δ = 2.06 (3H,s).

6.7.1.1: GENERAL PROCEDURE FOR THE RECYCLING TESTS

A 25 mL round bottom flask, equipped with a magnetic stirring bar, is charged with AuNPs-sPSB (500 mg; 2 *wt%* Au), phenylacetylene (25.4 mmol), aniline (30.2 mmol), equilibrated at 100 °C and left under stitting for 7 h at this temeprature. The reaction mixture is cooled to room temperature, DMSO-d_6 is added and then the mixture is centrifuged (4000 rpm). The catalyst is separated by filtration and the filtrate analyzed by ^{1}H-NMR spectroscopy. The catalyst is washed with MeOH, dried at room temperature and reused.

6.7.1.2: GENERAL PROCEDURE FOR KINETIC TESTS

The tests were performed under pseudo-first-order reaction conditions. A 10 mL round bottom flask, equipped with a magnetic stirring bar, is charged with AuNPs-sPSB (100 mg; 2 *wt%* Au), phenylacetylene and aniline or *N,N*-Aniline-d_2, equilibrated at 100 °C and left under stirring for the prescribed time. Depending on the case, the amount of PA and AN (or AN-d_2) are 10.51 mmol and 0.66 mmol, respectively, or vice versa. An aliquot of the reaction solution is sampled, DMSO-d_6 is added and the mixture is centrifugated (4000 rpm) to separate the catalyst. The supernatant solution is transferred into NMR tube and rapidly analyzed by ^{1}H-NMR spectroscopy.

6.7.2: SYNTHESIS OF 1,2,3,4-TETRAHYDROQUINOLINES BY INTRAMOLECULAR HYDROAMINATION OF 2-(2-PROPYNYL)ANILINES CATALYZED BY AuNPs-TiO₂

A 10 mL round bottom flask, equipped with a magnetic stirring bar, is charged with AuNPs-TiO$_2$ (100 mg; 1 *wt%* Au), Brønsted acid (*R*)-3,3'-Bis(9-phenanthryl)-1,1'-binaphthalene-2,2'-diyl hydrogen phosphate (0.005 mmol), Hantzsch ester Diethyl 1,4-dihydro-2,6-dimethyl-3,5-pyridinedicarboxylate (0.2 mmol), 2-(2-propynyl)anilines **26** (0.1 mmol) and 1mL of toluene. The reaction is equilibrated at 40 °C and left under stirring for the prescribed time. The reaction mixture is cooled to room temperature and the solvent distilled in vacuo. CDCl$_3$ is added and the mixture centrifuged at 4000 rpm to remove the catalyst. The supernatant solution is analyzed by ^{1}H-NMR spectroscopy.

Below are reported ^{1}H-NMR chemical shift of diagnostic signals[151,203,204] for the observed products (δ in ppm, CDCl$_3$, 25 °C), the HPLC characterization and optical rotation measurements.

(*S*)-2-phenyl-1,2,3,4-tetrahydroquinoline
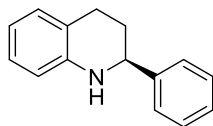
(300 MHz), δ = 7.23–7.48 (5H, m), 6.96–7.06 (2H, m), 6.65 (1H, td, *J* = 7.4, 1.0 Hz), 6.55 (1H, dd, *J* = 8.4, 1.2 Hz), 4.44 (1H, dd, *J* = 9.3, 3.3 Hz), 4.05 (1H, brs), 2.84–3.02 (1H, m), 2.74 (1H, dt, *J* = 16.4, 4.8 Hz), 2.07–2.19 (1H, m), 1.89–2.07 (1H, m). [α]$_D$ ^{21} = -20.6 (0.63M, EtOAc); Enantiomeric excess: 90%, determined by chiral HPLC (hexane/isopropanol = 95/5): t$_R$ = 10.95 min (major), t$_R$ = 14.33 min (minor). The absolute configuration was determined for comparison between the optical rotation measured and that reported in the literature.[151]

(*S*)-2-(4-methoxyphenyl)-1,2,3,4-tetrahydroquinoline
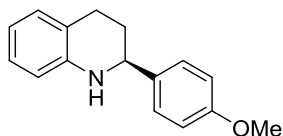
(300 MHz), δ = 7.27-7.35 (2H, m), 6.95-7.05 (2H, m), 6.84- 6.94 (2H, m), 6.65 (1H, td, *J* = 7.2, 0.9 Hz), 6.54 (1H, dd, *J* = 7.8, 0.9 Hz), 4.39 (1H, dd, *J* = 9.4, 3.3 Hz), 4.00 (1H, brs), 3.82 (3H, s), 2.84–3.02 (1H, m), 2.74 (1H, dt, *J* = 16.3, 4.6 Hz), 1.87–2.17 (2H, m). [α]$_D$ ^{28} = -33.4 (0.55M, EtOAc); Enantiomeric excess: 99%, determined by chiral HPLC (hexane/isopropanol = 95/5): t$_R$ = 11.76 min (major), t$_R$ = 16.96 min (minor). The absolute configuration was determined for comparison between the optical rotation measured and that reported in the literature.[151]

(R)-2-hexyl-1,2,3,4-tetrahydroquinoline
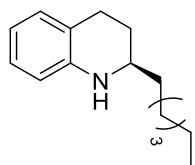
(300 MHz), δ = 6.88- 7.01 (2H, m), 6.60 (1H, t, J = 7.5 Hz), 6.47 (1H, d, J = 7.9 Hz), 3.72 (1H, brs), 3.14- 3.30 (1H, m), 2.64- 2.92 (2H, m), 1.88- 2.04 (1H, m), 1.00–1.70 (11H, m), 0.86 (3H, t, J = 6.8 Hz). $[\alpha]_D^{20}$ = 31.5 (0.46M, EtOAc); Enantiomeric excess: 70%, determined by chiral HPLC (hexane/isopropanol = 99/1; flow rate 0.5 ml/min): t_R = 13.30 min (major), t_R = 14.99 min (minor). The absolute configuration was determined for comparison between the optical rotation measured and that reported in the literature.[151]

2-Benzyl-1H-indole
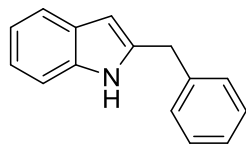
(300 MHz) δ = 7.78 (1H, brs), 7.50-7.58 (1H, m), 7.18- 7.39 (6H, m), 7.02-7.16 (2H, m), 6.33 (1H, s), 4.14 (2H, s).[203]

2-Phenylquinoline
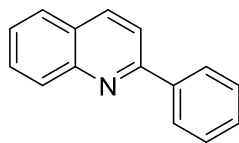
(300 MHz) δ = 8.23 (1H, d, J = 8.7 Hz), 8.13- 8.21 (3H, m), 7.89 (1H, d, J = 8.7 Hz), 7.84 (1H, dd, J = 8.1, 1.1 Hz), 7.74 (1H, dt, J =7.7, 1.3 Hz), 7.42-7.60 (m, 4H).[204]

6.7.2.1: GENERAL PROCEDURE FOR THE THQ·CDA COMPLEXES PREPARATION

In a NMR tube, the THQ **20** (8.0 mg, 1 equiv.) is dissolved in 0.6 mL of CDCl$_3$. The (*R*)-1,1-Binaphthyl-2,2-diyl hydrogenphosphate **23** (10.6 mg, molar ratio THQ:DCA = 1:0.8) is then added and the mixture (eventually sonicated) analyzed at ^{1}H-NMR.

6.7.3: OXIDATION OF HMF TO DFF CATALYZED BY AuNPs−sPSB

A 60 mL stainless-steel autoclave, equipped with a magnetic stirring bar, was charged with AuNPs−sPSB (50 mg; 2 *wt%* Au), Cs$_2$CO$_3$ (42 mg) and molecular sieves 4A (~50 mg). The reactor was sealed and the inner atmosphere was conditioned at atmospheric pressure and pressurized with O$_2$ (at 0.5 MPa) for five times. Then, the reactor was charged under fluing oxygen with an anhydrous solution of HMF (16 mg) in DMF (2.0 mL) and pressurized with O$_2$ at 1.5 MPa. The mixture was stirred at 80°C for 16 h. After this reaction time, the reactor was cooled in a water/ice bath and the oxygen pressure was slowly released. The mixture was analyzed by ^{1}H-NMR spectroscopy using DMSO-d$_6$ as solvent and anisole as external standard.

Below are reported ^{1}H-NMR and ^{13}C-NMR chemical shift of diagnostic signals[205–208] for the reaction products (δ in ppm, DMSO-d$_6$, 25 °C):

2,5-diformylfuran (DFF)
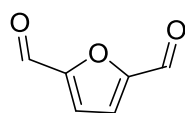
(400 MHz) δ = 9.83 ppm (2H, s), 7.57 (2H, s). ^{13}C-NMR: 121.5 (2C), 163.7 (2C), 180.2 (2C).

5-formyl-2-furancarboxylic acid (FFCA)
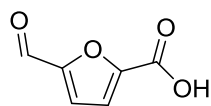
(400 MHz) δ = 9.55 (1H, s), 7.39 (1H, d, J = 3.3 Hz), 6.56 (1H, d, J = 3.3 Hz, 1H).

6.7.4: OXIDATIVE ESTERIFICATION OF HMF CATALYZED BY AuNPs–sPSB

A 60 mL stainless-steel autoclave, equipped with a magnetic stirring bar, was charged with AuNPs–sPSB (50 mg; 2 *wt%* Au), Cs$_2$CO$_3$ (42 mg) and molecular sieves 4A (~50 mg). The reactor was sealed and the inner atmosphere was conditioned at atmospheric pressure and pressurized with O$_2$ (at 0.5 MPa) for five times. Then, the reactor was charged under fluing oxygen with an anhydrous solution of HMF (16 mg) in MeOH (0.5 mL) and DMA (2.0 mL), and pressurized with O$_2$ at 1.5 MPa. The mixture was stirred at 110°C for 16 h. After this reaction time, the reactor was cooled in a water/ice bath and the oxygen pressure was slowly released. The mixture was analyzed by ^{1}H-NMR spectroscopy using DMSO-d$_6$ as solvent and anisole as external standard.

Below are reported ^{1}H-NMR and ^{13}C-NMR chemical shift of diagnostic signals[205–208] for the reaction products (δ in ppm, DMSO-d_6, 25 °C):

5-hydroxymethyl methylfuroate (HMMF)

(400 MHz) δ = 7.19 (1H, d, J = 3.2 Hz), 6.47 (1H, d, J = 3.2 Hz), 4.47 (2H, s), 3.78 (3H, s). ^{13}C-NMR: 52.2 (1C), 56.2 (1C), 109.1 (1C), 119.2 (1C), 143.3 (1C), 157.7 (1C), 158.1 (1C).

furan-2,5-dimethylcarboxylate (FDMC)
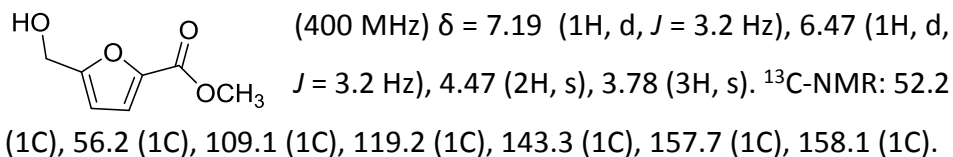
(400 MHz) δ = 7.32 (2H, s), 3.88 (6H, s). ^{13}C-NMR: 52.1 (2C), 118.7 (2C), 146.6 (2C), 158.2 (2C).
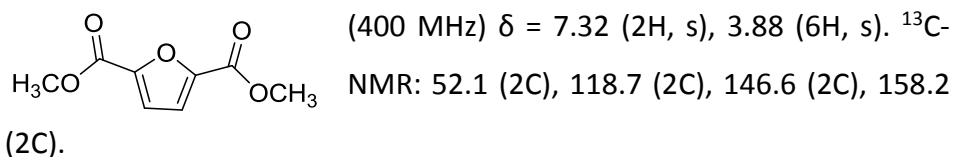
6.7.5: OXIDATION OF HMF TO FDCA CATALYZED BY AuNPs−sPSB

A 60 mL stainless-steel autoclave, equipped with a magnetic stirring bar, was charged with AuNPs−sPSB (50 mg; 2 *wt%* Au), Cs_2CO_3 (42 mg). The reactor was sealed and the inner atmosphere was conditioned at atmospheric pressure and pressurized with O_2 (at 0.5 MPa) for five times. Then, the reactor was charged under fluing oxygen with an anhydrous solution of HMF (16 mg) in H_2O (0.5 mL), MeOH (0.5 mL) and DMA (2.0

mL), and pressurized with O_2 at 1.5 MPa. The mixture was stirred at 110°C for 24 h. After this reaction time, the reactor was cooled in a water/ice bath and the oxygen pressure was slowly released. The mixture was analyzed by ^{1}H-NMR spectroscopy using DMSO-d$_6$ as solvent and anisole as external standard.

Below are reported ^{1}H-NMR and ^{13}C-NMR chemical shift of diagnostic signals[205–208] for the reaction products (δ in ppm, DMSO-d$_6$, 25 °C):

5-(methoxycarbonyl) furan-2-carboxylic acid (MFCA)
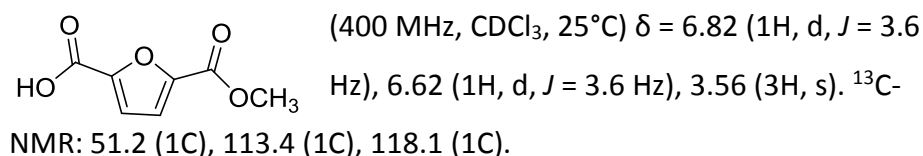
(400 MHz, CDCl$_3$, 25°C) δ = 6.82 (1H, d, J = 3.6 Hz), 6.62 (1H, d, J = 3.6 Hz), 3.56 (3H, s). ^{13}C-NMR: 51.2 (1C), 113.4 (1C), 118.1 (1C).

2,5-furandicarboxylic acid (FDCA)

(400 MHz, CDCl$_3$, 25°C) δ = 6.56 ppm (2H, s). ^{13}C-NMR: 113.5 (2C).

5-hydroxymethyl-2-furancarboxylic acid (HMFCA)

(400 MHz, D$_2$O+CD$_3$CN, 25°C) δ = 6.82 (1H, d, J = 3.4 Hz); 6.35 (1H, d, J = 3.4 Hz), 4.47 (2H, s). ^{13}C-NMR (D$_2$O, 25°C): 55.9 (1C), 109.2 (1C), 114.6 (1C).
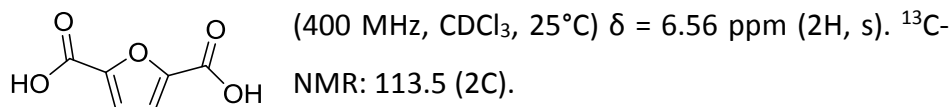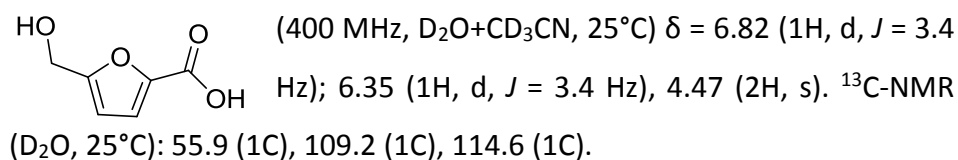
6.8: ¹H-NMR SPECTRA FOR THE (*E*)-*N*-1-DIPHENYLETHAN-1-IMINE EQUILIBRATION WITH AN-*d*₂
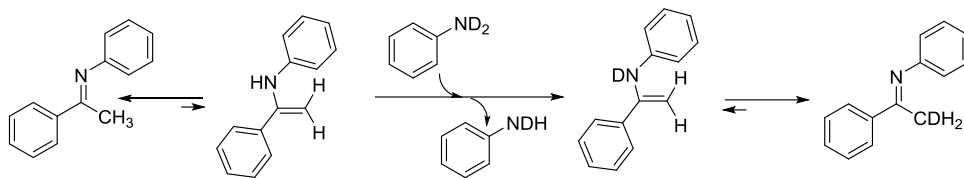
Figure 94: ¹H-NMR spectra of (E)-N,1-diphenylethan-1-imine: a) pure, b) in equilibration with AN-*d*₂ at room temperature, c) in equilibration with AN-*d*₂ at 80°C for 3h.

b)

8.017
8.014
8.000
7.995
7.488
7.382
7.184
7.119
6.843
6.822
6.789
6.716

2.258

2.258

2.25 ppm

8.0 7.5 7.0 6.5 6.0 5.5 5.0 4.5 4.0 3.5 3.0 2.5 2.0 1.5 1.0 0.5 ppm

c)

8.021
8.018
8.004
7.490
7.385
7.187
7.120
6.846
6.825
6.790
6.718
6.697

3.630

2.260
2.248
2.242

2.260
2.248
2.242

2.26 2.24 ppm

8.0 7.5 7.0 6.5 6.0 5.5 5.0 4.5 4.0 3.5 3.0 2.5 2.0 1.5 1.0 0.5 ppm
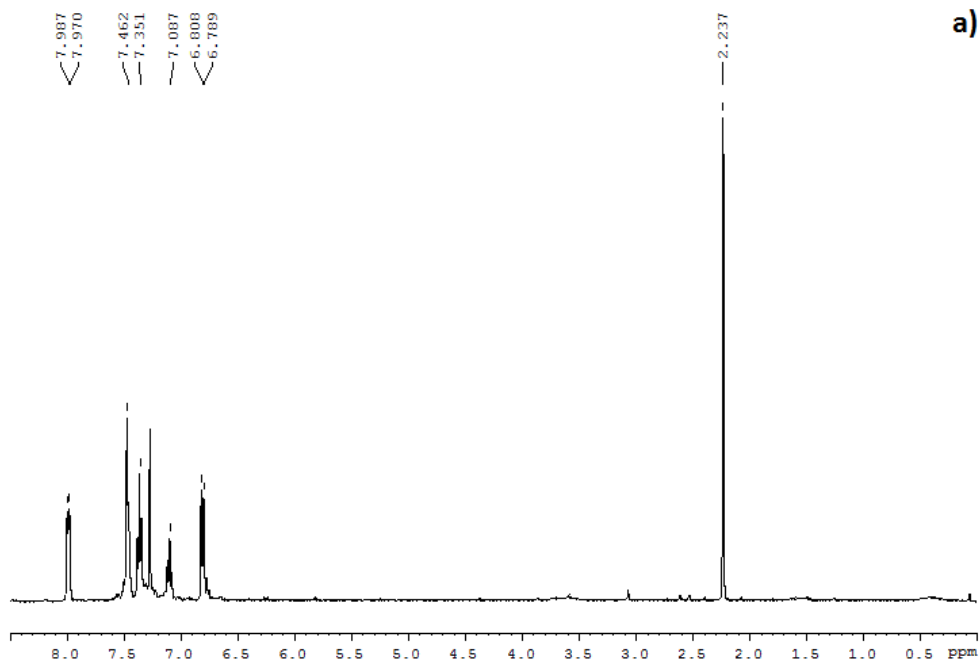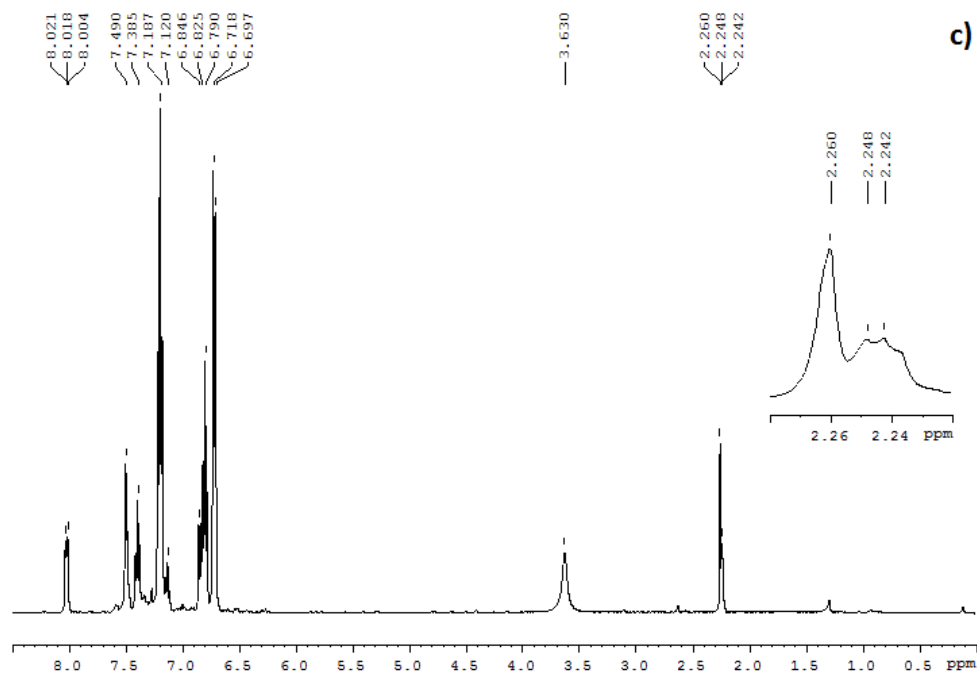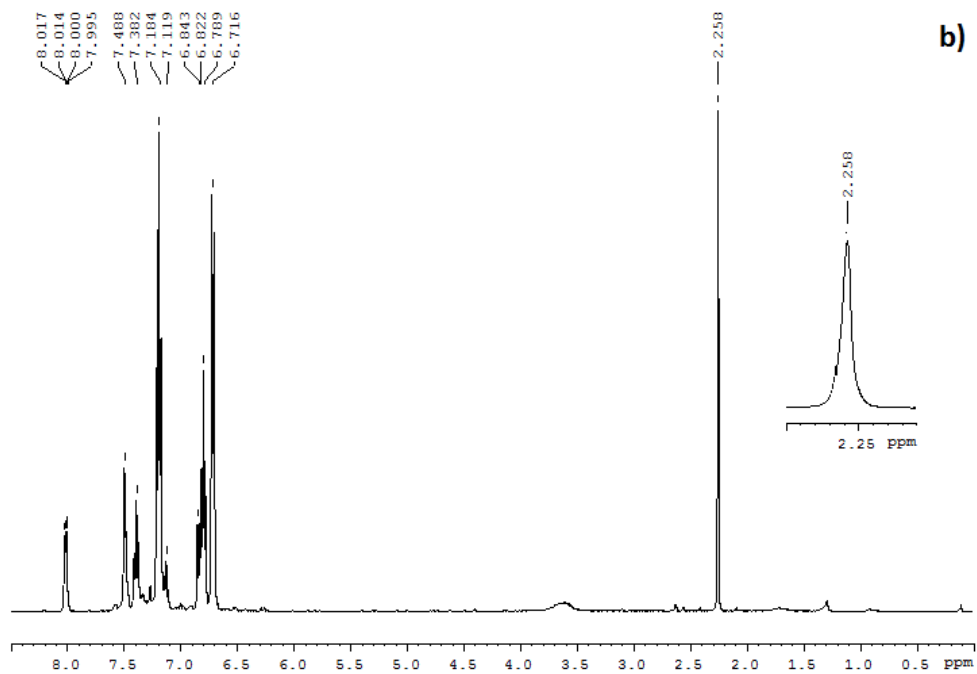
6.9: ¹H-NMR SPECTRA FOR THE DIASTEREOMERIC COMPLEXES THQ·CDA FORMATION.

Figure 95: ¹H-NMR spectra of racemic THQ 20: a) pure; b) in equilibration with (R)-1,1-Binaphthyl-2,2-diyl hydrogenphosphate 23 at room temperature.

a)

b)

224
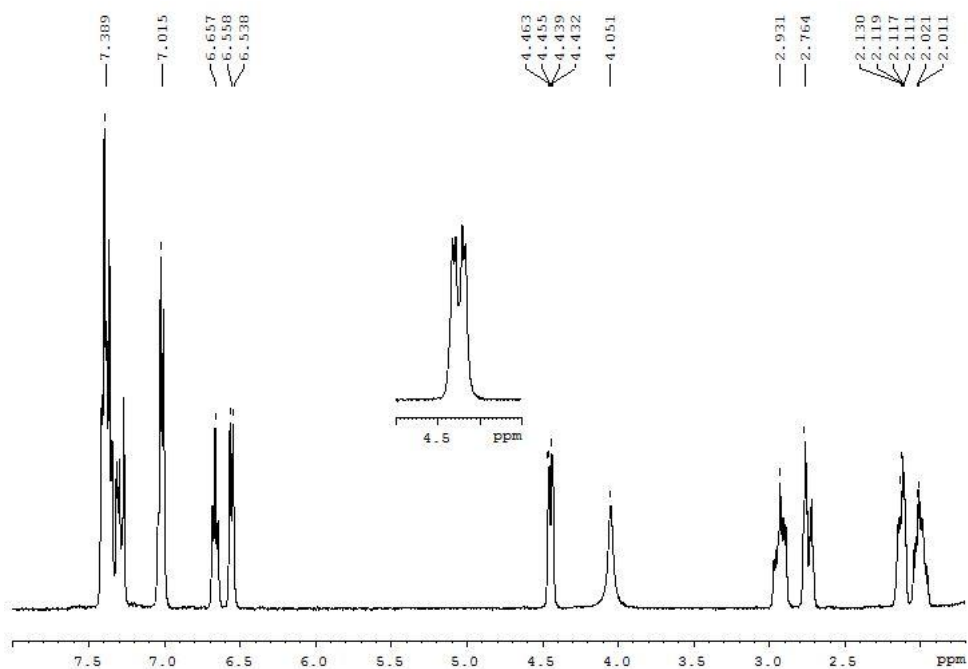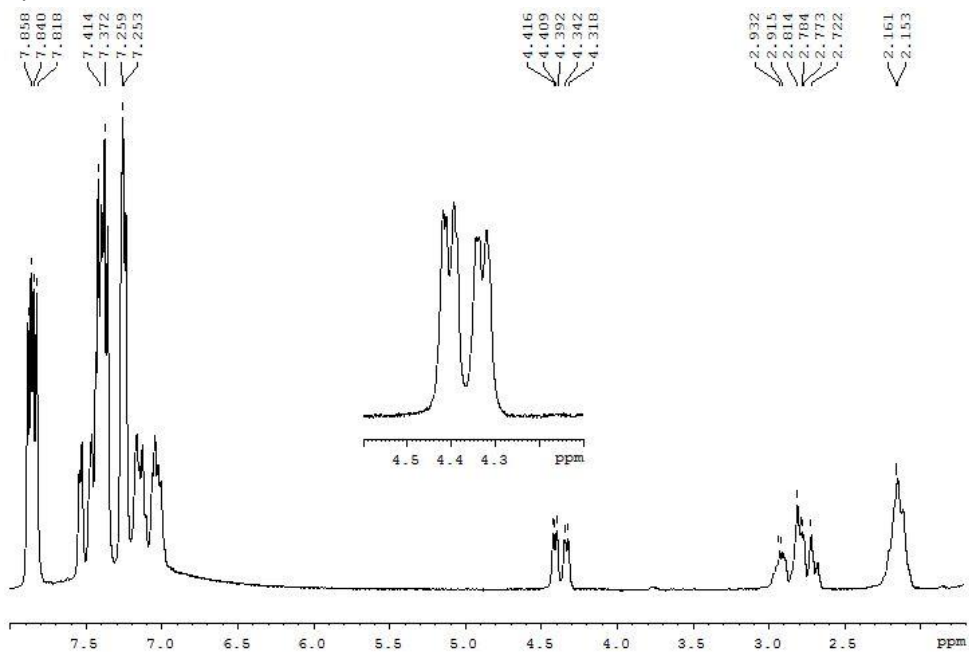
BIBLIOGRAPHY

(1)   Adekoya, J. A.; Ogunniran, K. O.; Siyanbola, T. O.; Dare, E. O.; Revaprasadu, N. *Noble and Precious Metals - Properties, Nanoscale Effects and Applications*; Seehra, M. S., Bristow, A. D., Eds.; InTech, 2018.

(2)   Daniel, M.-C.; Astruc, D. *Chem. Rev.* **2004**, *104*, 293–346.

(3)   Mody, V.; Siwale, R.; Singh, A.; Mody, H. *J. Pharm. Bioallied Sci.* **2010**, *2* (4), 282.

(4)   Amendola, V.; Pilot, R.; Frasconi, M.; Maragò, O. M.; Iatì, M. A. *J. Phys. Condens. Matter* **2017**, *29* (20), 203002.

(5)   Unser, S.; Bruzas, I.; He, J.; Sagle, L. *Sensors* **2015**, *15* (7), 15684–15716.

(6)   Agranovich, V. M.; Gartstein, Yu. N.; Litinskaya, M. Hybrid *Chem. Rev.* **2011**, *111* (9), 5179–5214.

(7)   Leonhardt, U. *Nat. Photonics* **2007**, *1* (4), 207–208.

(8)   X. The Bakerian Lecture *Philos. Trans. R. Soc. Lond.* **1857**, *147*, 145–181.

(9)   Toshima, N.; Yonezawa, T. *New J. Chem.* **1998**, *22* (11), 1179–1201.

(10)   Alshammari, A.; Kalevaru, V. N. *Catalytic Application of Nano-Gold Catalysts*; Mishra, N. K., Ed.; InTech, 2016.

(11)   Lopez, N. *J. Catal.* **2004**, *223* (1), 232–235.

(12)   Elechiguerra, J. L.; Reyes-Gasga, J.; Yacaman, M. J. *J. Mater. Chem.* **2006**, *16* (40), 3906.

(13)   Henry, C. R. *Prog. Surf. Sci.* **2005**, *80* (3–4), 92–116.

(14)   Stratakis, M.; Garcia, H. *Chem. Rev.* **2012**, *112* (8), 4469–4506.

(15)   Chen, M.; Goodman, D. W. *Chem. Soc. Rev.* **2008**, *37* (9), 1860.

(16)   Fierro-Gonzalez, J. C.; Gates, B. C. *Chem. Soc. Rev.* **2008**, *37* (9), 2127.

(17)   Sanchez, A.; Abbet, S.; Heiz, U.; Schneider, W.-D.; Häkkinen, H.; Barnett, R. N.; Landman, U. *J. Phys. Chem. A* **1999**, *103* (48), 9573–9578.

(18) Farnesi Camellone, M.; Kowalski, P. M.; Marx, D. *Phys. Rev. B* **2011**, *84* (3), 035413.

(19) Alshammari *Catalysts* **2019**, *9* (5), 402.

(20) Cuenya, B. R. *Thin Solid Films* **2010**, *518* (12), 3127–3150.

(21) Rodriguez, J. A.; Wang, X.; Liu, P.; Wen, W.; Hanson, J. C.; Hrbek, J.; Pérez, M.; Evans, J. *Top. Catal.* **2007**, *44* (1–2), 73–81.

(22) Rodriguez, J. A.; Liu, P.; Hrbek, J.; Evans, J.; Pérez, M. *Angew. Chem. Int. Ed.* **2007**, *46* (8), 1329–1332.

(23) Haruta, M. *Catal. Today* **1997**, *36* (1), 153–166.

(24) Corma, A.; Garcia, H. *Chem. Soc. Rev.* **2008**, *37* (9), 2096.

(25) Abad, A.; Corma, A.; García, H. *Chem. - Eur. J.* **2008**, *14* (1), 212–222.

(26) Dzhardimalieva, G. I.; Uflyand, I. E. *J. Polym. Res.* **2018**, *25* (12), 255.

(27) Ida, S.; Harada, H.; Sakai, K.; Atsumi, K.; Tani, Y.; Tanimoto, S.; Hirokawa, Y. *Chem. Lett.* **2017**, *46* (5), 760–763.

(28) Miyamura, H.; Yasukawa, T.; Kobayashi, S. *Green Chem.* **2010**, *12* (5), 776.

(29) Bond, G. C.; Sermon, P. A.; Webb, G.; Buchanan, D. A.; Wells, P. B. *J. Chem. Soc. Chem. Commun.* **1973**, 13, 444b.

(30) Hutchings, G. *J. Catal.* **1985**, *96* (1), 292–295.

(31) Haruta, M.; Kobayashi, T.; Sano, H.; Yamada, N. *Chem. Lett.* **1987**, *16* (2), 405–408.

(32) Takei, T.; Akita, T.; Nakamura, I.; Fujitani, T.; Okumura, M.; Okazaki, K.; Huang, J.; Ishida, T.; Haruta, M. *Advances in Catalysis* **2012**; 55, 1–126.

(33) Corti, C. W.; Holliday, R. J.; Thompson, D. T. *Top. Catal.* **2007**, *44* (1–2), 331–343.

(34) Corti, C. W.; Holliday, R. J. *Gold Bull.* **2004**, *37* (1–2), 20–26.

(35) Anastas, P. T.; Warner, J. C. *Green Chemistry: Theory and Practice*; Oxford University Press: Oxford [England]; New York, 1998.

(36) Elahi, N.; Kamali, M.; Baghersad, M. H. *Talanta* **2018**, *184*, 537–556.

(37) Hashmi, A. S. K. *Chem. Rev.* **2007**, *107* (7), 3180–3211.

(38)   Hayashi, T.; Tanaka, K.; Haruta, M. *J. Catal.* **1998**, *178* (2), 566–575.

(39)   Min, B. K.; Friend, C. M. *Chem. Rev.* **2007**, *107* (6), 2709–2724.

(40)   Landon, P.; Collier, P. J.; Papworth, A. J.; Kiely, C. J.; Hutchings, G. J. *Chem. Commun.* **2002**, 18, 2058–2059.

(41)   Teranishi, M.; Naya, S.; Tada, H. *J. Am. Chem. Soc.* **2010**, *132* (23), 7850–7851.

(42)   Choudhary, V. R.; Jana, P.; Bhargava, S. K. *Catal. Commun.* **2007**, *8* (5), 811–816.

(43)   Villa, A.; Wang, D.; Su, D. S.; Prati, L. *Catal. Sci. Technol.* **2015**, *5* (1), 55–68.

(44)   Ouyang, L.; Da, G.-J.; Ni, J.; Xu, J.; Han, Y.-F. *Recent Pat. Catal.* **2013**, *2* (1), 2–46.

(45)   Ferrando, R.; Jellinek, J.; Johnston, R. L. *Chem. Rev.* **2008**, *108* (3), 845–910.

(46)   Wang, A.; Liu, X. Y.; Mou, C.-Y.; Zhang, T. *J. Catal.* **2013**, *308*, 258–271.

(47)   Haruta, M. *Faraday Discuss.* **2011**, *152*, 11.

(48)   Wang, A.-Q.; Chang, C.-M.; Mou, C.-Y. *J. Phys. Chem. B* **2005**, *109* (40), 18860–18867.

(49)   Serna, P.; Concepción, P.; Corma, A. *J. Catal.* **2009**, *265* (1), 19–25.

(50)   Wang, Y.; Xia, Y. *Nano Lett.* **2004**, *4* (10), 2047–2050.

(51)   Herizchi, R.; Abbasi, E.; Milani, M.; Akbarzadeh, A. *Artif. Cells Nanomedicine Biotechnol.* **2016**, *44* (2), 596–602.

(52)   Freitas de Freitas, L.; Varca, G.; dos Santos Batista, J.; Benévolo Lugão, A. *Nanomaterials* **2018**, *8* (11), 939.

(53)   Turkevich, J.; Stevenson, P. C.; Hillier, J. *Discuss. Faraday Soc.* **1951**, *11*, 55.

(54)   Frens, G. *Nat. Phys. Sci.* **1973**, *241* (105), 20–22.

(55)   Wuithschick, M.; Birnbaum, A.; Witte, S.; Sztucki, M.; Vainio, U.; Pinna, N.; Rademann, K.; Emmerling, F.; Kraehnert, R.; Polte, J. Turkevich *ACS Nano* **2015**, *9* (7), 7052–7071.

(56)   Brust, M.; Walker, M.; Bethell, D.; Schiffrin, D. J.; Whyman, R. *J Chem Soc Chem Commun* **1994**, *0* (7), 801–802.

(57)   Wilcoxon, J. P.; Abrams, B. L. *Chem. Soc. Rev.* **2006**, *35* (11), 1162.

(58)   Dong, S.-A.; Zhou, S.-P. *Mater. Sci. Eng. B* **2007**, *140* (3), 153–159.

(59)   Sanabria-Cala J.A.; Conde Rodriguez G.R.; Gauthier G.H.; Ladeira L.O.; Laverde Catano D.A.; Pena Ballesteros D.Y.; Merchan Arenas D.R. *Chem. Eng. Trans.* **2018**, *64*, 403–408.

(60)   Misra, N.; Biswal, J.; Gupta, A.; Sainis, J. K.; Sabharwal, S. *Radiat. Phys. Chem.* **2012**, *81* (2), 195–200.

(61)   Abedini, A.; Daud, A. R.; Abdul Hamid, M. A.; Kamil Othman, N.; Saion, E. *Nanoscale Res. Lett.* **2013**, *8* (1), 474.

(62)   Raveendran, P.; Fu, J.; Wallen, S. L. *Green Chem* **2006**, *8* (1), 34–38.

(63)   Gutiérrez-Wing, C.; Esparza, R.; Vargas-Hernández, C.; Fernández García, M. E.; José-Yacamán, M. *Nanoscale* **2012**, *4* (7), 2281.

(64)   Lee, K. X.; Shameli, K.; Yew, Y. P.; Teow, S.-Y.; Jahangirian, H.; Rafiee-Moghaddam, R.; Webster, T. *Int. J. Nanomedicine* **2020**, *15*, 275–300.

(65)   Noruzi, M. *Bioprocess Biosyst. Eng.* **2015**, *38* (1), 1–14.

(66)   Carabineiro, S. A. C. *Front. Chem.* **2019**, *7*, 702.

(67)   Tsubota, S.; Haruta, M.; Kobayashi, T.; Ueda, A.; Nakahara, Y. *Studies in Surface Science and Catalysis*; Elsevier, 1991; 63, 695–704.

(68)   Cárdenas-Lizana, F.; Pedro, Z. M. D.; Gómez-Quero, S.; Kiwi-Minsker, L.; Keane, M. A. *J. Mol. Catal. Chem.* **2015**, *408*, 138–146.

(69)   Behravesh, E.; Kumar, N.; Balme, Q.; Roine, J.; Salonen, J.; Schukarev, A.; Mikkola, J.-P.; Peurla, M.; Aho, A.; Eränen, K.; Murzin, D. Yu.; Salmi, T. *J. Catal.* **2017**, *353*, 223–238.

(70)   Ofir, Y.; Samanta, B.; Rotello, V. M. *Chem. Soc. Rev.* **2008**, *37* (9), 1814.

(71)   Shan, J.; Tenhu, H. *Chem. Commun.* **2007**, 44, 4580.

(72)   Alexandridis, P. *Chem. Eng. Technol.* **2011**, *34* (1), 15–28.

(73)   Sarkar, S.; Guibal, E.; Quignard, F.; SenGupta, A. K. *J. Nanoparticle Res.* **2012**, *14* (2), 715.

(74) dos Santos, D. S.; Goulet, P. J. G.; Pieczonka, N. P. W.; Oliveira, O. N.; Aroca, R. F. *Langmuir* **2004**, *20* (23), 10273–10277.

(75) Chatterjee, U.; Jewrajka, S. K. *J. Colloid Interface Sci.* **2007**, *313* (2), 717–723.

(76) Laudenslager, M. J.; Schiffman, J. D.; Schauer, C. L. *Biomacromolecules* **2008**, *9* (10), 2682–2685.

(77) Huang, H.; Yang, X. *Biomacromolecules* **2004**, *5* (6), 2340–2346.

(78) Shi, F.; Deng, Y. *J. Catal.* **2002**, *211* (2), 548–551.

(79) Tsunoyama, H.; Sakurai, H.; Negishi, Y.; Tsukuda, T. *J. Am. Chem. Soc.* **2005**, *127* (26), 9374–9375.

(80) Burato, C.; Centomo, P.; Pace, G.; Favaro, M.; Prati, L.; Corain, B. *J. Mol. Catal. Chem.* **2005**, *238* (1–2), 26–34.

(81) Corain, B.; Burato, C.; Centomo, P.; Lora, S.; Meyer-Zaika, W.; Schmid, G. *J. Mol. Catal. Chem.* **2005**, *225* (2), 189–195.

(82) Ishida, T.; Haruta, M.; Makiyama, R. Patent JP 2007-082287. **2007**.

(83) Miyamura, H.; Matsubara, R.; Miyazaki, Y.; Kobayashi, S. *Angew. Chem. Int. Ed.* **2007**, *46* (22), 4151–4154.

(84) Rouquerol, J.; Avnir, D.; Fairbridge, C. W.; Everett, D. H.; Haynes, J. M.; Pernicone, N.; Ramsay, J. D. F.; Sing, K. S. W.; Unger, K. K. *Pure Appl. Chem.* **1994**, *66* (8), 1739–1758.

(85) White, R. J.; Luque, R.; Budarin, V. L.; Clark, J. H.; Macquarrie, D. J. *Chem Soc Rev* **2009**, *38* (2), 481–494.

(86) Buonerba, A.; Cuomo, C.; Ortega Sánchez, S.; Canton, P.; Grassi, A. *Chem. Eur. J.* **2012**, *18* (2), 709–715.

(87) Noschese, A.; Buonerba, A.; Canton, P.; Milione, S.; Capacchione, C.; Grassi, A. *J. Catal.* **2016**, *340*, 30–40.

(88) Buonerba, A.; Noschese, A.; Grassi, A. *Chem. - Eur. J.* **2014**, *20* (18), 5478–5486.

(89) Buonerba, A.; Impemba, S.; Dentoni Litta, A.; Capacchione, C.; Milione, S.; Grassi, A. *ChemSusChem* **2018**, *11* (18), 3139–3149.

(90) Caprio, M.; Serra, M. C.; Bowen, D. E.; Grassi, A. *Macromolecules* **2002**, *35* (25), 9315–9322.

(91) Milano, G.; Guerra, G. *Prog. Mater. Sci.* **2009**, *54* (1), 68–88.

(92) Gowd, E. B.; Tashiro, K.; Ramesh, C. *Prog. Polym. Sci.* **2009**, *34* (3), 280–315.

(93) Rizzo, P.; Daniel, C.; De Girolamo Del Mauro, A.; Guerra, G. *Chem. Mater.* **2007**, *19* (16), 3864–3866.

(94) De Rosa, C.; Guerra, G.; Petraccone, V.; Pirozzi, B. *Macromolecules* **1997**, *30* (14), 4147–4152.

(95) Albunia, A. R.; Rizzo, P.; Guerra, G. *Chem. Mater.* **2009**, *21* (14), 3370–3375.

(96) Shnoudeh, A. J.; Hamad, I.; Abdo, R. W.; Qadumii, L.; Jaber, A. Y.; Surchi, H. S.; Alkelany, S. Z. *Biomaterials and Bionanotechnology*; Elsevier, 2019; 527–612.

(97) Mourdikoudis, S.; Pallares, R. M.; Thanh, N. T. K. *Nanoscale* **2018**, *10* (27), 12871–12934.

(98) Tsunoyama, H.; Sakurai, H.; Tsukuda, T. *Chem. Phys. Lett.* **2006**, *429* (4–6), 528–532.

(99) Graphics and Images Taken from Cytodiagnostics Inc. Https://Www.Cytodiagnostics.Com/Pages/Introduction-to-Gold Nanoparticle-Characterization.

(100) Liu, X.; Atwater, M.; Wang, J.; Huo, Q. *Colloids Surf. B Biointerfaces* **2007**, *58* (1), 3–7.

(101) Haiss, W.; Thanh, N. T. K.; Aveyard, J.; Fernig, D. G. *Anal. Chem.* **2007**, *79* (11), 4215–4221.

(102) Singh, A. K.; Srivastava, O. N. *Nanoscale Res. Lett.* **2015**, *10* (1), 353.

(103) *Metal Nanoclusters in Catalysis and Materials Science: The Issue of Size Control*, 1st ed.; Corain, B., Schmid, G., Toshima, N., Eds.; Elsevier: Amsterdam ; Boston, 2008.

(104) Shard, A. G. A *J. Phys. Chem.* **2012**, *116* (31), 16806–16813.

(105) Casaletto, M. P.; Longo, A.; Martorana, A.; Prestianni, A.; Venezia, A. M. *Surf. Interface Anal.* **2006**, *38* (4), 215–218.

(106) *Handbook of X-Ray Photoelectron Spectroscopy: A Reference Book of Standard Spectra for Identification and Interpretation of XPS Data*; Moulder, J. F., Stickle, W. F., Sobol, P. E., Bomben, K. D., Chastain, J., King Jr., R. C., Physical Electronics, Incorporation, Eds.; Physical Electronics: Eden Prairie, Minn., 1995.

(107) Inkson, B. J. *Materials Characterization Using Nondestructive Evaluation (NDE) Methods*; Elsevier, 2016; 17–43.

(108) Goon, I. Y.; Lai, L. M. H.; Lim, M.; Munroe, P.; Gooding, J. J.; Amal, R. *Chem. Mater.* **2009**, *21* (4), 673–681.

(109) Müller, T. E.; Hultzsch, K. C.; Yus, M.; Foubelo, F.; Tada, M. *Chem. Rev.* **2008**, *108* (9), 3795–3892.

(110) Severin, R.; Doye, S. *Chem. Soc. Rev.* **2007**, *36* (9), 1407.

(111) Pohlki, F.; Doye, S. *Chem. Soc. Rev.* **2003**, *32* (2), 104–114.

(112) Straub, T.; Haskel, A.; Neyroud, T. G.; Kapon, M.; Botoshansky, M.; Eisen, M. S. *Organometallics* **2001**, *20* (24), 5017–5035.

(113) Müller, T. E.; Hultzsch, K. C.; Yus, M.; Foubelo, F.; Tada, M. *Chem. Rev.* **2008**, *108* (9), 3795–3892.

(114) Patel, M.; Saunthwal, R. K.; Verma, A. K. *Acc. Chem. Res.* **2017**, *50* (2), 240–254.

(115) Bytschkov, I.; Doye, S. *Eur J Org Chem* **2001**, 8.

(116) Vasudevan, A.; Verzal, M. K. *Synlett* **2004**, 4, 631–634.

(117) Zhao, J.; Zheng, Z.; Bottle, S.; Chou, A.; Sarina, S.; Zhu, H. *Chem. Commun.* **2013**, *49* (26), 2676.

(118) Liang, S.; Hammond, L.; Xu, B.; Hammond, G. B. *Adv. Synth. Catal.* **2016**, *358* (20), 3313–3318.

(119) Parise, C.; Ballarin, B.; Barreca, D.; Cassani, M. C.; Dambruoso, P.; Nanni, D.; Ragazzini, I.; Boanini, E. *Applied Surface Science* **2019**, *492*, 45–54.

(120) Corma, A.; Concepcion, P.; Dominguez, I.; Forne, V.; Sabater, M. Gold *J. Catal.* **2007**, *251* (1), 39–47.

(121) Huang, L.; Arndt, M.; Gooßen, K.; Heydt, H.; Gooßen, L. J. *Chem. Rev.* **2015**, *115* (7), 2596–2697.

(122) Mizushima, E.; Hayashi, T.; Tanaka, M. *Org. Lett.* **2003**, *5* (18), 3349–3352.

(123) Zhdanko, A.; Maier, M. E. *Angew. Chem. Int. Ed.* **2014**, *53* (30), 7760–7764.

(124) Sengupta, M.; Bag, A.; Das, S.; Shukla, A.; Konathala, L. N. S.; Naidu, C. A.; Bordoloi, A. *ChemCatChem* **2016**, *8* (19), 3121–3130.

(125) Zhao, J.; Zheng, Z.; Bottle, S.; Chen, C.; Huang, Y.; Sarina, S.; Chou, A.; Zhu, H. *RSC Adv.* **2016**, *6* (38), 31717–31725.

(126) Lee, L.-C.; Zhao, Y. *ACS Catal.* **2014**, *4* (2), 688–691.

(127) Liu, D.; Nie, Q.; Zhang, R.; Cai, M. *Adv. Synth. Catal.* **2018**, *360* (20), 3940–3948.

(128) Seral-Ascaso, A.; Luquin, A.; Lázaro, M. J.; de la Fuente, G. F.; Laguna, M.; Muñoz, E. *Appl. Catal. Gen.* **2013**, *456*, 88–95.

(129) Kitahara, H.; Sakurai, H. *J. Organomet. Chem.* **2011**, *696* (1), 442–449.

(130) Hydroamination of Terminal Alkynes on Gold Nanoclusters. *Synfacts* **2019**, *15* (04), 0405.

(131) Solovyeva, V. A.; Vu, K. B.; Merican, Z.; Sougrat, R.; Rodionov, V. O. *ACS Comb. Sci.* **2014**, *16* (10), 513–517.

(132) DeRuiter, J. Principles Of Drug Action 1, Resonance and Induction. **2005**.

(133) Miyazaki, Y.; Kobayashi, S. *J. Comb. Chem.* **2008**, *10* (3), 355–357.

(134) Sá, J.; Goguet, A.; Taylor, S. F. R.; Tiruvalam, R.; Kiely, C. J.; Nachtegaal, M.; Hutchings, G. J.; Hardacre, C. *Angew. Chem. Int. Ed.* **2011**, *50* (38), 8912–8916.

(135) Kesavan, L.; Tiruvalam, R.; Rahim, M. H. A.; bin Saiman, M. I.; Enache, D. I.; Jenkins, R. L.; Dimitratos, N.; Lopez-Sanchez, J. A.; Taylor, S. H.; Knight, D. W.; Kiely, C. J.; Hutchings, G. J. *Science* **2011**, *331* (6014), 195–199.

(136) Davis, S. E.; Ide, M. S.; Davis, R. J. *Green Chem* **2013**, *15* (1), 17–45.

(137) Couce-Rios, A.; Kovács, G.; Ujaque, G.; Lledós, A. *ACS Catal.* **2015**, *5* (2), 815–829.

(138) O'Hagan, D. *Nat. Prod. Rep.* **2000**, *17* (5), 435–446.

(139) Nakamura, I.; Yamamoto, Y. *Chem. Rev.* **2004**, *104* (5), 2127–2198.

(140) Alonso, F.; Beletskaya, I. P.; Yus, M. *Chem. Rev.* **2004**, *104* (6), 3079–3160.

(141) Kaur, R.; Bariwal, J.; Voskressensky, L. G.; Van der Eycken, E. V. *Chem. Heterocycl. Compd.* **2018**, *54* (3), 241–248.

(142) Perea-Buceta, J. E.; Wirtanen, T.; Laukkanen, O.-V.; Mäkelä, M. K.; Nieger, M.; Melchionna, M.; Huittinen, N.; Lopez-Sanchez, J. A.; Helaja, J. *Angew. Chem.* **2013**, *125* (45), 12051–12055.

(143) Yamane, Y.; Liu, X.; Hamasaki, A.; Ishida, T.; Haruta, M.; Yokoyama, T.; Tokunaga, M. *Org. Lett.* **2009**, *11* (22), 5162–5165.

(144) Zhang, X.; Corma, A. *Angew. Chem. Int. Ed.* **2008**, *47* (23), 4358–4361.

(145) Savva, I.; Kalogirou, A.; Achilleos, M.; Vasile, E.; Koutentis, P.; Krasia-Christoforou, T. *Molecules* **2016**, *21* (9), 1218.

(146) Muthukrishnan, I.; Sridharan, V.; Menéndez, J. C. *Chem. Rev.* **2019**, *119* (8), 5057–5191.

(147) Sridharan, V.; Suryavanshi, P. A.; Menéndez, J. C. *Chem. Rev.* **2011**, *111* (11), 7157–7259.

(148) Su, D.-S.; Lim, J. J.; Tinney, E.; Wan, B.-L.; Young, M. B.; Anderson, K. D.; Rudd, D.; Munshi, V.; Bahnck, C.; Felock, P. J.; Lu, M.; Lai, M.-T.; Touch, S.; Moyer, G.; DiStefano, D. J.; Flynn, J. A.; Liang, Y.; Sanchez, R.; Prasad, S.; Yan, Y.; Perlow-Poehnelt, R.; Torrent, M.; Miller, M.; Vacca, J. P.; Williams, T. M.; Anthony, N. J. *Bioorg. Med. Chem. Lett.* **2009**, *19* (17), 5119–5123.

(149) Wang, H.; Li, Y.; Sun, F.; Feng, Y.; Jin, K.; Wang, X. *J. Org. Chem.* **2008**, *73* (21), 8639–8642.

(150) Patil, N. T.; Wu, H.; Yamamoto, Y. A *J. Org. Chem.* **2007**, *72* (17), 6577–6579.

(151) Han, Z.-Y.; Xiao, H.; Chen, X.-H.; Gong, L.-Z. *J. Am. Chem. Soc.* **2009**, *131* (26), 9182–9183.

(152) Zhao, G.; Yin, Y. *HETEROCYCLES* **2006**, *68* (1), 23.

(153) Rueping, M.; Antonchick, A. P.; Theissmann, T. *Angew. Chem. Int. Ed.* **2006**, *45* (22), 3683–3686.

(154) Rueping, M.; Theissmann, T. *Chem. Sci.* **2010**, *1* (4), 473.

(155) Shapiro, M. J.; Archinal, A. E.; Jarema, M. A. *J. Org. Chem.* **1989**, *54* (24), 5826–5828.

(156) Fielding, L. *Tetrahedron* **2000**, *56* (34), 6151–6170.

(157) Crisci, A. J.; Tucker, M. H.; Dumesic, J. A.; Scott, S. L. *Top. Catal.* **2010**, *53* (15–18), 1185–1192.

(158) Takagaki, A.; Nishimura, S.; Ebitani, K. *Catal. Surv. Asia* **2012**, *16* (3), 164–182.

(159) Zakrzewska, M. E.; Bogel-Łukasik, E.; Bogel-Łukasik, R. *Chem. Rev.* **2011**, *111* (2), 397–417.

(160) Dull, G. *Chem. Zeit.* **1895**, *19*, 216–217.

(161) Melo, F. C. de; Souza, R. F. de; Coutinho, P. L. A.; Souza, M. O. *J. Braz. Chem. Soc.* **2014**.

(162) Menegazzo, F.; Ghedini, E.; Signoretto, M. *Molecules* **2018**, *23* (9), 2201.

(163) Toftgaard Pedersen, A.; Ringborg, R.; Grotkjær, T.; Pedersen, S.; Woodley, J. M. *Chem. Eng. J.* **2015**, *273*, 455–464.

(164) Rosatella, A. A.; Simeonov, S. P.; Frade, R. F. M.; Afonso, C. A. M. *Green Chem.* **2011**, *13* (4), 754.

(165) Lewkowski, J. *Arkivoc* **2001**, *2*, 17–54.

(166) Alonso, D. M.; Bond, J. Q.; Dumesic, J. A. *Green Chem.* **2010**, *12* (9), 1493.

(167) Moreau, C.; Belgacem, M. N.; Gandini, A. *Top. Catal.* **2004**, *27* (1–4), 11–30.

(168) Román-Leshkov, Y.; Barrett, C. J.; Liu, Z. Y.; Dumesic, J. A. *Nature* **2007**, *447* (7147), 982–985.

(169) van Putten, R.-J.; van der Waal, J. C.; de Jong, E.; Rasrendra, C. B.; Heeres, H. J.; de Vries, J. G. *Chem. Rev.* **2013**, *113* (3), 1499–1597.

(170) Pal, P.; Saravanamurugan, S. *ChemSusChem* **2019**, *12* (1), 145–163.

(171) Xia, H.; Xu, S.; Hu, H.; An, J.; Li, C. *RSC Adv.* **2018**, *8* (54), 30875–30886.

(172) Zhao, D.; Su, T.; Wang, Y.; Varma, R. S.; Len, C. *Mol. Catal.* **2020**, *495*, 111-133.

(173) Gorbanev, Y. Y.; Klitgaard, S. K.; Woodley, J. M.; Christensen, C. H.; Riisager, A. *ChemSusChem* **2009**, *2* (7), 672–675.

(174) Casanova, O.; Iborra, S.; Corma, A. *ChemSusChem* **2009**, *2* (12), 1138–1144.

(175) Davis, S. E.; Houk, L. R.; Tamargo, E. C.; Datye, A. K.; Davis, R. J. *Catal. Today* **2011**, *160* (1), 55–60.

(176) Ma, B.; Wang, Y.; Guo, X.; Tong, X.; Liu, C.; Wang, Y.; Guo, X. *Appl. Catal. Gen.* **2018**, *552*, 70–76.

(177) Zhu, Y.; Lu, M. *RSC Adv.* **2015**, *5* (104), 85579–85585.

(178) Albonetti, S.; Lolli, A.; Morandi, V.; Migliori, A.; Lucarelli, C.; Cavani, F. *Appl. Catal. B Environ.* **2015**, *163*, 520–530.

(179) Villa, A.; Schiavoni, M.; Campisi, S.; Veith, G. M.; Prati, L. *ChemSusChem* **2013**, *6* (4), 609–612.

(180) Pasini, T.; Piccinini, M.; Blosi, M.; Bonelli, R.; Albonetti, S.; Dimitratos, N.; Lopez-Sanchez, J. A.; Sankar, M.; He, Q.; Kiely, C. J.; Hutchings, G. J.; Cavani, F. *Green Chem.* **2011**, *13* (8), 2091.

(181) Ferraz, C. P.; Zieliński, M.; Pietrowski, M.; Heyte, S.; Dumeignil, F.; Rossi, L. M.; Wojcieszak, R. *ACS Sustain. Chem. Eng.* **2018**, *6* (12), 16332–16340.

(182) Gupta, N. K.; Nishimura, S.; Takagaki, A.; Ebitani, K. *Green Chem.* **2011**, *13* (4), 824.

(183) Taarning, E.; Nielsen, I. S.; Egeblad, K.; Madsen, R.; Christensen, C. H. *ChemSusChem* **2008**, *1* (1–2), 75–78.

(184) Casanova, O.; Iborra, S.; Corma, A. *J. Catal.* **2009**, *265* (1), 109–116.

(185) Menegazzo, F.; Fantinel, T.; Signoretto, M.; Pinna, F.; Manzoli, M. *J. Catal.* **2014**, *319*, 61–70.

(186) Menegazzo, F.; Signoretto, M.; Marchese, D.; Pinna, F.; Manzoli, M. *J. Catal.* **2015**, *326*, 1–8.

(187) Wojcieszak, R.; Ferraz, C.; Sha, J.; Houda, S.; Rossi, L.; Paul, S. *Catalysts* **2017**, *7* (11), 352.

(188) Wan, X.; Zhou, C.; Chen, J.; Deng, W.; Zhang, Q.; Yang, Y.; Wang, Y. *ACS Catal.* **2014**, *4* (7), 2175–2185.

(189) Batrice, R. J.; Eisen, M. S. *Chem. Sci.* **2016**, *7* (2), 939–944.

(190) Frisch, M. J.; Trucks, G. W.; Schlegel, H. B.; Scuseria, G. E.; Robb, M. A.; Cheeseman, J. R.; Scalmani, G.; Barone, V.; Petersson, G. A.; Nakatsuji, H.; Li, X.; Caricato, M.;

Marenich, A. V.; Bloino, J.; Janesko, B. G.; Gomperts, R.; Mennucci, B.; Hratchian, H. P.; Ortiz, J. V.; Izmaylov, A. F.; Sonnenberg, J. L.; Williams; Ding, F.; Lipparini, F.; Egidi, F.; Goings, J.; Peng, B.; Petrone, A.; Henderson, T.; Ranasinghe, D.; Zakrzewski, V. G.; Gao, J.; Rega, N.; Zheng, G.; Liang, W.; Hada, M.; Ehara, M.; Toyota, K.; Fukuda, R.; Hasegawa, J.; Ishida, M.; Nakajima, T.; Honda, Y.; Kitao, O.; Nakai, H.; Vreven, T.; Throssell, K.; Montgomery Jr., J. A.; Peralta, J. E.; Ogliaro, F.; Bearpark, M. J.; Heyd, J. J.; Brothers, E. N.; Kudin, K. N.; Staroverov, V. N.; Keith, T. A.; Kobayashi, R.; Normand, J.; Raghavachari, K.; Rendell, A. P.; Burant, J. C.; Iyengar, S. S.; Tomasi, J.; Cossi, M.; Millam, J. M.; Klene, M.; Adamo, C.; Cammi, R.; Ochterski, J. W.; Martin, R. L.; Morokuma, K.; Farkas, O.; Foresman, J. B.; Fox, D. J. *Gaussian 16 Rev. C.01*; Wallingford, CT, 2016.

(191) Perdew, J. P.; Burke, K.; Ernzerhof, M. *Phys. Rev. Lett.* **1996**, *77* (18), 3865–3868.

(192) Weigend, F.; Ahlrichs, R. *Phys. Chem. Chem. Phys.* **2005**, *7* (18), 3297.

(193) Cordón, J.; Jiménez-Osés, G.; López-de-Luzuriaga, J. M.; Monge, M. *Nat. Commun.* **2017**, *8* (1), 1657.

(194) Grimme, S.; Ehrlich, S.; Goerigk, L. *J. Comput. Chem.* **2011**, *32* (7), 1456–1465.

(195) AIMAll (Version 19.10.12), Todd A. Keith, TK Gristmill Software, Overland Park KS, USA, 2019 (Aim.Tkgristmill.Com).

(196) Mukai, C.; Kobayashi, M.; Kubota, S.; Takahashi, Y.; Kitagaki, S. *J. Org. Chem.* **2004**, *69* (6), 2128–2136.

(197) Han, H. S.; Oh, E. H.; Jung, Y.-S.; Han, S. B. *Org. Lett.* **2018**, *20* (7), 1698–1702.

(198) Eisch, J. J.; Liu, W.; Zhu, L.; Rheingold, A. L. *Eur. J. Org. Chem.* **2015**, *2015* (33), 7384–7394.

(199) Bouissane, L.; Sestelo, J. P.; Sarandeses, L. A. *Org. Lett.* **2009**, *11* (6), 1285–1288.

(200) Han, Z.; Wang, Z.; Zhang, X.; Ding, K. *Angew. Chem. Int. Ed.* **2009**, *48* (29), 5345–5349.

(201) Tillack, A.; Khedkar, V.; Jiao, H.; Beller, M. *Eur. J. Org. Chem.* **2005**, *2005* (23), 5001–5012.

(202) Li, W.; Hou, G.; Chang, M.; Zhang, X. *Adv. Synth. Catal.* **2009**, *351* (18), 3123–3127.

(203) Zhou, L.; Shi, Y.; Xiao, Q.; Liu, Y.; Ye, F.; Zhang, Y.; Wang, J. *Org. Lett.* **2011**, *13* (5), 968–971.

(204) Meléndez Gómez, C. M.; Kouznetsov, V. V.; Sortino, M. A.; Álvarez, S. L.; Zacchino, S. A. *Bioorg. Med. Chem.* **2008**, *16* (17), 7908–7920.

(205) Verdeguer, P.; Merat, N.; Gaset, A. *J. Mol. Catal.* **1993**, *85* (3), 327–344.

(206) Liu, T.; Liu, L.; Jiang, X.; Huang, X.; Chen, J. *Can. J. Plant Pathol.* **2009**, *31* (1), 22–27.

(207) Hanson, S. K.; Wu, R.; Silks, L. A. *Org. Lett.* **2011**, *13* (8), 1908–1911.

(208) Boyer, A.; Lautens, M. *Angew. Chem. Int. Ed.* **2011**, *50* (32), 7346–7349.